Project No. 13-5292

Correlating Thermal and Mechanical Coupling Based Multiphysics Behavior of Nuclear Materials through In-Situ Measurements

Fuel Cycle Research and Development

Vikas Tomar
Purdue University

In collaboration with:
Pennsylvania State University

Frank Goldner, Federal POC
Cetin Unal, Technical POC

NEUP Nuclear Energy University Programs
U.S. Department of Energy

Final Report

DOE Award Number:	DE-NE0000696
Recipient:	Purdue University
Project title:	(Project 13-5292) Correlating Thermal and Mechanical Coupling Based Multiphysics Behavior of Nuclear Materials through In-Situ Measurements
Principal investigator:	Vikas Tomar, Professor tomar@purdue.edu 765-494-3423
Project period:	1/1/14 – 12/31/16
Report submission date:	03/15/2016
Reporting period:	01/01/14 – 12/31/16

DISCLAIMER

TABLE OF CONTENTS

EXECUTIVE SUMMARY

The following are milestones, along with deliverable and criterion for completion:

Year 3 (1/16 to 12/16)

Correlation of microstructure change prediction of Zircaloy with established literautre studies as well as with Marmot based predictions, Establishment of user subroutine data that correlates thermo-mechanical multiphysics, 12/31/2016

Deliverable Title Multiphysical Property User subroutine

Criteria for verified user subroutine for use in Bison and Marmot to predict
Completion microstructure influenece on multiphysical properties

Task 8: Combine feedback from TEM thermomechanical property measurement experiments and simulations to provide uncertainty quantified dataset that links microstructure damage to irradiation with measured levels of confidence.

Year 3 Goal: This task has been completed..

Task 9: *In-situ* Nanomechanical and micromechanical SERS based measurements to understand the effect of temperature up to 1000 ºC on environment dependent coupled thermal and mechanical properties.

Year 3 Goal: This task has been completed..

Task 10: Establishment of microstructure-irradiation-stress-environment-temperature correlations using Bayesian uncertainty quantification procedures that affect separate effect multiphysics properties of Zircaloy. Development of empirical relations predicting such correlations.

Year 3 Goal: This task has been completed..

YEAR 2 (1/15 TO 12/15)

Establishment of Irradiation and Temperature effects on Zircaloy microstructures in Sandia I3 TEM,Measurement of Irradiation and Temperature influence on Zircaloy Thermal and Mechanical properties 12/31/2015

Deliverable Title	Zircaloy Temperature and Irradiation Dependent Thermal and Mechanical Coupling Properties
Criteria for Completion	Successful experimental protocols, dataset that verifies available literature, New Dataset that predicts how microstructure in Zircaloy correlates to Multiphysical properties

Task 5: *In-situ* TEM measurements of thermal conductivity as function of irradiation and mechanical stressing,

Year 2 Goal: This task has been completed.

In-situ TEM tests were performed on evaporated as deposited and Zr+ irradiated specimens (collaboration with Sandia National Laboratories) 100 nm thick, 10 micron wide and 100 micron long. The samples were exposed to Zr+ 800KeV at 4.5nA with doses of 3E10, 3E11 and 3E+12 (collaboration with Sandia National Laboratories). Figure S2.13 shows a typical stress-strain diagram for as deposited specimen. The lack of plastic deformation is due to the small grain size (~10 nm) that is unable to accommodate dislocations. Also the freestanding film has surfaces

through which the defects can escape, causing the dislocation starvation. Diffusive plasticity also doesn't take place at room temperature because Zr is a very high melting point material.

Collaborating with University of Dayton, we were able to sputter deposit Zircaloy thin films on the MEMS devices. Control of microstructure of the specimens was performed in-situ in TEM. Our previous finding was that up to 100 times grain size increase by thermo-electro-mechanical annealing was possible. In this period, we worked on the zircaloy thin films. For zircaloy, remarkable grain growth due to heating is about shown inside the TEM. Here the grain size increased about 10 times after heating to 150 ^{o}C. The extent of such grain growth is very obvious in the diffraction patterns. The grains also showed extensive dislocations inside. The results suggest that nanocrystalline zircaloy has higher grain boundary mobility, which gives rise to the high temperature sensitivity.

Thermal conductivity for Zr specimens as function of applied strain was measured. Thermal conductivity decreases as we increase the strain. This behavior can be ascribed to the nanocrystalline microstructure of these thin films. When the geometric dimension of specimen or the grain sizes go down to nanoscale, it becomes increasingly difficult for the grain interiors to accommodate the external deformations. Therefore, mechanical deformation mechanisms for grain sizes smaller than phonon mean free path (about 20 nm) are basically different from the bulk ones which is not only due to absence of dislocations but also very high volume fraction of the grain boundaries. In absence of dislocations in the grain interior, the grain boundaries primarily accommodate the applied strain. To accomplish this, the grain boundaries must slide, rotate or emit dislocations that also move along the grain boundaries as strain is applied. The scattering of electrons by grain boundaries will be enhanced by these grain motions. Therefore we hypothesize that the motion of grain boundaries resulted from strain localization is the primary mechanism behind thermal-strain coupling

Finally, we measured the thermal conductivity of the as function of irradiation. About 38% reduction of thermal conductivity is seen at $3.26x10^{14}$ ions/cm^2 radiation. We hypothesize that the effect of irradiation is most prominent at the grain boundaries, which are easier to knocked out by the ions. Pronounced disorder at the grain boundaries lead to the reduction in thermal transport

A major obstacle for the proposed research was integration of electron transparent zircaloy specimen (sectioned from the bulk) with the MEMS devices for in-situ TEM testing. The issue was the planarity of the specimen (irrespective of FIB sectioned or electropolished or ion milled). Since the MEMS devices are highly planar, any warpage in the specimen makes it challenging to fix both ends of the specimen on the two planar jaws of the MEMS. In this quarter, we have resolved this issue and have demonstrated it on gamma irradiated zircaloy specimens.

Task 6: *In-situ* Nanomechanical and micromechanical SERS based measurements of environment dependent thermal conductivity, diffusivity as a function of stress/strain
Year 2 Goal: This task has been completed.

One hour prior to corrosion testing, all samples were polished with SiC paper. Immediately before electrolyte submersion, the samples were degreased with a solvent and rinsed with distilled water.

These methods are in accordance with the ASTM G5. Prior to mechanical testing, samples were again degreased with a solvent and rinsed with distilled water. No further polishing are performed to ensure corrosion effects are accurately represented. So far, we have performed two corrosion tests. One is unirradiated zircaloy sample, the otherone is irradiated zircaloy sample. From compare their corrosion test data, we can find some clue about how does the radiation affect zircaloy corrosion resistence. In Fig. 3.17, we showed the corrosion rate of unirradiated sample in both palarization resistance model and Tafel model. In Fig.3.19, we compared the corrosion rate of unirradiated and irradiated samples in both palarization resistance model and Tafel model. It's obvious that zircaloy samples after irradiation will have a higher corrosion rate. Which consistents with common sense and our expection, radiation will reduce the material's corrosion resistance.

The micro-Raman method is a noncontact and nondestructive method for thermal conductivity measurements. In our case, we want to use micro-Raman method to measure thermal conductivity of the irradiated zircaloy specimen. However, there's a thin silicon film on our specimen, which means that the film thermal conductivity, film thickness, substrate thermal conductivity and interface thermal resistance all have effects on the heat transfer process. A computational model was developed for implementation into MOOSE for incorporating these effects. Computational model closely predicted the experimental thermal conductivity fields in Zircaloy sampleas as a function of stress and temperatures.

Experiments at microstructure level are time consuming. In order to incorporate the experimental results in a predictive manner as new phase field model was developed that incorporates microstructure dependency of the research results. This model is being interfaced with MARMOT.

Task 7: Identification of key microstructural parameters that link irradiation induced damage and environment dependent thermomechanical coupling based on quantified data
Year 2 Goal: This task has been completed.
TEM measurements specifically focused on thin film specimen subjected to irradiation. Samples, mainly with ion-irradiation were analyzed. Due to sample preparation limitations highlighted in task 5, specific type of GB's/grains and their correlation with irradiation damage was not possible to be obtained with using TEM. Instead a combined phase-fields modeling and nanomechanical SERS based approach was adopted. Specific microstructure related trends were found in the initial phase. These studies ae not getting extended as part of task 10 in year 3.

YEAR 1 (1/14 TO 12/14) [COMPLETED]

Zr processing and Zircaloy processing, Sample characterization as a function of irradiation, Initial TEM based measurements of coupled thermomechanical properties in Zr, Nanomechanical and Micromechanical High Temperature Measurements of Zr Samples 12/31/2014

Deliverable Title	Zr and Zircaloy with controlled microstructure, Establishment of experimental protocols
	Initial establishment of experimental and processing protocols
Criteria for	Electron microscopy based characterized microstructures; Database relating

Completion microstructure with multiphysical properties of Zr and Zircaloy Interface

Task 1: Preparation of Zircaloy samples for pre and post-irradiation *in-situ* TEM analyses

Progress Made: Before accomplishing the preparation methods for Zircaloy samples, ultrafine Zr and sputtered Zr samples were tried. This step will help understand the effect of the 2.5% alloying elements on the behavior of Zircaloy-4 (PWR cladding material) when compared to pure Zr. It was tough to get hold of the Zircaloy samples initially from suppliers as those suppliers focus on mainly bulk supplies. Finally a supplier was found and Zircaloy materials were ordered and were received in the third week of September 2014. Zircaloy-4 samples were prepared for TEM analyses.

Task 2: Setup imaging and characterization procedures using X-ray diffraction, EBSD, SEM, and LEAP to understand the effect of various environments on Zircaloy microstructure

Progress Made: Initial progress has been made for the prepared Zr samples which are analyzed using TEM, pre and post irradiation.

Setups and experimental optimizations/preparations for the SEM and FIB characterizations were performed by first irradiating and post characterizing Zr samples. The reason of choosing Zr samples is outline in Task 1 progress.

Task 3: Design and nanofabricate *in-situ* TEM testing devices for coupled thermal and mechanical property measurements and integration with specimens obtained from milestone M1

Progress Made: The proposed MEMS chip is developed and demonstrated on 100 nm thick Zr thin film specimens. In-situ TEM tests showed triple point junction void formation as a mechanism for low fracture strain of the nano-crystalline (grain size < 10 nm) specimens. The specimens also show effects of electron irradiation compared to experiments performed under optical microscopes. The MEMS chip was integrated with micro-heaters to perform thermal conductivity measurement. This was demonstrated on the 100 nm thick Zr specimens as function of temperature. Remarkable size effect (25% reduction in thermal conductivity) was observed at 180 °C. Integration of such measurements with Zircaloy will be performed in Quarter 4. Details regarding those are mentioned in this report at the end of milestone description.

Task 4: Setup Zircaloy samples obtained from Task1 to various test environments containing oxygen, water, CO_2, sodium containing oxygen, and LiOH solutions and perform high temperature and chemistry dependent nano/micro thermomechanical measurements based on surface enhanced Nanomechanical Raman spectroscopy

Progress Made: Temperature dependent (upto 450 degree C) measurements of mechanical properties as a function of irradiation for initial irradiated Zr microstructures have now been performed based on indentation tests. The same measurements for Zircaloy have been started, The measurements have been incorporated into microstructure dependent property dataset using a high temperature viscoplastic model that has been developed based on the dataset. Since the model is for pure Zr, the model and dataset now provide a good basis for understanding the influence of compositional issues in Zircaloy (e.g. variation between Zircaloy2 vs. Zircaloy4 chemistry as a function of microstructure) on the measured environment and temperature dependent mechanical and thermal properties and their correlation. The current focus of experiments now is on exposing recently obtained Zircaloy samples in different chemical environments and on extending the Zr microstructural measurements to Zircaloy. Correspondingly, the high temperature microstructure dependent model developed for polycrystalline Zr will be modified to accommodate Zircaloy. Once developed the model will be used to predict Zircaloy mechanical properties under different measurement conditions and correlate those to thermal property measurements by Tomar and Haque. The

PI also had a conversation with TPOC (Dr. Unal) and will also perform environment dependent thermomechanical measurements on HT-9 and/or APMT steel as well as UO_2 substitutes. Details regarding those are mentioned in this report at the end of milestone description.

PROJECT REPORT NARRATIVE

The following are yearly milestones, along with deliverable and criterion for completion

YEAR 1 (1/14 TO 12/14)

Zr processing and Zircaloy processing, Sample characterization as a function of irradiation, Initial TEM based measurements of coupled thermomechanical properties in Zr, Nanomechanical and Micromechanical High Temperature Measurements of Zr Samples 12/31/2014

Deliverable Title	Zr and Zircaloy with controlled microstructure, Establishment of experimental protocols
	Initial establishment of experimental and processing protocols
Criteria for Completion	Electron microscopy based characterized microstructures; Database relating microstructure with multiphysical properties of Zr and Zircaloy Interface

Task 1: Preparation of Zircaloy samples for pre and post-irradiation *in-situ* TEM analyses

Progress Made: Before accomplishing the preparation methods for Zircaloy samples, ultrafine Zr and sputtered Zr samples were tried. This step will help understand the effect of the 2.5% alloying elements on the behavior of Zircaloy-4 (PWR cladding material) when compared to pure Zr. It was tough to get hold of the Zircaloy samples initially from suppliers as those suppliers focus on mainly bulk supplies. Finally a supplier was found and Zircaloy materials were ordered and were received in the third week of September 2014. Zircaloy-4 samples were prepared for TEM analyses.

Task 2: Setup imaging and characterization procedures using X-ray diffraction, EBSD, SEM, and LEAP to understand the effect of various environments on Zircaloy microstructure

Progress Made: Initial progress has been made for the prepared Zr samples which are analyzed using TEM, pre and post irradiation.

Setups and experimental optimizations/preparations for the SEM and FIB characterizations were performed by first irradiating and post characterizing Zr samples. The reason of choosing Zr samples is outline in Task 1 progress.

Task 3: Design and nanofabricate *in-situ* TEM testing devices for coupled thermal and mechanical property measurements and integration with specimens obtained from milestone M1

Progress Made: The proposed MEMS chip is developed and demonstrated on 100 nm thick Zr thin film specimens. In-situ TEM tests showed triple point junction void formation as a mechanism for low fracture strain of the nano-crystalline (grain size < 10 nm) specimens. The specimens also show effects of electron irradiation compared to experiments performed under optical microscopes. The MEMS chip was integrated with micro-heaters to perform thermal conductivity measurement. This was demonstrated on the 100 nm thick Zr specimens as function of temperature. Remarkable size effect (25% reduction in thermal conductivity) was observed at 180 °C. Integration of such measurements with Zircaloy will be performed in Quarter 4. Details regarding those are mentioned in this report at the end of milestone description.

Task 4: Setup Zircaloy samples obtained from Task1 to various test environments containing oxygen, water, CO_2, sodium containing oxygen, and LiOH solutions and perform high temperature and chemistry dependent nano/micro thermomechanical measurements based on surface enhanced Nanomechanical Raman spectroscopy

Progress Made: Temperature dependent (upto 450 degree C) measurements of mechanical properties as a function of irradiation for initial irradiated Zr microstructures have now been performed based on indentation tests. The same measurements for Zircaloy have been started, The measurements have been incorporated into microstructure dependent property dataset using a high temperature viscoplastic model that has been developed based on the dataset. Since the model is for pure Zr, the model and dataset now provide a good basis for understanding the influence of compositional issues in Zircaloy (e.g. variation between Zircaloy2 vs. Zircaloy4 chemistry as a function of microstructure) on the measured environment and temperature dependent mechanical and thermal properties and their correlation. The current focus of experiments now is on exposing recently obtained Zircaloy samples in different chemical environments and on extending the Zr microstructural measurements to Zircaloy. Correspondingly, the high temperature microstructure dependent model developed for polycrystalline Zr will be modified to accommodate Zircaloy. Once developed the model will be used to predict Zircaloy mechanical properties under different measurement conditions and correlate those to thermal property measurements by Tomar and Haque. The PI also had a conversation with TPOC (Dr. Unal) and will also perform environment dependent thermomechanical measurements on HT-9 and/or APMT steel as well as UO_2 substitutes. Details regarding those are mentioned in this report at the end of milestone description.

CURRENT OVERALL STATUS OF YEAR 1 MILESTONES: Milestones completed.

YEAR 2 (1/15 TO 12/15)

Establishment of Irradiation and Temperature effects on Zircaloy microstructures in Sandia I3 TEM,Measurement of Irradiation and Temperature influence on Zircaloy Thermal and Mechanical properties 12/31/2015

Deliverable Title	Zircaloy Temperature and Irradiation Dependent Thermal and Mechanical Coupling Properties
Criteria for Completion	Successful experimental protocols, dataset that verifies available literature, New Dataset that predicts how microstructure in Zircaloy correlates to Multiphysical properties

Task 5: *In-situ* TEM measurements of thermal conductivity as function of irradiation and mechanical stressing,

Year 2 Goal: This task has been completed.

In-situ TEM tests were performed on evaporated as deposited and Zr+ irradiated specimens (collaboration with Sandia National Laboratories) 100 nm thick, 10 micron wide and 100 micron long. The samples were exposed to Zr+ 800KeV at 4.5nA with doses of 3E10, 3E11 and 3E+12 (collaboration with Sandia National Laboratories). Figure S2.13 shows a typical stress-strain diagram for as deposited specimen. The lack of plastic deformation is due to the small grain size (~10 nm) that is unable to accommodate dislocations. Also the freestanding film has surfaces through which the defects can escape, causing the dislocation starvation. Diffusive plasticity also doesn't take place at room temperature because Zr is a very high melting point material.

Collaborating with University of Dayton, we were able to sputter deposit Zircaloy thin films on the MEMS devices. Control of microstructure of the specimens was performed in-situ in TEM. Our

previous finding was that up to 100 times grain size increase by thermo-electro-mechanical annealing was possible. In this period, we worked on the zircaloy thin films. For zircaloy, remarkable grain growth due to heating is about shown inside the TEM. Here the grain size increased about 10 times after heating to 150 ºC. The extent of such grain growth is very obvious in the diffraction patterns. The grains also showed extensive dislocations inside. The results suggest that nanocrystalline zircaloy has higher grain boundary mobility, which gives rise to the high temperature sensitivity.

Thermal conductivity for Zr specimens as function of applied strain was measured. Thermal conductivity decreases as we increase the strain. This behavior can be ascribed to the nanocrystalline microstructure of these thin films. When the geometric dimension of specimen or the grain sizes go down to nanoscale, it becomes increasingly difficult for the grain interiors to accommodate the external deformations. Therefore, mechanical deformation mechanisms for grain sizes smaller than phonon mean free path (about 20 nm) are basically different from the bulk ones which is not only due to absence of dislocations but also very high volume fraction of the grain boundaries. In absence of dislocations in the grain interior, the grain boundaries primarily accommodate the applied strain. To accomplish this, the grain boundaries must slide, rotate or emit dislocations that also move along the grain boundaries as strain is applied. The scattering of electrons by grain boundaries will be enhanced by these grain motions. Therefore we hypothesize that the motion of grain boundaries resulted from strain localization is the primary mechanism behind thermal-strain coupling

Finally, we measured the thermal conductivity of the as function of irradiation. About 38% reduction of thermal conductivity is seen at 3.26×10^{14} ions/cm^2 radiation. We hypothesize that the effect of irradiation is most prominent at the grain boundaries, which are easier to knocked out by the ions. Pronounced disorder at the grain boundaries lead to the reduction in thermal transport

A major obstacle for the proposed research was integration of electron transparent zircaloy specimen (sectioned from the bulk) with the MEMS devices for in-situ TEM testing. The issue was the planarity of the specimen (irrespective of FIB sectioned or electropolished or ion milled). Since the MEMS devices are highly planar, any warpage in the specimen makes it challenging to fix both ends of the specimen on the two planar jaws of the MEMS. In this quarter, we have resolved this issue and have demonstrated it on gamma irradiated zircaloy specimens.

Task 6: *In-situ* Nanomechanical and micromechanical SERS based measurements of environment dependent thermal conductivity, diffusivity as a function of stress/strain
Year 2 Goal: This task has been completed.

One hour prior to corrosion testing, all samples were polished with SiC paper. Immediately before electrolyte submersion, the samples were degreased with a solvent and rinsed with distilled water. These methods are in accordance with the ASTM G5. Prior to mechanical testing, samples were again degreased with a solvent and rinsed with distilled water. No further polishing are performed to ensure corrosion effects are accurately represented. So far, we have performed two corrosion tests. One is unirradiated zircaloy sample, the otherone is irradiated zircaloy sample. From compare their corrosion test data, we can find some clue about how does the radiation affect zircaloy corrosion

resistence. In Fig. 3.17, we showed the corrosion rate of unirradiated sample in both palarization resistance model and Tafel model. In Fig.3.19, we compared the corrosion rate of unirradiated and irradiated samples in both palarization resistance model and Tafel model. It's obvious that zircaloy samples after irradiation will have a higher corrosion rate. Which consistents with common sense and our expection, radiation will reduce the material's corrosion resistance.

The micro-Raman method is a noncontact and nondestructive method for thermal conductivity measurements. In our case, we want to use micro-Raman method to measure thermal conductivity of the irradiated zircaloy specimen. However, there's a thin silicon film on our specimen, which means that the film thermal conductivity, film thickness, substrate thermal conductivity and interface thermal resistance all have effects on the heat transfer process. A computational model was developed for implementation into MOOSE for incorporating these effects. Computational model closely predicted the experimental thermal conductivity fields in Zircaloy sampleas as a function of stress and temperatures.

Experiments at microstructure level are time consuming. In order to incorporate the experimental results in a predictive manner as new phase field model was developed that incorporates microstructure dependency of the research results. This model is being interfaced with MARMOT.

Task 7: Identification of key microstructural parameters that link irradiation induced damage and environment dependent thermomechanical coupling based on quantified data
Year 2 Goal: This task has been completed.
TEM measurements specifically focused on thin film specimen subjected to irradiation. Samples, mainly with ion-irradiation were analyzed. Due to sample preparation limitations highlighted in task 5, specific type of GB's/grains and their correlation with irradiation damage was not possible to be obtained with using TEM. Instead a combined phase-fields modeling and nanomechanical SERS based approach was adopted. Specific microstructure related trends were found in the initial phase. These studies ae not getting extended as part of task 10 in year 3.

CURRENT OVERALL STATUS OF YEAR 2 MILESTONES: Milestones completed.

Year 3 (1/16 to 12/16)

Correlation of microstructure change prediction of Zircaloy with established literautre studies as well as with Marmot based predictions, Establishment of user subroutine data that correlates thermo-mechanical multiphysics, 12/31/2016

Deliverable Title Multiphysical Property User subroutine

Criteria for verified user subroutine for use in Bison and Marmot to predict
Completion microstructure influenece on multiphysical properties

Task 8: Combine feedback from TEM thermomechanical property measurement experiments and simulations to provide uncertainty quantified dataset that links microstructure damage to irradiation with measured levels of confidence.
Year 3 Goal: This task has been completed as reported here.

Task 9: *In-situ* Nanomechanical and micromechanical SERS based measurements to understand the effect of temperature up to 1000 ºC on environment dependent coupled thermal and mechanical properties.
Year 3 Goal: This task has been completed as reported here..
Task 10: Establishment of microstructure-irradiation-stress-environment-temperature correlations using Bayesian uncertainty quantification procedures that affect separate effect multiphysics properties of Zircaloy. Development of empirical relations predicting such correlations.
Year 3 Goal: This task has been completed as reported here..

CURRENT OVERALL STATUS OF YEAR 3 MILESTONES: Project is complete.

PROJECT MILESTONE STATUS CHART

13-5292 Correlating Thermal and Mechanical Coupling Based Multiphysics Behavior of Nuclear Materials Through In-Situ Measurements

Focus	Description	Q1	Q2	Q3	Q4	Q5	Q6	Q7	Q8	Q9	Q10	Q11	Q12
1	*In-situ* TEM: Examine Radiation Damage	Tasks 1 &2 Complete				This Task is not continued in years 2 and 3 with focus shifting on Focus2 and Focus3 to feed into overall proposal goal in task 4							
2	*In-situ* TEM: thermal and mechanical property Measurements	Task 3 Complete				Task 5 Complete				Task 9 Complete			
3	*In-situ* Nanomechanical and Micromechanical SERS: Environment/Temperature Effects	Task 4 Complete				Task 6 Complete				Task 10 Complete			
4	Establishing Microstructure-irradiation-temperature-stress-environment relationship and Uncertainty Quantification	Task 4 Complete				Task 7 Complete				Task 8, Task 11 Complete			

Project Start Date: Jan 01, 2014, Ends: December 31, 2016

TECHNICAL DESCRIPTION OF PROJECT ACCOMPLISHMENTS

SECTION 1 (S1)

(Year 1 only): Sample Preparation and Irradiation Effect on Microstructure Characterization (Dr. El-Atwani)

STATUS:

Task 1: Preparation of Zircaloy samples for pre and post-irradiation *in-situ* TEM analyses (COMPLETED)

Task 2: Setup imaging and characterization procedures using X-ray diffraction, EBSD, SEM, and LEAP to understand the effect of various environments on Zircaloy microstructure (COMPLETED)

S1.1 Introduction

Irradiations and post characterization experiments were performed first on Zr samples. This step will help understand the effect of the 2.5% alloying elements on the behavior of Zircaloy-4 (PWR cladding material) when compared to pure Zr. Irradiation flux measurements and sample temperature calibrations were performed at different energies prior to the irradiation experiments. Irradiations were performed with two different energy regimes1: non-displacment energies and displacement energies. Time was also dedicated to optimize transmission electron microscopy (TEM) sample preparation conditions via electropolishing technique. This step is crucial to prepare TEM samples for the in-situ TEM/irradiation experiments (Year 2). In addition, Zircaloy-4 samples are being prepared for irradiation, and a setup is built by one of our collaborators (Dr. Mert Efe) to prepare ultrafine (UF) and nanocrystalline (NC) Zircaloy-4 samples for comparison with the commercial Zircaloy-4 samples.

S1.2 Experimental Procedure

Two types of Zr samples were used in this work: rolled and annealed vs rolled. The samples were mechanically polished before irradiation. Irradiations were performed in the Center of Materials Under extreme Environment (CMUXE) at Purdue University. Room temperature irradiation of the samples was performed in the Interaction of Materials with Particles and Components Testing (IMPACT) experimental facility using gridded ion source. The ion flux was 1 $x10^{20}$ m^{-2}.High temperature (350 and 700 ^{0}C) helium (He) irradiations were performed in the high flux lab at CMUXE using gridless end-hall ion source. The ion flux was 1 $x10^{20}$ m^{-2}. All samples were irradiated to a total fluence of 5 $x10^{22}$ m^{-2}.

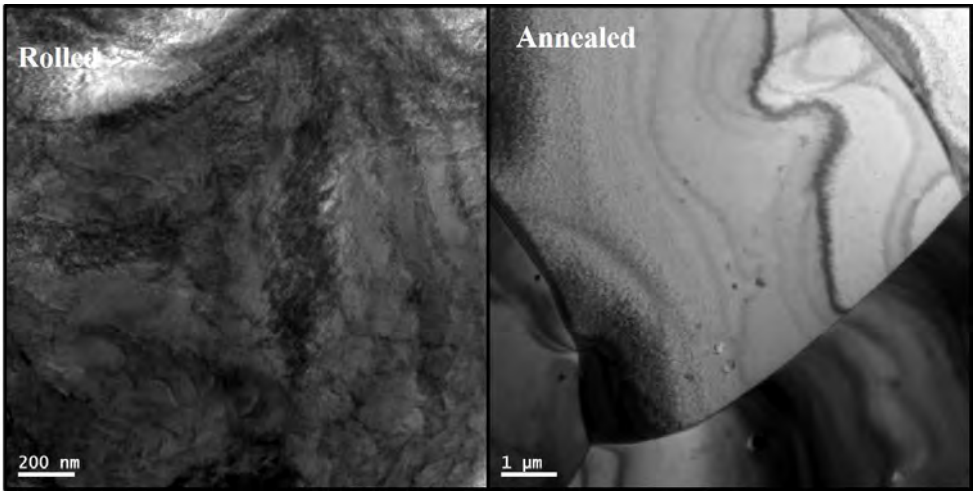

Figure S1.1: TEM micrographs of the rolled and the annealed samples.

Morphology investigation of the sample after irradiation were performed in Birck Nanotechnology Center at Purdue University using Hitachi S4800 FESEM. Cross section imaging was performed using FEI xT Nova NanoLab Dual Beam focused ion beam/scanning electron microscope (FIB/SEM). For pre-irradiation transmission electron microscopy characterization, FEI Titan 80/300 field emission TEM, operating at 300 kV or 200 KV FEI Technai LaB6 TEM was used

S1.3 Results

Figure S1.1 shows TEM micrographs of both types of samples used in this study. The rolled samples has ultrafine grains with mostly non-sharp grain boundaries decorated by dislocation cells. The annealed samples has large grains of about 5-10 µm. SEM micrographs of the samples prior to irradiation is shown in Figure S1.2. Little morphological effects can be seen in the images due to mechanical polishing of the samples.

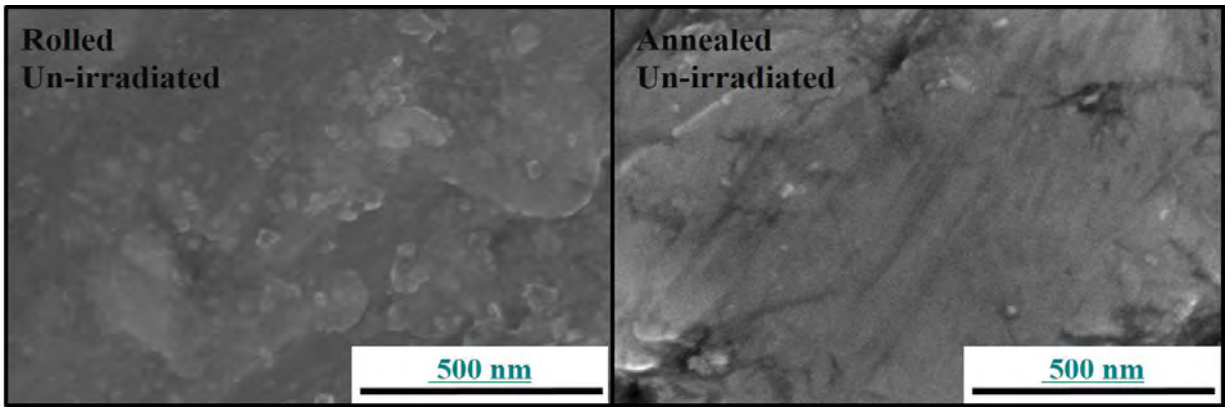

Figure S1.2: SEM micrographs of the un-irradiated rolled and annealed samples. The micrographs show little effect on the sample morphology due to polishing.

Figure S1.3 shows both samples morphologies after He irradiation at 100 eV and RT. Small blisters and relatively large holes were observed. The damage is more apparent on the rolled sample. Using TRIMJF Ziegler (2010), calculations, no displacement should occur with 100 eV He

irradiation. However, defects can still form due to bubble formation and possible loop punching, Minyou (2005), or trap mutation, Caspers et al. (1978), during bubble growth. Trap mutation is defined as the process from which interstitials are generated due to bubble growth, and loop punching is a similar process from which dislocation loops are generated from over pressurized bubbles. It should be noted, however, that defect migration (especially vacancies) should be slow at RT. Therefore, small bubbles should form, and the resulting change in microstructure should be small too.

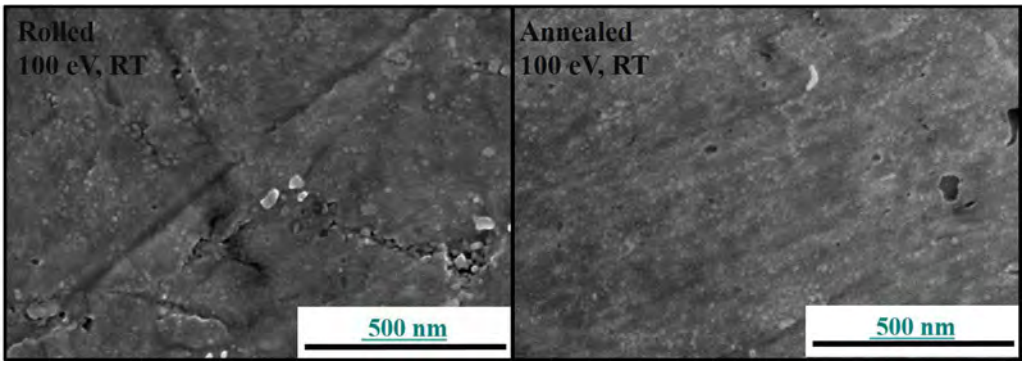

Figure S1.*3*: SEM micrographs of both samples irradiated with 100 eV He at RT.

At higher temperatures (temperatures relevant to BWR reactors, defect migration should be enhanced. Vacancy cluster formation is then expected and larger bubble should form. Figure S1.4 shows SEM micrographs of both samples irradiated with 100 eV He at 350 ^{0}C. Small blisters/nanostructure formation is observed in the rolled sample with facetted voids on the surface possibly due to facetted bubbles bursting on the surface. Less damage is observed on the annealed sample despite high density of surface voids. Residual stresses involved in the rolled samples can enhance the microstructural changes when combined to bubble (lateral stresses), Behrisch et al. (1975), and He accumulation (residual stresses), Som et al. (1998). El-Azab and Liang‡ (2003) suggested stress related surface diffusion to play a role in the nanostructure formation on metal oxides. Moreover, high density of dislocations and dislocation cells (Figure T1&2.1) in the cold rolled samples can serve as nucleation bubble sites due helium 1D trapping effect on dislocations, Singh and Foreman (1974).

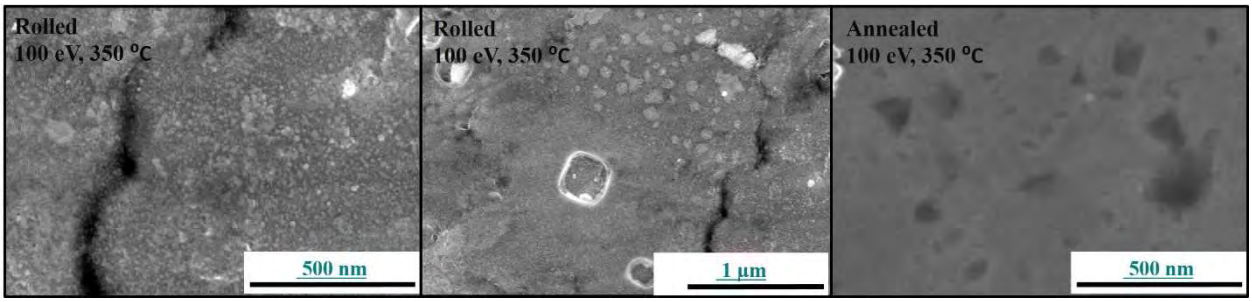

Figure S1.*4* SEM micrographs of both samples irradiated with 100 eV He at 350 ^{0}C

Further increase in the temperature (temperatures relevant to PWR), showed larger damage. Figure S1.5 shows SEM micrographs of both samples irradiated with 100 eV at 700 ^{0}C. Higher

density of blisters is observed in the rolled sample with intergranular micro-crack formation. At 700 ^{0}C, recrystallization is expected to occur on the rolled sample. Bubble formation on the grain boundaries along with irradiation enhanced diffusion can results in enhanced grain boundary grooving and thus micro-crack formation, El-Atwani et al. (2013).

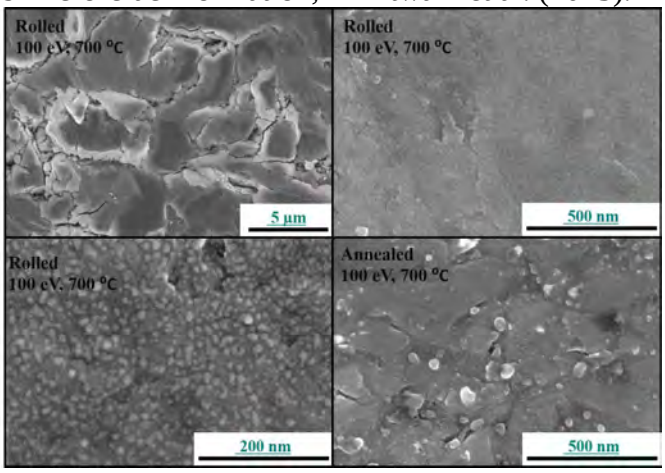

Figure S1.5: SEM micrographs of both samples irradiated with 100 eV He at 700 ^{0}C.

Increasing the irradiation energy to 1 keV led to larger damage formation on both samples at RT. Figure S1.6 shows SEM micrographs of both samples irradiated at 1 keV and RT. Large surface voids and small blisters-bubble formation are formed on both samples. At 1 keV, defects can be generated (vacancies and interstitials). However, migration of vacancies could be limited at RT. Comparison of both samples at 1 keV could then be better made at higher temperatures (ongoing work).

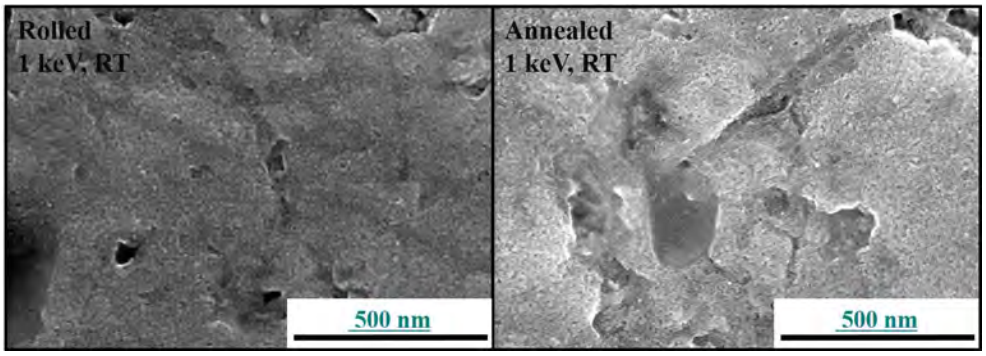

Figure S1.*6* SEM micrographs of both samples irradiated with 1 KeV He at RT.

For better comparison between both samples, cross-section images were taken from both samples after irradiation with 1 keV and 100 eV He at RT and 700 ^{0}C respectively, Fig. S1.7. The thickness of the damages layer was found to be comparable in both samples in the 1 keV irradiation at RT case.

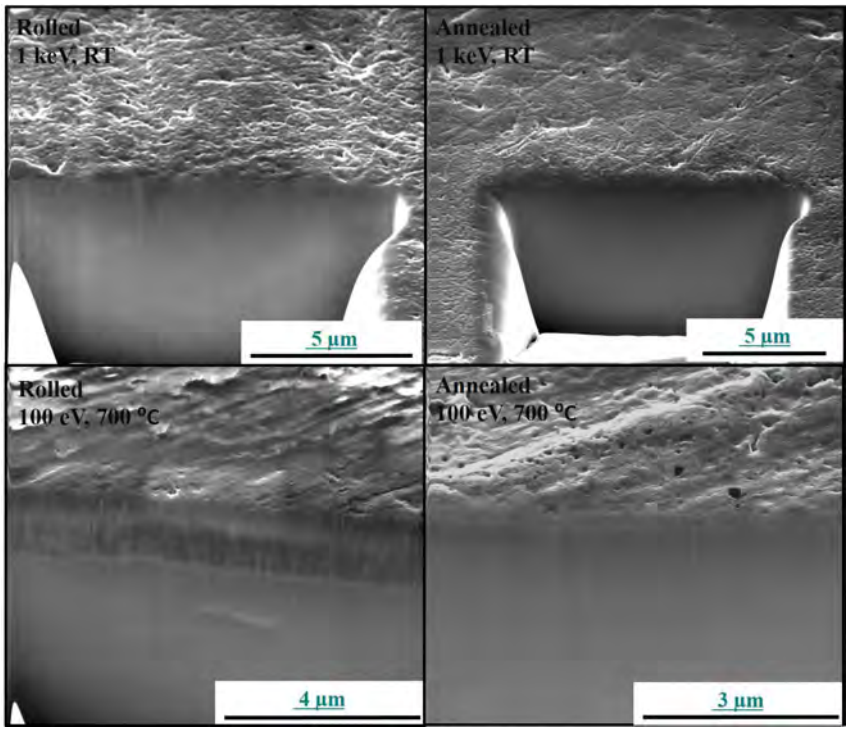

Figure S1.*7*: cross-sectional SEM images of the samples irradiated with 1 keV He at RT and 100 eV He at 700 ^{0}C

Little contrast below the damaged layer in the rolled sample demonstrates the microstructure of the sample to be of ultrafine type. AT 700 ^{0}C (100 eV He irradiation), no contrast is observed due to recrystallization of the sample. At this temperature, however, the thickness of the damages layer is found to be higher in the rolled sample. The several micron damaged layer is much larger than what is expected from He penetration depth (10 nm) from TRIM simulations.

Electropolishing of zircaloy-4 (TEM sample characterization)

Figure S1.8 shows bright-field TEM images of cold rolled zircaloy-4 sample. This sample was performed using the optimum conditions for TEM sample prepration (discussed in the experimental part). The grain size was foud to be several µm. As expected, the dislcoation density is high. Few samples (including this one) were prepared for in-situ TEM irradiation. However, this cold rolled commercial sample is not suitable for grain refinement (ultrafine and nanocyrstalline) study purposes (effect of decreasing grain size) due to relatively large grain size. Therefore, ultrafine and nanocrstalline samples should be prepared using other novel techniques such as orthogonal machining discussed in the proposal. Figure S1.9 shows bright-field TEM images of cold rolled + annelaed zircaloy-4 sample. As expected, the grain size is very large which needs low magnification characterization tools such optical microscopy for accurate measurements. Few samples (including this one) were prepared for in-situ irradition experiments. Such samples can be used to compare with

ultrafine and nanocrystalline samples response to irradiation during in-situ TEM/irradiation and ex-situ irradaition/morphology characterization experiments.

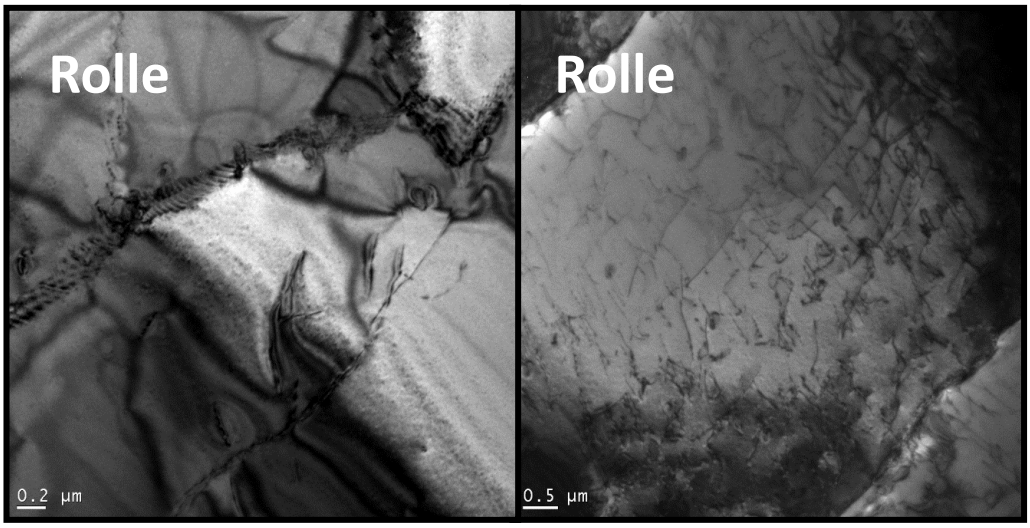

Figure S1.8 : Bright-field TEM image of commercial cold rolled zircaloy-4 sample.

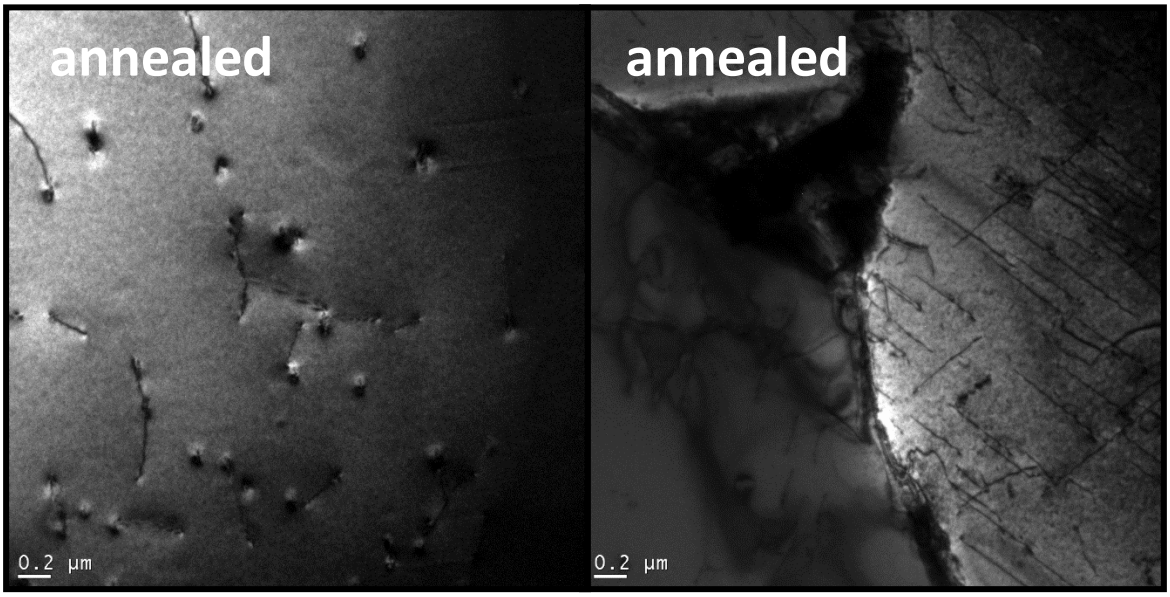

Figure S1.9: Bright-field TEM image of commercial cold rolled + annealed zircaloy-4 sample.

S1.4 Summary

Despite the smaller grain size, the cold-rolled Zr samples showed larger damage, interaction depth and irradiation response than the annealed (stress relieved) samples. These results shed the

light on the effect of residual stresses on the behavior of cladding materials exposed to severe environment. The results confirm that the refinement of the grains to the ultrafine regime did not lead to enhanced irradiation tolerance possibly due to high density of dislocations on the strained material (cold-rolled)

S1.5 Ongoing work

The following work is being performed currently as an extension of this task as described in in section 2:

- To simulate neutron damage (damage through transmutation process), neutron irradiation will be performed at Penn-State rector.
- Irradiated samples are with Dr. Aman and Dr Tomar for correlating the irradiation results with the resulting thermal and mechanical properties.

SECTION 2 (S2)

In-Situ TEM Measurements of Thermomechanical Coupling (Dr. Aman Haque)

STATUS:

Task 3: Design and nanofabricate *in-situ* TEM testing devices for coupled thermal and mechanical property measurements and integration with specimens obtained from milestone M1, (COMPLETED)

Task 5: *In-situ* TEM measurements of thermal conductivity as function of irradiation and mechanical stressing, (COMPLETED).

Task 7: Identification of key microstructural parameters that link irradiation induced damage and environment dependent thermomechanical coupling based on quantified data, (COMPLETED).

Task 8: Combine feedback from TEM thermomechanical property measurement experiments and simulations to provide uncertainty quantified dataset that links microstructure damage to irradiation with measured levels of confidence, (COMPLETED).

Task 10: Establishment of microstructure-irradiation-stress-environment-temperature correlations using Bayesian uncertainty quantification procedures that affect separate effect multiphysics properties of Zircaloy. Development of empirical relations predicting such correlations, (COMPLETED).

Summary of Activities & Findings: In the first year of this project, the followings were achieved,

(i) In-situ TEM Mechanical Testing: We developed an in-situ TEM mechanical testing setup and demonstrated it on 100 nm thick sputtered freestanding Zr thin films with average grain size 5-10 nm. Stress-strain data was obtained both under transmission electron and white light microscope environments. The measured Young's modulus of 85-90 GPa, falling very close to the bulk value (90 GPa) validates the experimental protocol. The critical finding is the *remarkably strong effect of electron irradiation on the mechanical properties*, that the co-PI (Haque) did not see with other metals, such as aluminum, nickel and platinum in his prior studies. The in-situ TEM tests showed yielding around 400-500 MPa and fracture strain around 1.5-2% strain, whereas white light tests showed mostly linear elastic behavior till fracture at around 0.9-1.1 GPa. In comparison, ultra-fine grained Zr (>100nm grain size) in the literature shows yield strength of 500 MPa and 15% fracture strain.

(ii) In-situ TEM Grain Growth: By passing dc current through the specimen, we were able to grow the grain from 5-10 nm to up to 500 nm. The motivation is to achieve control over the microstructure so that the microstructure-property relationship could be studied in-situ in TEM. Such large grain growth, however, is accompanied by significant curling of the tensile specimen (curled from a flat plate shape to almost cylinder shape), which made the TEM observation and measurements difficult. We hypothesize that the combination of externally applied mechanical and electro-migration stress, in conjunction with temperature induced softening result in such curling of the material.

(iii) Thermal Transport Measurement: Using microheaters (integrated with the in-situ TEM testing chip) and an infrared microscope, we measured thermal conductivity of the above mentioned Zr specimens. The experimental value of 20 W/m-K at room temperature matches very close to the literature bulk value of 20-22 W/m-K, which validates the developed technique. The critical finding is the very *strong temperature dependence of thermal conductivity of nanocrystalline (<10 nm grain size) Zr specimen*. At only 180 °C, the thermal conductivity decreased to 15 W/m-K (25% decrease), whereas the literature shows negligible change at

around 19-20 W/m-K. We hypothesize that the significant fraction of grain boundary and triple point atoms in the nanoscrystalline form enhances the electron scattering at higher temperatures, which may reduce thermal conductivity.

The milestones for Year 2 are summarized below for the co-PI (Haque).

Period	Milestones	Status
Year 2 Months 1-3	I. Adapt the MEMS-based in-situ TEM testing technique in Year 1 to Zircaloy specimens.	Significant progress has been made in adapting the MEMS devices with the bulk specimens. Residual stress after thinning to 200 nm or below still curls the specimen making it challenging because the MEMS devices need high planar specimens. An alternate path of sputtering of Zircaloy has been developed.
Year 2 Months 4-6	II. Control microstructure of the specimens (grain size and defects) in-situ in TEM using thermal, stress-assisted and electron flow assisted annealing). III. In-situ TEM measurements of mechanical and thermal properties as function of grain size	This task was performed and presented previously on pure Zr. New results on zircaloy thin films are presented. Up to 100 times grain size increase by thermo-electro-mechanical annealing was shown inside the TEM. Both mechanical and thermal properties were measured as function of 800 keV Zr+ ion irradiation. Results are presented in this report.

In the following, first, the year 1 work is described, followed by year 2 work.

S2.1 Introduction: The objectives of the first year of this research as setup to develop and demonstrate experimental capabilities for measuring mechanical and thermal properties as well as their coupling in nuclear materials. The focus of the co-PI (Haque) activity was in-situ TEM measurements, so that microstructural aspects could be quantified. A unique feature of the developed setups is the quantitative property measurements, so that the microstructure-property relationship is based on direct observation and measurement, which can play invaluable role in developing models that predict properties. Therefore, it is important to note that the experimental setups presented here are capableto measuring the properties such as Young's modulus, yield strength, fracture strain, thermal conductivity and not simply TEM observation under arbitrary straining or heating. To achieve the above-mentioned objective the following three tasks were pursued in Year 1.

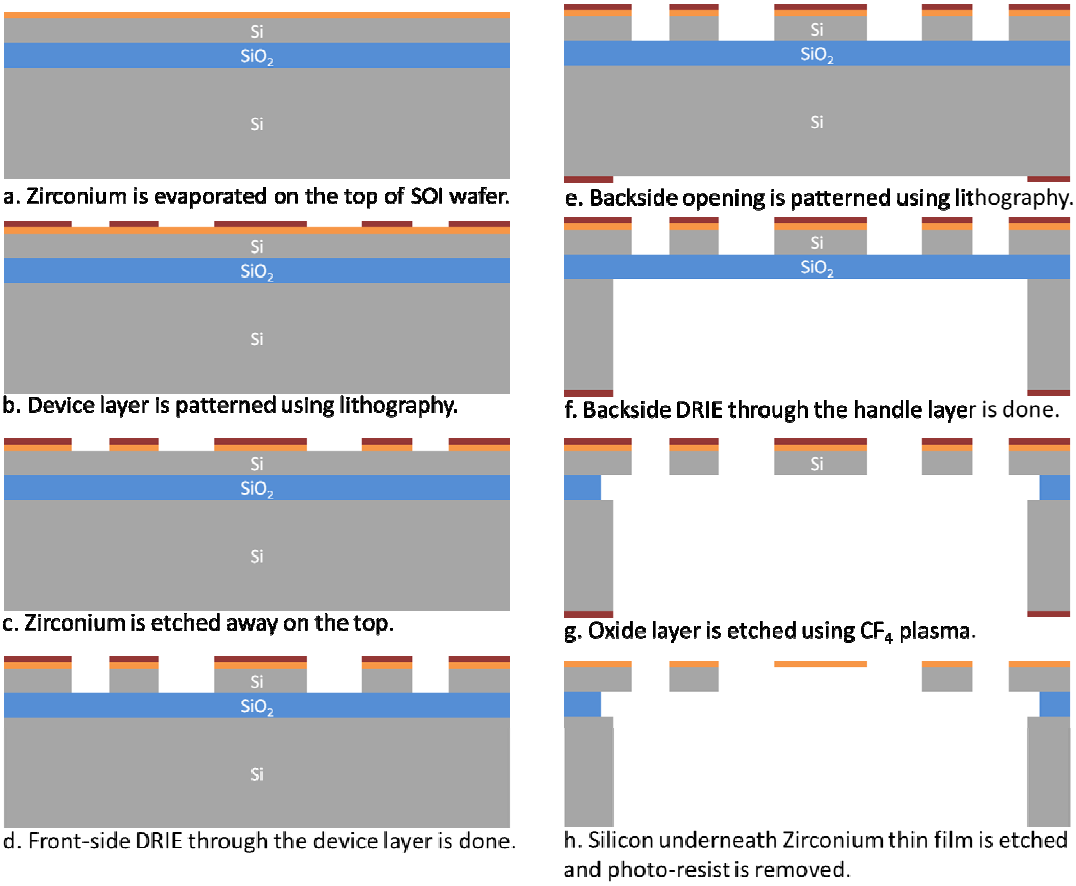

Figure S2.1. Nanofabrication process of the MEMS device depicted step by step

S2.2: In-situ TEM Mechanical Testing In the first year of this research project, we developed an in-situ TEM testing setup consisting of a micro-electro-mechanical systems (MEMS) based device nanofabricated from a Silicon-On-Insulator (SOI) wafer. Zr (or any desired material) layer of 100nm thickness is deposited using evaporation on the top of the device layer. The device design is then patterned using standard photolithography procedure. The unmasked region of Zr is etched exposing the Silicon device layer. The device layer is then etched using Deep Reactive Ion Etch (DRIE) technique. The back side design of the device is patterned on the handle layer and the whole handle layer Silicon is etched away using the DRIE. The Buried Oxide (BOX) layer is then removed using CF_4 plasma. The final step is to make the Zr sample freestanding. This is done by etching the Silicon underneath the sample using SF_6 plasma while the rest of the device is masked using a physical mask. The whole process is depicted in Figure S2.1. Figure S2.2 shows SEM image of a device and a TEM image of the as prepared specimen. The chip size is 3mm x 5 mm, which fits a custom electrical biasing holder. Since the actuators and heaters are built-in to the MEMS chip and powered by electrical connects, all the experiments can be carried by a biasing holder. Here, the bright-field TEM image shows that the grain size in the as-deposited condition is very small (5-10 nm). This is also reflected in the electron diffraction pattern, showing diffused rings representing various

crystallographic planes.

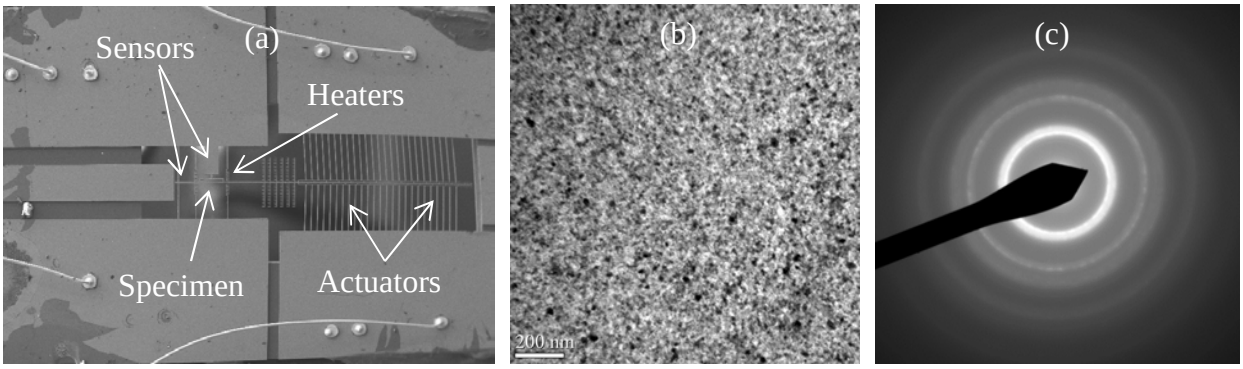

Figure S2.2. (a) SEM image of an in-situ TEM test chip (also equipped with micro heaters for thermal conductivity measurements) with co-fabricated Zr specimen, (b) bright-field TEM image of the as-deposited specimen and (c) TEM electron diffraction showing the nano-crystalline structure.

S2.2.1 Experimental Results: In-situ TEM tests were performed on the as-deposited Zr specimens. The 100 nm thick specimens were about 10 micron wide and 100 micron long. Figure S2.3a shows a typical stress-strain diagram, where yield stress is around 500 MPa and fracture stress and strain are about 0.9 GPa and 1.5% respectively. This shows remarkable grain size effect when compared to the ultrafine grain Zr (UFG Zr) literatureTabachnikova et al. (2008), which shows almost no strain hardening beyond 500 MPa stress. However, our nanocrystalline Zr (nc Zr) suggests also has very small fracture strain (<2%) compared to the UFG Zr (15%). Our in-situ TEM experiments on nc Zr suggest that there may not be any plasticity in the material. Rather, strain incompatibility among neighboring grains may pronounce the grain boundary stress, creating voids at the grain boundaries. Generation of these voids may explain the deviation from linear elastic behavior that appears as pseudo strain hardening. In-situ TEM observation seems to support this hypothesis, since we did not see any evidence of dislocation-based plastic deformation mechanism. At the same time, we saw numerous void like structures in the specimen on the on-set of failure. This is shown in Figure S2.3b.

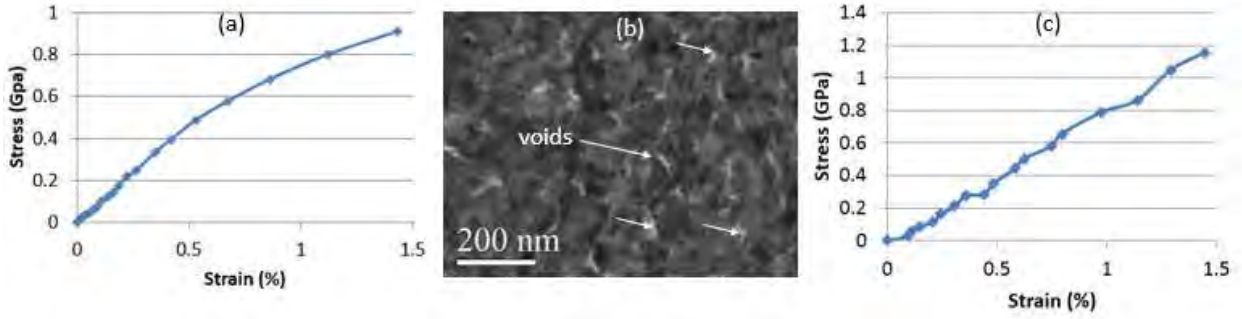

Figure S2.3. (a) Representative stress-strain diagram for a nc Zr specimen measured in situ inside a TEM (b) nanoscale voids appears at the grain boundaries at the onset of fracture (c) Stress-strain diagram in absence of electron irradiation

An interesting finding of this study is the strikingly different mechanical behavior of the nc Zr

under white light microscopy. These in-situ optical microscope experiments were used in digital image correlation (DIC) technique to measure the stress-strain behavior. Figure S2.3c shows a representative stress strain diagram, which highlights remarkable difference between materials behavior with and without electron beam exposure. We hypothesize that electron irradiation (in-situ TEM) at 300 kV results in void swelling Faulkner and Woo (1980) which is absent in white light microscopy. As a result, the loss in strength (pseudo strain hardening in Figure 3b) is also minimum, and the material can sustain higher strength. In either cases, the fracture strain is very low compared to the value for ultra-fine grained Zr (around 15%). This is because in out <10 nm grain size, deformation is mostly localized in the grain boundaries and triple points and the deformation does not have any plastic mechanism to relax that is available for >100 nm grain sizes. Rather, the triple points act as localized stress-raisers and initiate micro-cracks due to stress inhomogeneity in the neighboring grains. As a result, even though the strength of our nc Zr specimen is almost double of that reported in the literature for ultra-fine grained material, the fracture strain is also much lower.

S2.2.2 Task 2: In-situ TEM Grain Growth The second task pursued was in-situ TEM grain growth of the nc Zr specimens. The motivation for this task was the ability to actively control the microstructure, so that the overall goal of microstructure-property relationship can be quantified. To grow the grains, we perform electrical annealing, where modest DC current density is applied to the specimen. Since the specimen is freestanding, it experiences a temperature gradient as well as large electro-mechanical stress due to the impingement of the fast electrons on to the atoms. We grew the grain size to averaged 25nm by passing a current at density of $0.5x10^6 A/cm^2$ through the specimen by using the heaters for about 5min. Kumar et al. (2011) have reported that by passing current through freestanding thin films, the grain grows because of electromigration stress and Joule heating. The microstructure and selected area diffraction pattern after grain growth are shown in Figure S2.4 (a) and (b). Figure S2.4 (c) shows a typical stress-strain diagram measured in in-situ TEM for Zr thin film with an average grain size of 25nm. The yield stress is around 800 MPa, which is 60% higher than that for as-deposited specimen with an average grain size of 5-10nm. The stress-strain data is almost linear, suggesting that for these larger grains, void swelling (as hypothesized for <10 nm grain size) was mostly absent.

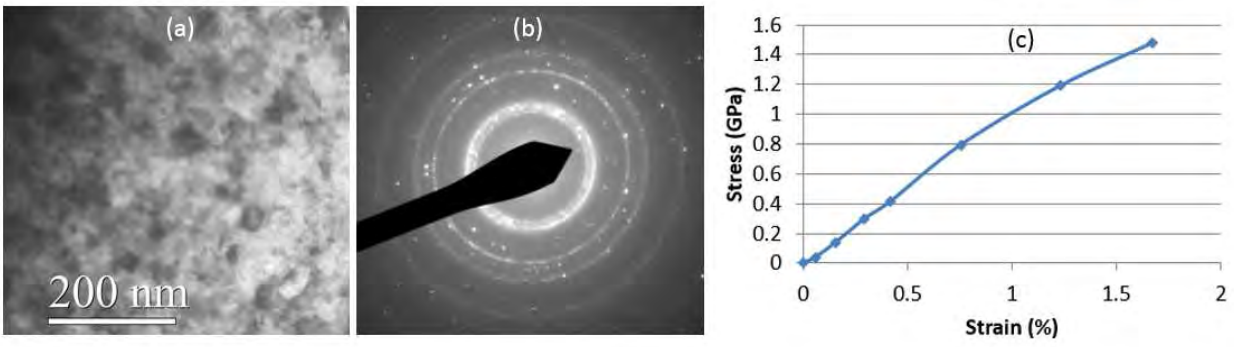

Figure S2.4. (a) bright-field TEM image of specimen after 5min of a current flow at $0.5x10^6 A/cm^2$ density (b) TEM selected area electron diffraction showing grain growth when compared to Figure 1c and (c) stress-strain diagram for 25 nm grain sized specimen, showing absence of the pseudo-plasticity that resulted in form of void swelling.

Continued increase of DC current density can further increase the grain size, as shown in Figure

5. However, this is at the expense of specimen curling. Since the current also raises the temperature by Joule heating, it becomes more flexible. Therefore, the initially flat specimen severely curls and become unsuitable for TEM observation.

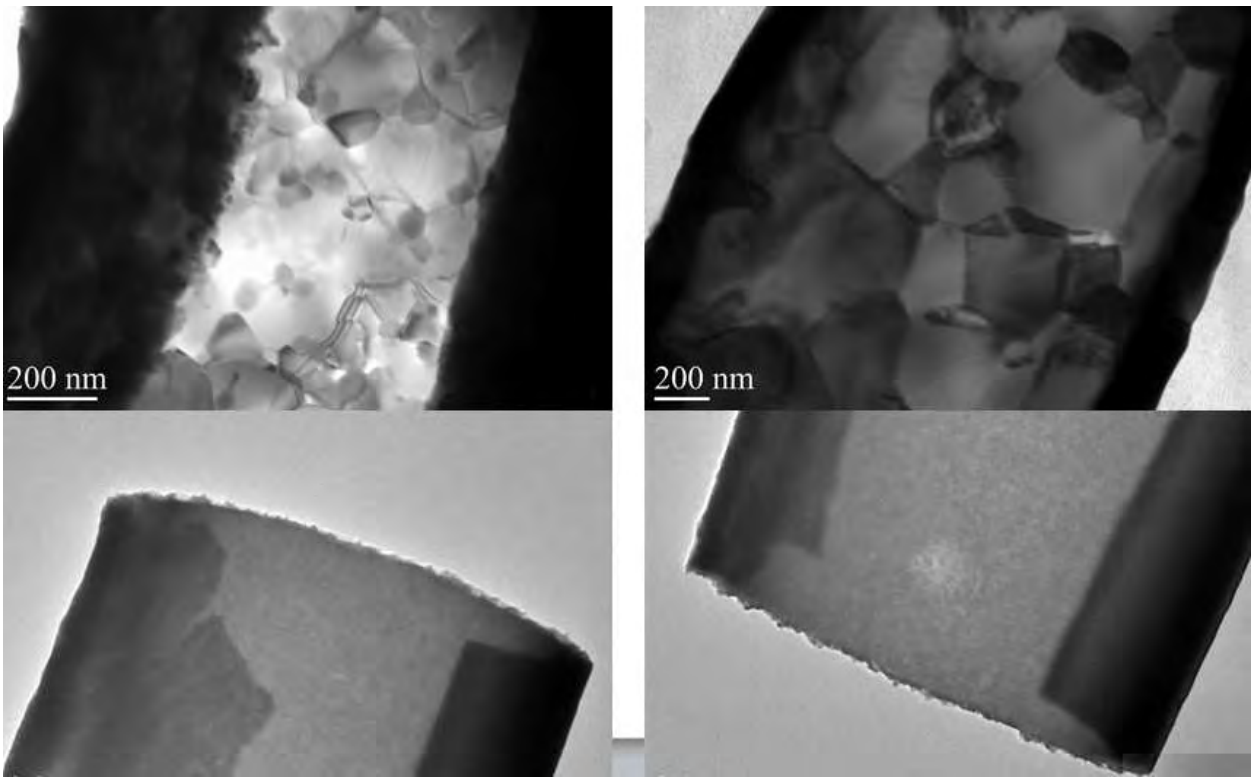

Figure S2.5. Very large grain growth can be achieved in the nc Zr specimens by passing electrical current density in-situ in the TEM. However, the specimen curls excessively, making the observation difficult.

S2.2.3 Thermal Transport Measurement: The MEMS chip described above is also equipped with microheaters that can establish a controllable heat flux and temperature gradient in the specimens (Figure S2.6), which can be measured to quantify thermal conductivity. This an essential step for the proposed research because currently, there is no off the shelf tool for measuring thermal conductivity of such thin films. The underlying physical principle of this experimental design is the Fourier's law of heat conduction. The material under study, Zr in this case, is fabricated as a rectangular shaped fin structure. The knowledge of temperature distribution along and surrounding the sample specimen is required to develop an analytical model for evaluating thermal conductivity of the specimen. The experiment was carried in ambient temperature and the temperature is measured by Infrascope II thermal microscope (Quantum Focus Instruments Corporation) with the spatial and temperature resolutions of about 1.6 microns and 0.1 K, respectively. The solution to a one-dimensional heat conduction problem is well established for different boundary conditions.

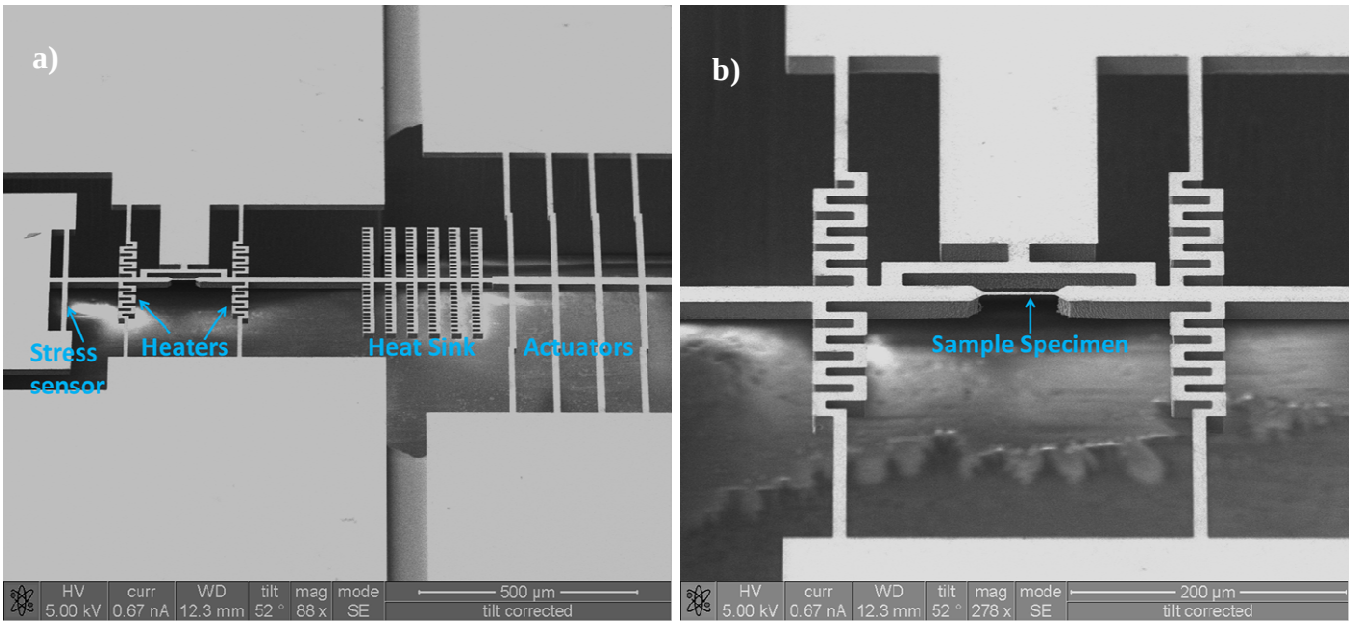

Figure S2.6. a) SEM image of the device showing the specimen integrated with microheaters, b) Magnified image of the freestanding specimen.

The solution for the temperature distribution of a fin with the base temperature, T_b, set to a constant reference value is well established for different boundary conditions at the tip of the fin. Those of interest in this experiment are (i) constant temperature and (ii) adiabatic at x=L, where L is the length of interest in the sample specimen. The respective solutions are

$$\frac{\theta}{\theta_b} = \frac{\frac{\theta_L}{\theta_b}\sinh mx + \sinh m(L-x)}{\sinh mL} \quad (S21)$$

$$\frac{\theta}{\theta_b} = \frac{\cosh m(L-x)}{\sinh mL} \quad (S22)$$

where T_∞ is the room temperature, $\Theta(x) = T(x) - T_\infty$, $\Theta(0) = \Theta_b$, $\Theta(L) = \Theta_L$, $m^2 = \frac{hP}{kA_c}$, h is the heat transfer coefficient, P is the perimeter of the specimen whose cross-sectional area is A_c. h and k are the unknown parameters in the model prediction of temperature. Once the temperature distribution is known from the infrared micrograph, it is matched with the model prediction by parametric variation of thermal conductivity 'k'. The value of k with the best fit of the experimental measurements is obtained as the thermal conductivity of the specimen. In order to evaluate the heat transfer coefficient, the temperature profile in the surrounding boundary layer is measured. An exponential distribution in space is suggested as the best fitting function by Roldan et al. to allow T (air temperature at position y) to approach the room temperature T_∞ as $y \to \infty$, where y is in the lateral direction to the length of sample specimen

$$T = T_\infty + (T_w - T_\infty) * e^{-sy} \quad (S23)$$

Where *s* is a constant determined by plotting the logarithm of the temperature against the distance (y) from the specimen surface at temperature T_w,

$$\ln \frac{T - T_{\infty}}{T_w - T_{\infty}} = s * y \quad \text{(S2.4)}$$

The boundary condition is that the air immediately above the surface is at rest and transfers heat by conduction. The conductive flux Q given by the Fourier's law of conduction is $Q = -k_{air} \frac{dT}{dx}|_{surface}$, where k_{air} is the thermal conductivity of air. The local heat transfer coefficient is defined as $h = \frac{Q}{(T_s - T_{\infty})}$. On substituting the conductive flux at the surface we obtain the expression for the local heat transfer coefficient as,

$$h = k_{air} * s \quad \text{(S2.5)}$$

This work has been done in detail in our previous work and it was shown that the order of magnitude of h is heavily dependent on the size of heater. In this case, for a micro-scale heater, it is expected to lie in the order of 1000 W/m^{2}K. The room temperature thermal conductivity of Zr is known to be around 20 W/m-K. The corresponding heat transfer coefficient is evaluated and is assumed to be same throughout this segment of the experiment. In a typical experiment, DC current is passed through a single set of heaters in order to set a zero-gradient boundary condition at a length L. This is done by snipping the unwanted set of heaters. Figure S2.7 shows the thermal image when 15 mA current is passed through one of the heaters after deactivating the symmetric part using a focused ion beam induced cut. As a result only the connected part of the heater gets lighted up under infrared view.

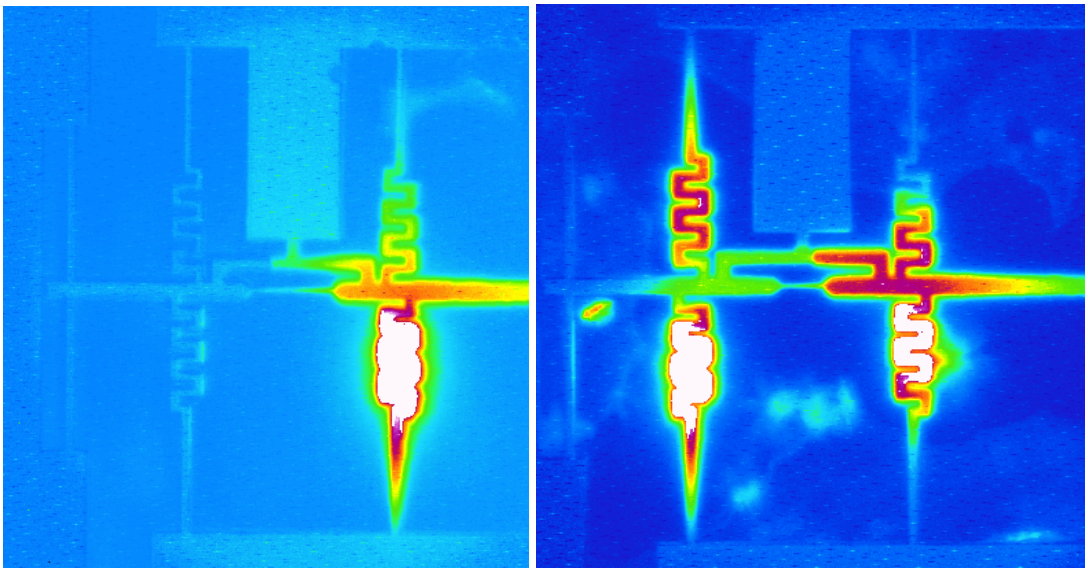

Figure S2.7. Thermal image of the device showing setting up a heat flux and temperature gradient by actuating heaters at (a) one end and (b) both ends (for measuring thermal conductivity as function of temperature).

A linear scan along the sample specimen yields the temperature profile of the film and is shown in Figure S2.8. As evident from the graph, L is taken as the length at which the gradient seems very close to zero. The temperature along the sample is predicted using Equation 2 and the value of 'k' is varied to obtain the best fit. Figure S2.9 shows accuracy of the fit of model prediction to the experimental data.

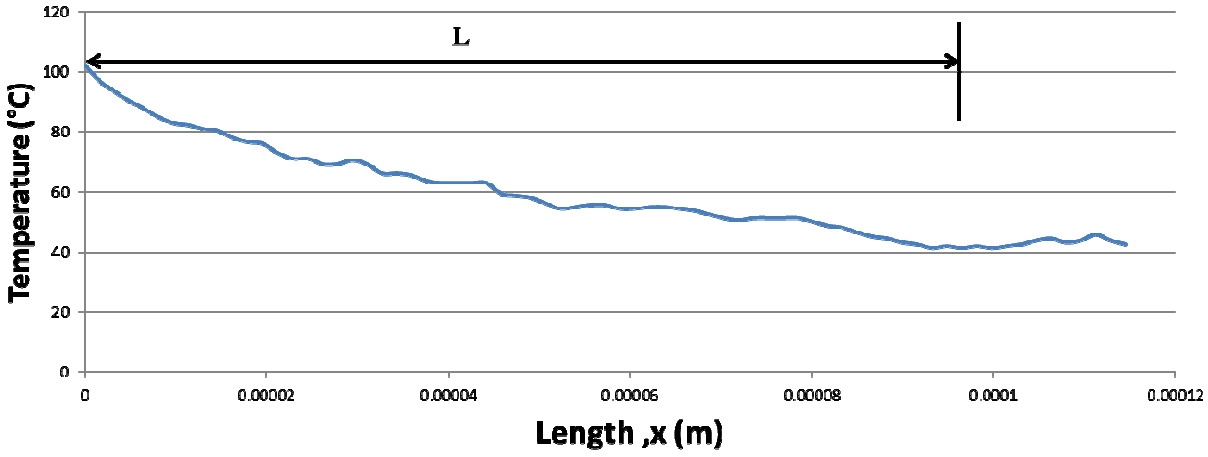

Figure S2.8. Experimental Readings along the sample specimen for 15mA current through heater

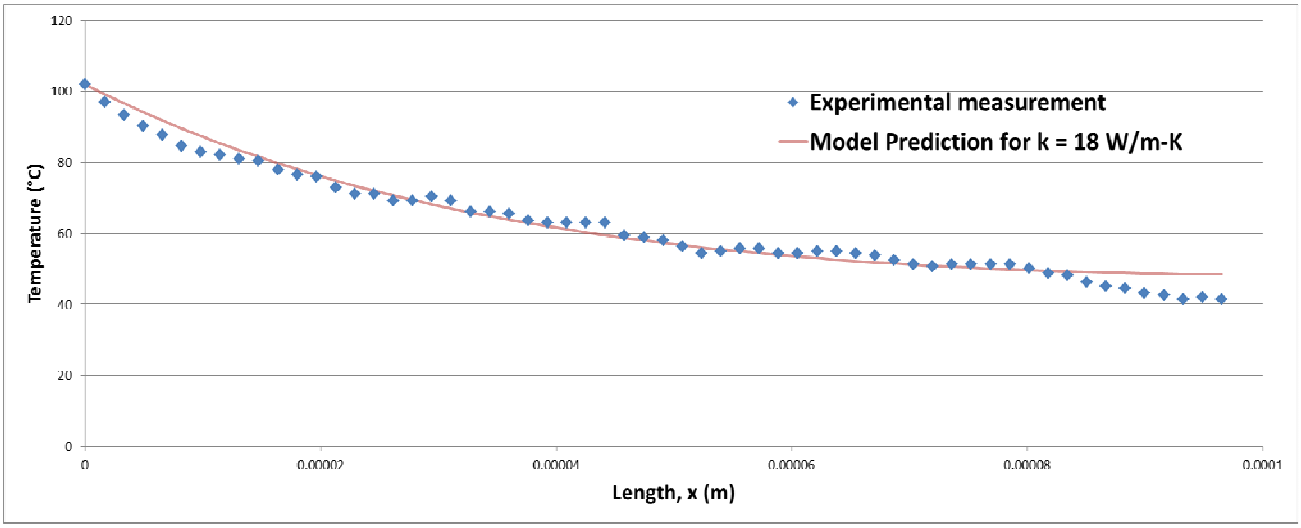

Figure S2.9. Extraction of thermal conductivity by fitting model prediction for k =18 W/m-K

Table S2.1 shows the variation of thermal conductivity of Zr with the average temperature in the as-deposited state. The dramatic (25%) decrease in thermal conductivity is most likely due to the pronounced scattering of the electrons as the grain boundaries as triple points. We hypothesize that such strong thermal-microstructural coupling is due to the <10 nm grain size only.

Table S2.1 Variation with temperature in the as-fabricated specimen

Average Temperature (° C)	Thermal Conductivity (W/m-K)
37.8	20
62.5	18
182.9	15

Since the Zircaloy-4 material is high temperature resistant – mere thermal annealing does not work satisfactorily towards grain growth. Our new technique exploits the high mechanical, thermal and electrical loading that are also localized at the grain boundaries. The average grain size of the as-deposited films was in the 5-10 nm range, whereas most of the studies in the literature are at the micron to 100 nm range. To connect this study to the literature, we aimed to increase the grain size of the specimens. The most common way to achieve this is thermal annealing, which does not result in any appreciable grain growth because zirconium is a high temperature material. We propose that a synergistic effect of various stimuli (thermo-electro-mechanical, or thermo-mechanical) is more influential in grain growth kinetics. To study this effect in zirconium, we passed electrical current through the specimen. Here, the momentum transfer between conducting electrons (electron wind) and diffusing metal atoms creates a flux of metal atoms in the direction of the electron flow, creating both mechanical stress (compressive stresses build up near anode whereas tensile stresses are found near cathode) and temperature fields in the specimen, which trigger the grain boundary diffusion processes. The mechanisms involved in this process are similar to electro-migration, except we applied one order of magnitude lower current density to avoid any damage. The results are shown in Figure 1 for various current levels and polarity. Both the cathode and anode ends of the freestanding specimen are attached to the micromachined silicon structures that act as large heat sinks, hence they are at around room temperature. At the anode end, the electro-migration stress is tensile, while it is compressive at the anode end. Also, the temperature distribution at the specimen is parabolic and is highest (about 350°C). Such combined stress and temperature field effects are reflected by the grain growth in the specimen. The largest grain growth is in the middle section where the temperature is the highest, but still very low compared to the melting point of zirconium (1850°C) and the stress is tensile. The cathode side experiences remarkable grain growth as well, where the temperature is much lower than the middle section but the tensile electro-migration stress is the highest. Finally, very little grain growth is seen at the anode end where the temperature is also very low and the stress is compressive.

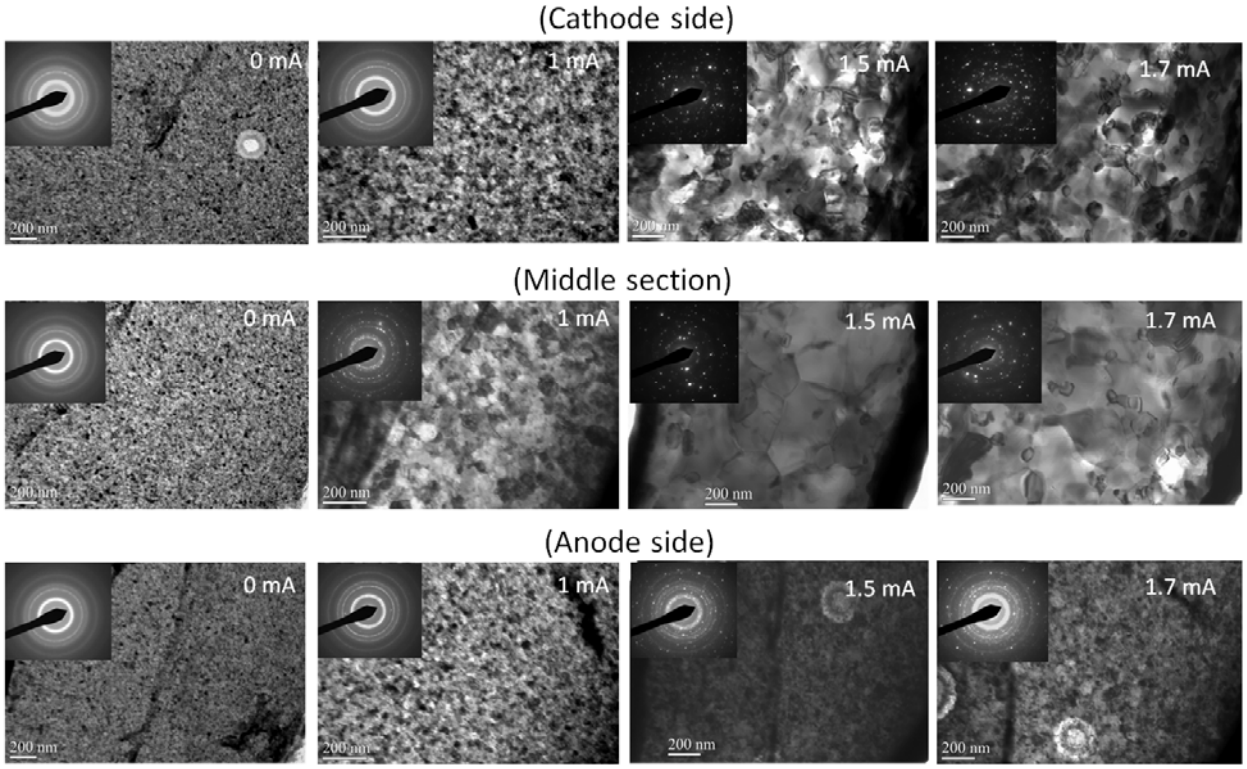

Figure S2.10. Grain growth as function of polarity and magnitude of dc electrical current passed through the freestanding specimen.

The literature suggests that the critical average grain size where the inverse Hall-Petch-type relationship shows for face-centered cubic (FCC) metals (Cu, Ni and Pd) is around 15 nm, which means the yield stress of nanocrystalline FCC metals decreases with grain refinement when the grain size crosses this threshold. Zirconium is known to follow the Hall-Petch relationship, however there is no study in the literature on the inverse phenomenon for HCP nanocrystalline zirconium. We approach this question from an opposite way that is NC metals with a grain size slightly bigger than 15 nm should show higher yield stress than that with a grain size slightly smaller than 15 nm. We grew the grain size to averaged 25 nm by passing a current at density of $0.5x10^6 A/cm^2$ through the specimen by using the heaters for about 5 min. The microstructure and selected area diffraction pattern after grain growth are shown in Figure S2.11(a) and (b). Figure S2.11(c) shows a typical stress-strain diagram measured in in-situ TEM for zirconium thin film with an average grain size of 25 nm. The yield stress is around 800 MPa, which is 60% higher than that for as-deposited specimen with an average grain size of 5-10nm. This suggests inverse Hall-Petch-type relationship nanocrystalline zirconium, however extensive experimentation is needed to substantiate this phenomenon.

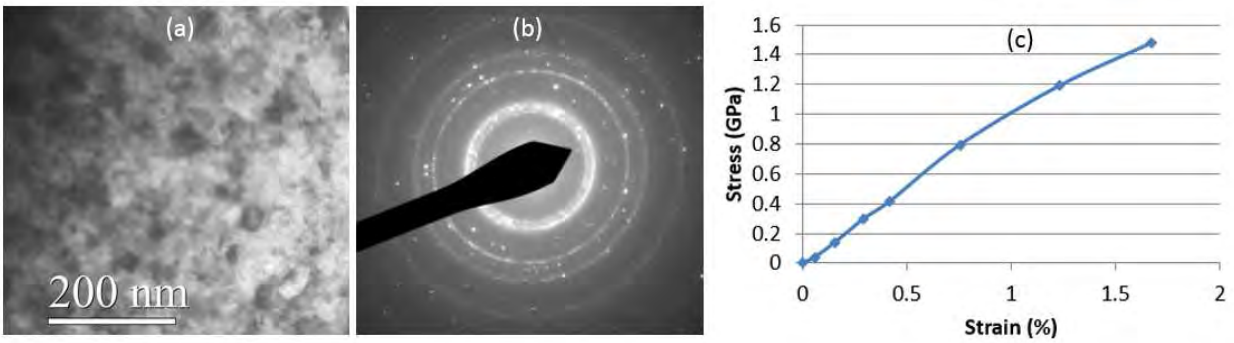

Figure S2.11. **(a) bright-field TEM image of specimen after 5min of a current flow at $0.5x10^6 A/cm^2$ density (b) TEM selected area electron diffraction**

To summarize, we developed a MEMS-based setup for in-situ TEM testing of nanocrystalline zirconium thin films. Mechanical tests were performed both under transmission electron and white light microscopes. The measured Young's modulus of as-deposited specimen with an average grain size 5-10nm is 85-90 GPa which falls very close to the bulk value. However, in-situ TEM tests showed yielding around 400-500 MPa and fracture strain around 1.5-2% strain, whereas white light tests showed mostly linear elastic behavior till fracture at around 900-1100 MPa. In comparison, ultra-fine grained zirconium (>100nm grain size) in the literature shows yield strength of 500 MPa and 15% fracture strain. The measured yield stress of zirconium thin films with an average grain size 25 nm is about 60% higher than that of as deposited specimen with an average gain size of 5-10 nm, which suggests that the critical grain size for nanocrystalline zirconium is at the same range as other metals.

WORK IN YEAR-2:

Figure S2.12 below shows an in-situ TEM testing setup at various temperatures.

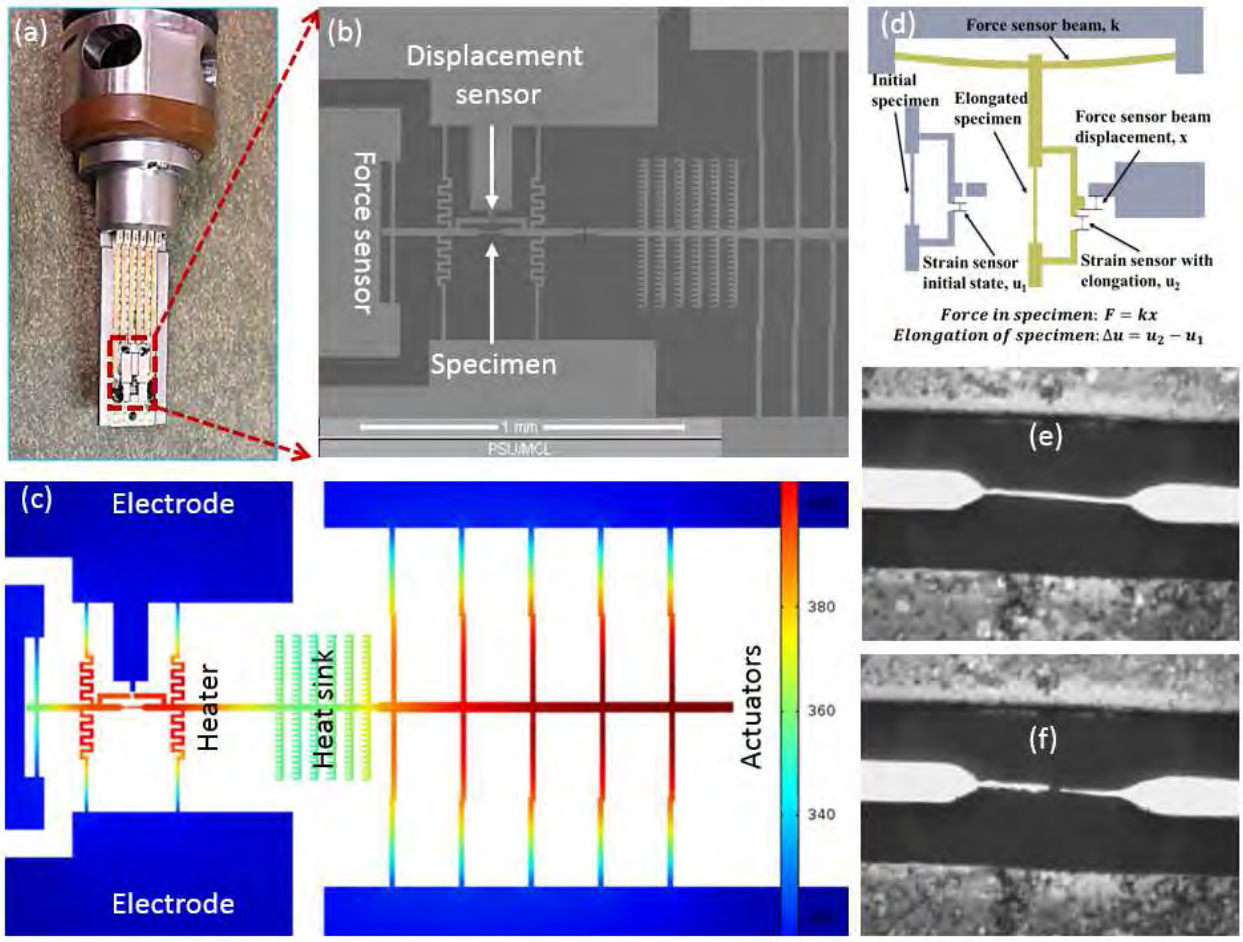

Figure S2.12 (a) TEM test chip holder (b) the test chip with heaters and actuators (c) finite element analysis of operating principle, (d) measurement of stress and strain (e, f) melting of aluminum.

The test chip is fabricated with heaters so that the mechanical deformation mechanisms can be visualized and modeled as function of temperature up to 700 °C. This is demonstrated by melting aluminum (660 °C) as shown in figure 1.

Experimental Results: In-situ TEM tests were performed on evaporated as deposited and Zr+ irradiated specimens (collaboration with Sandia National Laboratories) 100 nm thick, 10 micron wide and 100 micron long. The samples were exposed to Zr+ 800KeV at 4.5nA with doses of 3E10, 3E11 and 3E+12 (collaboration with Sandia National Laboratories). Figure S2.13 shows a typical stress-strain diagram for as deposited specimen. The lack of plastic deformation is due to the small grain size (~10 nm) that is unable to accommodate dislocations. Also the freestanding film has surfaces through which the defects can escape, causing the dislocation starvation. Diffusive plasticity also doesn't take place at room temperature because Zr is a very high melting point material.

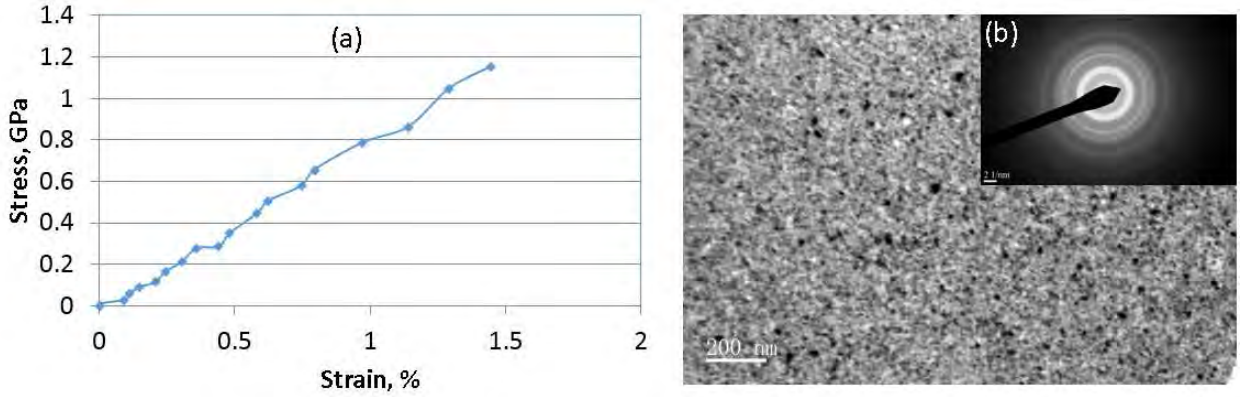

Figure S2.13. In-situ TEM mechanical test results without irradiation (a) Stress strain diagram and (b) as received microstructure

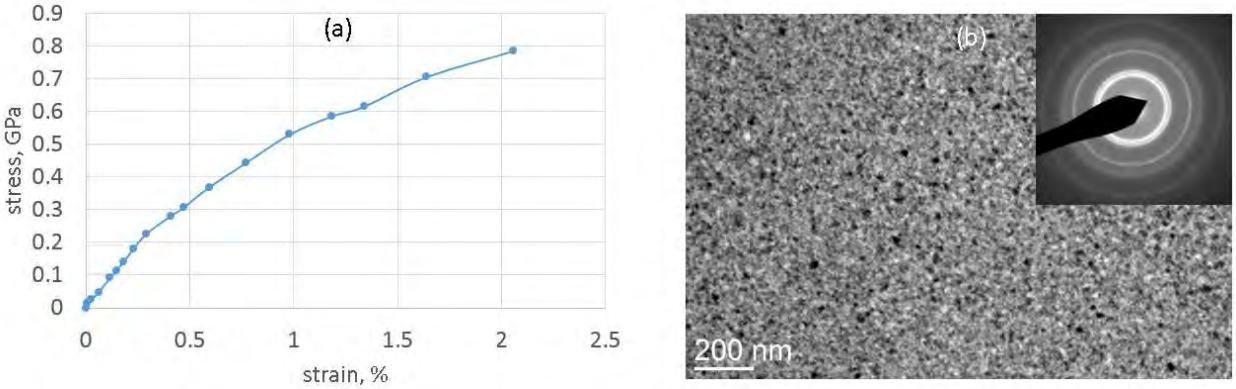

Figure S2.14. In-situ TEM mechanical test results with irradiation (a) Stress strain diagram and (b) irradiated with 800 KeV Zr+ with dose of 3E10.

Figure S2.14 shows the in-situ TEM experimental results for irradiation dose of 3E+10. The TEM images did not show any discernible change, which suggests that the effects of irradiation may have been atomic level vacancy. This is reflected in the Young's modulus, which is about 55 GPa. The defects added from irradiation introduces some extent of plasticity in the materials as seen in the stress strain diagram. Figure S2.15 below experimental result for irradiation dose of 3E+11. The Young's modulus is about 60 GPa, suggesting no further decrease. The TEM images show discernible coarsening effects. Also, the increase in strain hardening is obvious with the increase in ultimate stress.

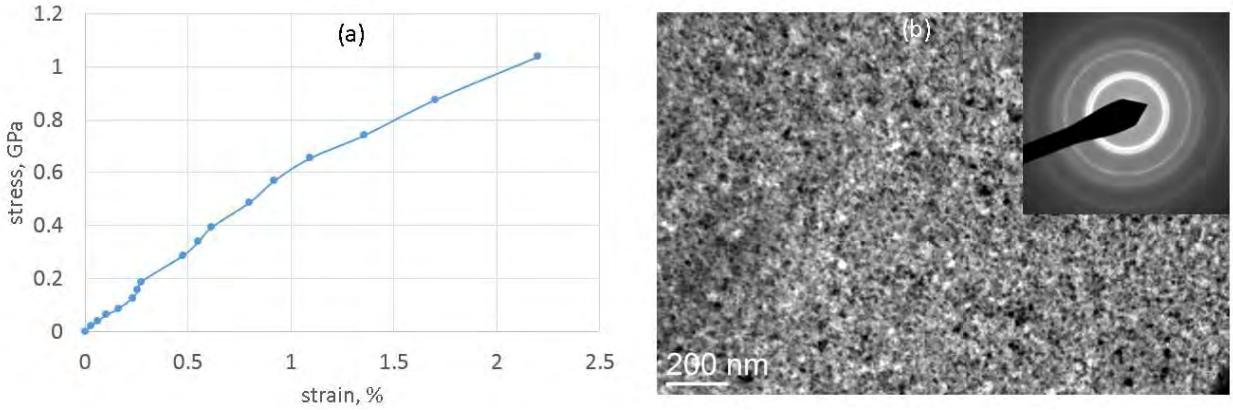

Figure S2.15. In-situ TEM mechanical test results with irradiation (a) Stress strain diagram and (b) irradiated with 800 KeV Zr+ with dose of 3E11.

Figure S2.16 below experimental result for irradiation dose of 3E+12. The Youngs modulus is about 65 GPa, suggesting no further decrease. Remarkable strengthening effect and improvement in fracture strain is observed. We are currently analyzing the experimental results so that fracture toughness measurements can be carried out in the future.

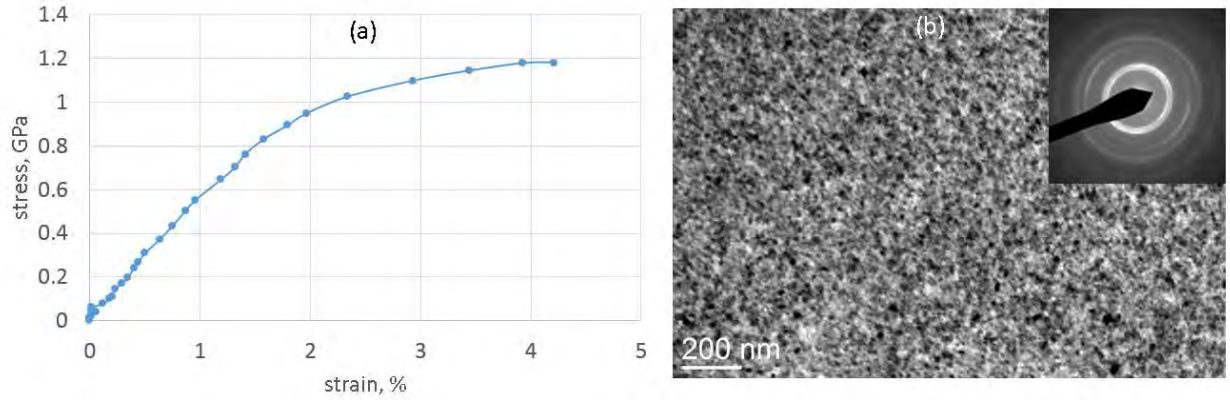

Figure S2.16. In-situ TEM mechanical test results with irradiation (a) Stress strain diagram and (b) irradiated with 800 KeV Zr+ with dose of 3E12.

<u>Activity 1:</u> Adapting bulk zircaloy specimens on MEMS devices was a major activity in this time period. As reported previously, the MEMS devices need about 20 microns long specimens that are highly planar. Since the FIB cut specimens tend to curl slightly, integrating them on to the silicon micromachined MEMS devices becomes challenging.

We have taken an alternative route where the bulk specimen is polished to about 10 micron thickness and the laser cut into thin strips. These strips are then manipulated and secured to the MEMS device using vacuum compatible and high temperature glue using a nanopipette. We then used FIB milling process. The specimen thins down below 200 nm, it starts curling, but remains secure. Currently, we are improving this technique. Figure S2.17 shows the achieved results.

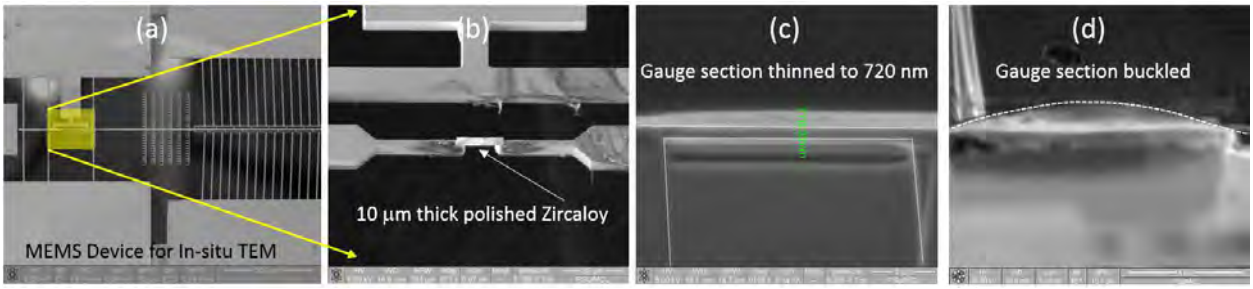

Figure S2.17. (a) location of specimen in a highly planar MEMS device (b) a polished cut out of specimen mounted on the gauge section (c) FIB thinning to 720 nm and (d) continued thinning to 200 nm

Collaborating with University of Dayton, we were able to sputter deposit Zircaloy thin films on the MEMS devices, which shows excellent promise for the proposed research. Figures S2.18a and S2.18b show the TEM brightfield and diffraction images. The thickness was calibrated using a high resolution SEM. Figures S2.18d, S2.18e and S2.18f show the segments of an XPS scan of the film with the constituents.

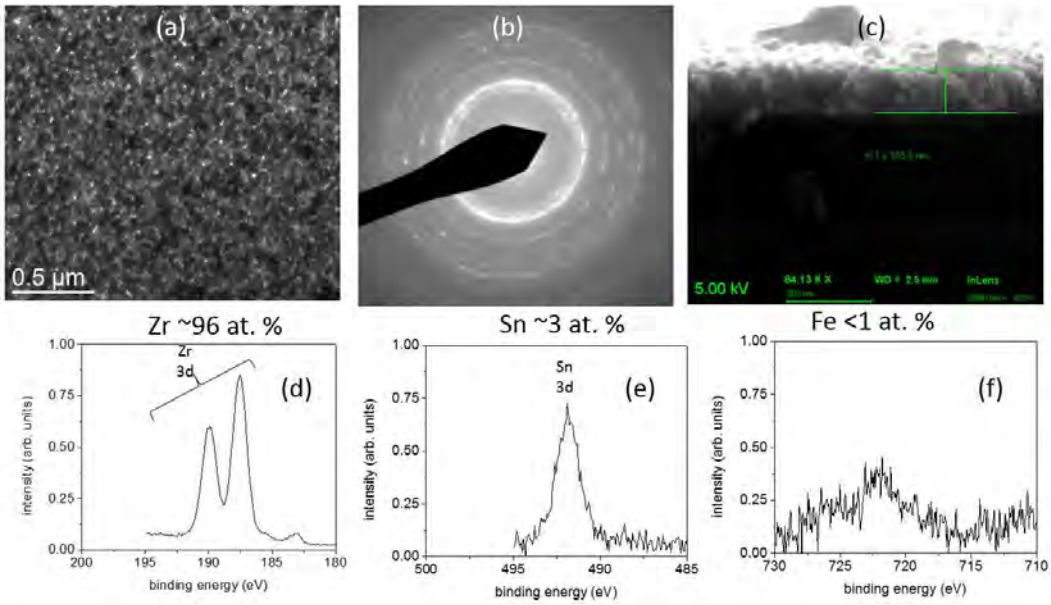

Figure S2.18. Pulsed laser deposition of Zircaloy thin films from a bulk zircaloy target allowing characterization of nanocrystalline regime (a) TEM bright field (b) diffraction pattern (c) SEM cross-sectional image showing thickness (d, e, f) XPS scans showing the film stoichiometry.

<u>Activity 2</u>: Control of microstructure of the specimens was performed in-situ in TEM. Our previous finding was that up to 100 times grain size increase by thermo-electro-mechanical annealing was possible. In this period, we worked on the zircaloy thin films. For zircaloy, remarkable grain growth due to heating is about shown inside the TEM. Here the grain size increased about 10 times after heating to 150 ºC. The extent of such grain growth is very obvious in the diffraction patterns. The grains also showed extensive dislocations inside. The results suggest that nanocrystalline zircaloy has

higher grain boundary mobility, which gives rise to the high temperature sensitivity.

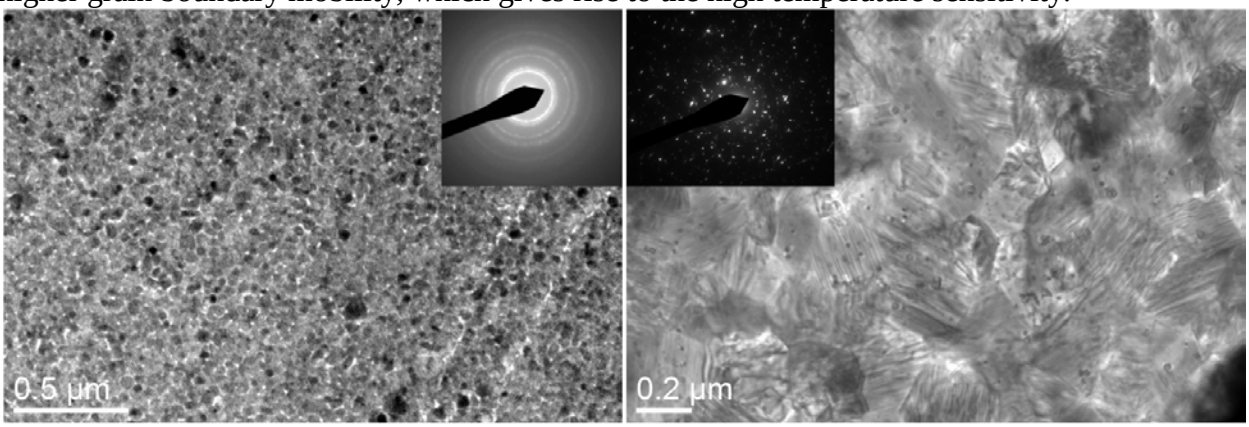

Figure S2.19. **(a) Nanocrystalline zircaloy at room temperature (b) at about 150 C**

Activity 3: Ion-irradiation effects on nanocrystalline Zr. In the period, we measured mechanical and thermal properties of zirconium thin films as function of ion irradiation. The reason for this activity was that 100 nm thin films remained radiation transparent, and only ion irradiation could do any damage to the specimens. The results for radiation fluence of 10^{12} ions/cm^2 were presented in the previous reporting period. Here we present further irradiation results up to $3.2x10^{14}$ ions/cm^2 and present some analysis. Results show that Young's modulus drops with increasing doses, specifically more than 50% with ion irradiation dose of $3.2x10^{14}$ ions/cm^2. The fracture strain increases from 1.5% to 2.6% at 0 and 3E14 ions/cm^2, respectively. Thermal conductivity decreases from 20 W/mK at 0 to 13.6 W/mK at $3.2x10^{14}$ ions/cm^2. TEM observation reveals that fringes in the microstructures increase with irradiation doses. These changes in the thermal and mechanical properties are associated with nanoscale displacement damage created by the self-ion irradiation.

Ion Irradiation Effects on Mechanical Properties: In collaboration with Sandia National Laboratory, we irradiated partially processed MEMS devices with an 800 keV Zr^+ beam using the 6 MV HVE Tandem accelerator. The ion energy was chosen based on a SRIM simulations to have the majority of the ion species past through the Zr film leaving a relatively uniform damage profile, as a function of depth in the Zr. The majority of the Zr ion species are predicted to come to rest in the silicon sacrificial layer that was removed by reactive ion etching. All of the irradiations occurred at nominally room temperature with a rastered ion beam. Figure S2.20 shows the ion damage profile calculated with SRIM software.

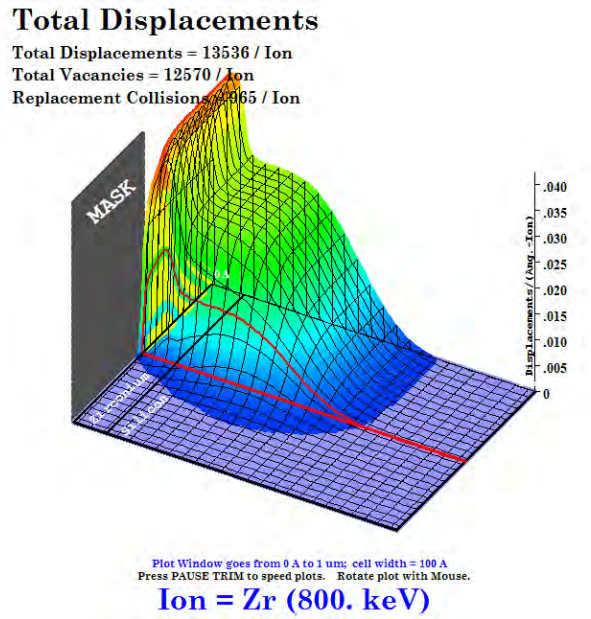

Figure S2.20. **SRIM simulation of the ion damage profiles in the Zr specimen and the sacrificial silicon layer**

Figure S2.21 summarizes the effects of ion irradiation on the mechanical properties of nanocrystalline Zr. The stress strain diagram inset shows elastic behavior for the as deposited specimens. This is because for grain sizes below, it is difficult for dislocation based plasticity to dominate. Also motion of dislocations may result in the their escape through the surface. Such mechanical annealing is known to cause 'dislocation starvation' for nanocrystalline metals. Our results confirm this phenomenon and also shows that the material can regain plasticity if external sources are active. This is possible by irradiating the specimens. We propose that the effect of ion radiation is to increase the grain size as well as induce linear and rotational displacements in the specimen. The underlying mechanism could be ion impact effects on the abundant grain boundaries and make them mobile.

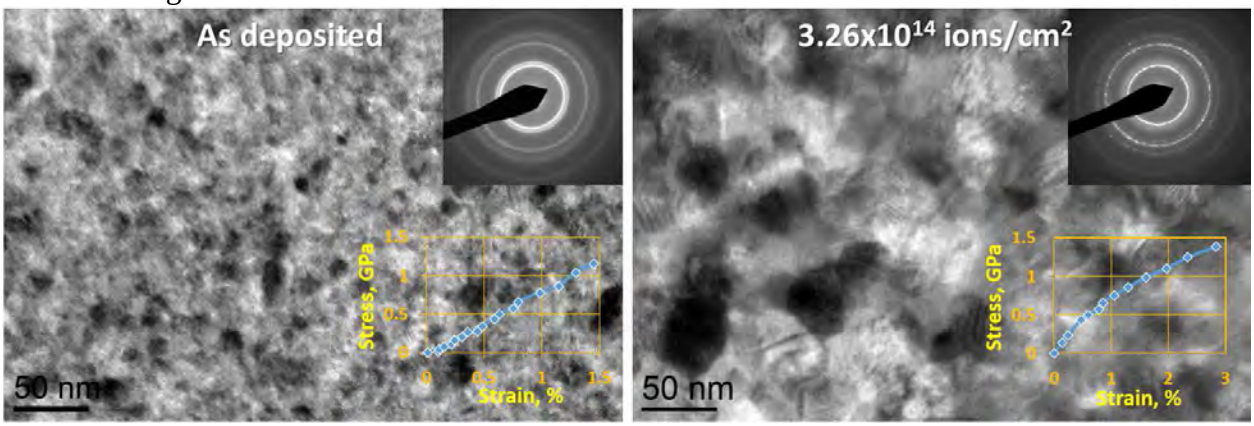

Figure S2.21. **Ion irradiation effects on nanocrystalline Zr. Inset shows stress-strain diagrams (a) before and (b) after irradiation.**

Figure S2.22 shows three snapshots for some of the irradiated specimens during the insitu TEM

testing. The grains are too small to show visual distinctions, however, the radiation damage is very clear when compared by the unloaded specimens. This analysis suggests that mechanical stress induced microstructural changes are insignificant compared to the radiation damages.

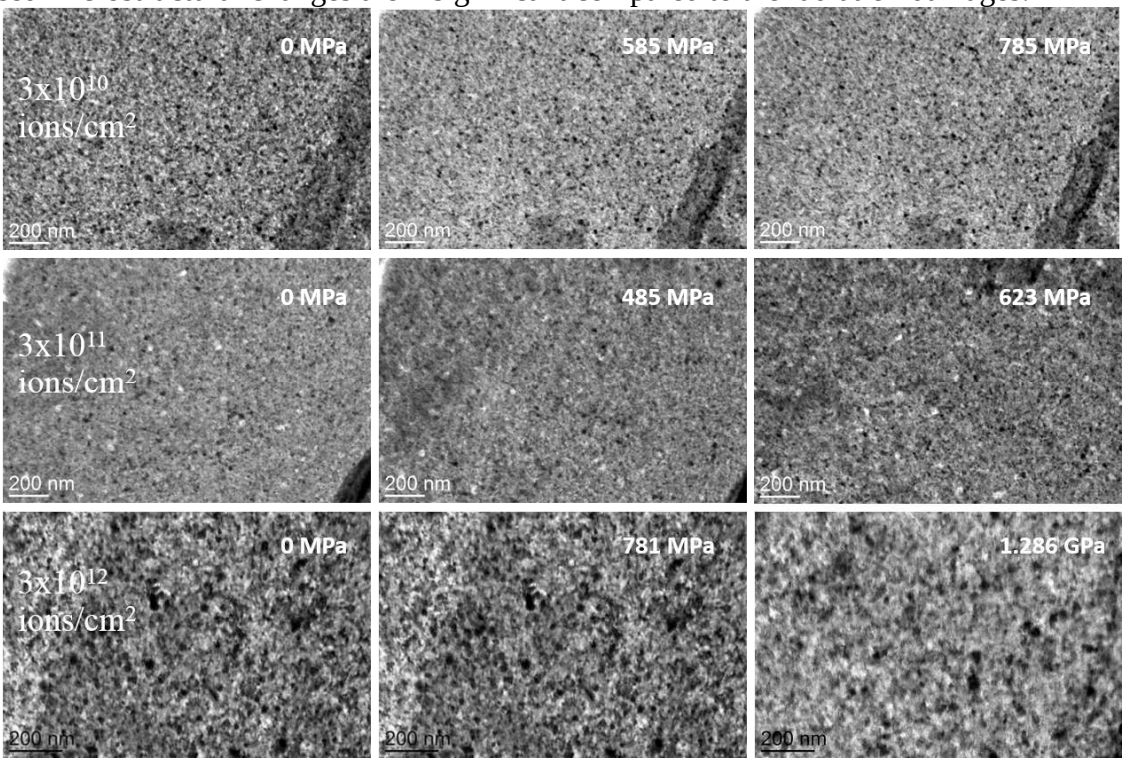

Figure S2.22. **In-situ TEM test results for three different radiation doses**.

Figure S2.23 below shows the texture changes due to irradiation. The 101 plane is very diffused after irradiation, while a new ring showing the 220 plane for ZrO2 shows up. The diffraction patterns also show the grain size increase.

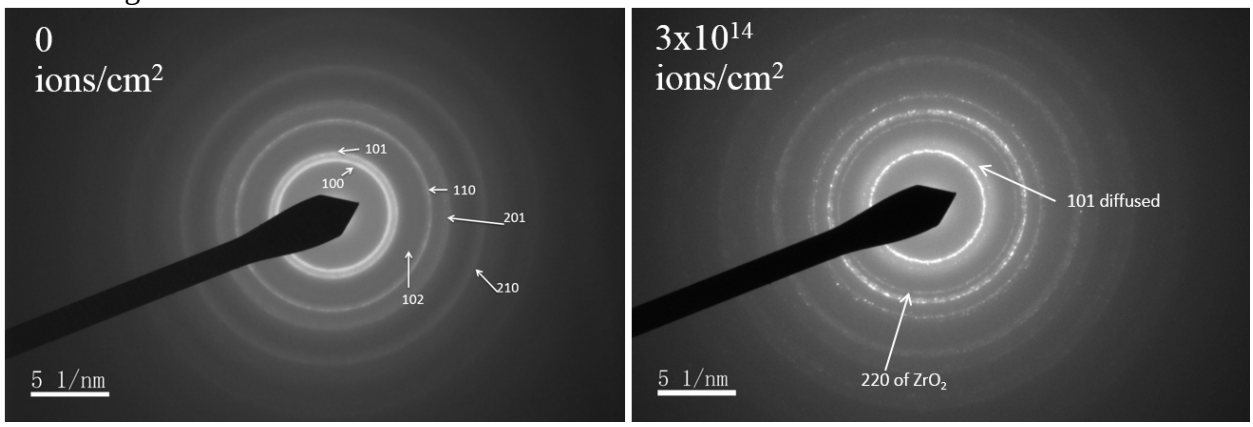

Figure S2.23. **Diffraction patterns indicating texture and grain size changes as function of irradiation.**

Ion Irradiation Effects on Thermal Properties: We have measured thermal properties of the ion

irradiated Zr specimens. Thermal conductivity measurements were conducted under infrared (IR) microscope. Figure S2.24a shows a typical thermal mapping from the IR microscope after heating the sample with a MEMS device. The freestanding specimen is modeled as a simple extended fin as shown in Figure S2.24b. Energy balance is applied on a control volume of the specimen with a length of Δx.

$$kA\frac{dT}{dx}\Big|_x - kA\frac{dT}{dx}\Big|_{x+\Delta x} = hP\Delta x(T - T_\infty) \quad \text{(S2.5)}$$

where *k* is thermal conductivity of specimen, *A* and *P* are cross-sectional area and perimeter, h is the overall heat transfer coefficient (summation of convection h_c and radiation h_r) and T_∞ is the ambient temperature. The solution to this problem is used to curve fit the experimental data with the model prediction to extract the thermal conductivity □. The heat transfer coefficient h can be acquired by applying energy conservation principle near the heated specimen surface,

$$-k_{air}A\frac{\partial}{\partial y}(T - T_s)\Big|_{y=0} = h_c A(T_s - T_\infty) \quad \text{(S2.6)}$$

where, y is the perpendicular direction to the specimen length (y = 0 denotes specimen surface) and T_s is the specimen temperature. The solution to this equation can be rearranged as,

$$\ln\frac{(T-T_\infty)}{(T_s-T_\infty)} = -sy \text{ , where } s = \frac{h_c}{k_{air}}. \quad \text{(S2.7)}$$

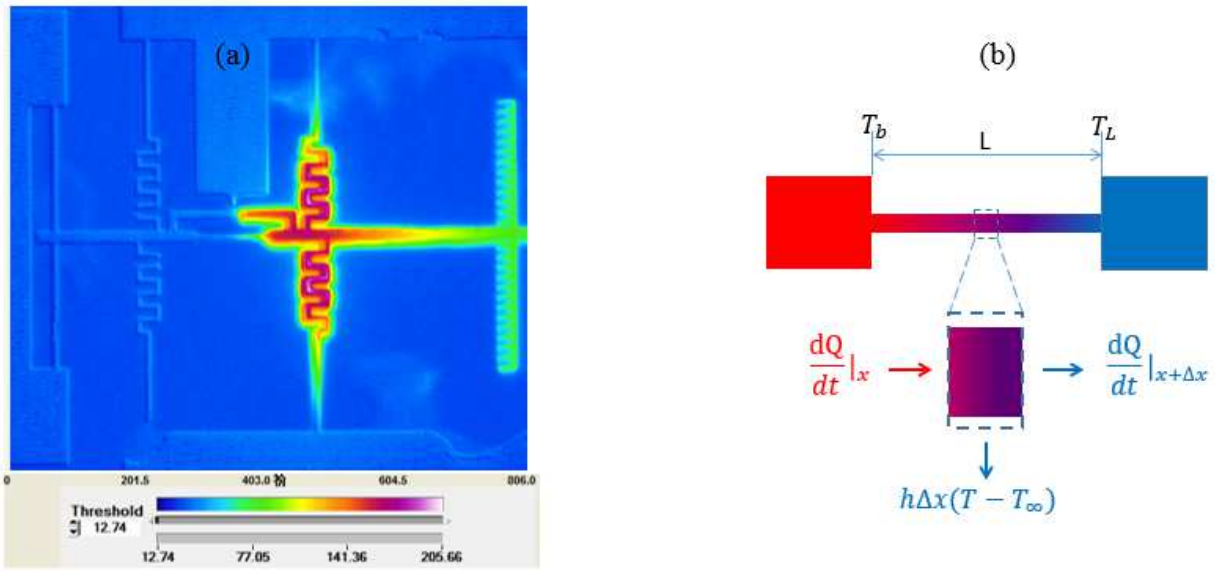

Figure S2.24. (a) Infrared thermal image of the device when one-side heater is activated; (b) Mathematical model of proposed study.

We measure thermal conductivity for Zr specimens as function of applied strain. Figure S2.25 summarizes the obtained results with a strain range from zero to 1.244%, where the thermal conductivity clearly decreases as we increase the strain. This behavior can be ascribed to the nanocrystalline microstructure of these thin films. When the geometric dimension of specimen or the grain sizes go down to nanoscale, it becomes increasingly difficult for the grain interiors to accommodate the external deformations. Therefore, mechanical deformation mechanisms for grain sizes smaller than phonon mean free path (about 20 nm) are basically different from the bulk ones

which is not only due to absence of dislocations but also very high volume fraction of the grain boundaries. In absence of dislocations in the grain interior, the grain boundaries primarily accommodate the applied strain. To accomplish this, the grain boundaries must slide, rotate or emit dislocations that also move along the grain boundaries as strain is applied. The scattering of electrons by grain boundaries will be enhanced by these grain motions. Therefore we hypothesize that the motion of grain boundaries resulted from strain localization is the primary mechanism behind thermal-strain coupling.

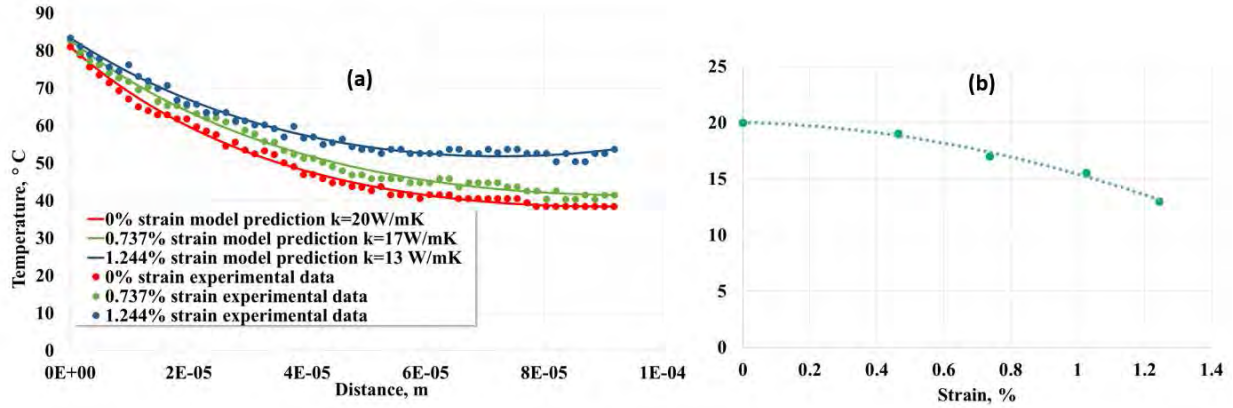

Figure S2.25. Thermo-mechanical coupling at the nanoscale. Experimental results (a) Comparison of experimental temperature profile with model prediction at various strains; (b) Plot of measured thermal conductivity as a function of strains.

Finally, we measured the thermal conductivity of the as function of irradiation. The results are shown in Figure S2.26, where about 38% reduction of thermal conductivity is seen at 3.26×10^{14} ions/cm^2 radiation. We hypothesize that the effect of irradiation is most prominent at the grain boundaries, which are easier to knocked out by the ions. Pronounced disorder at the grain boundaries lead to the reduction in thermal transport

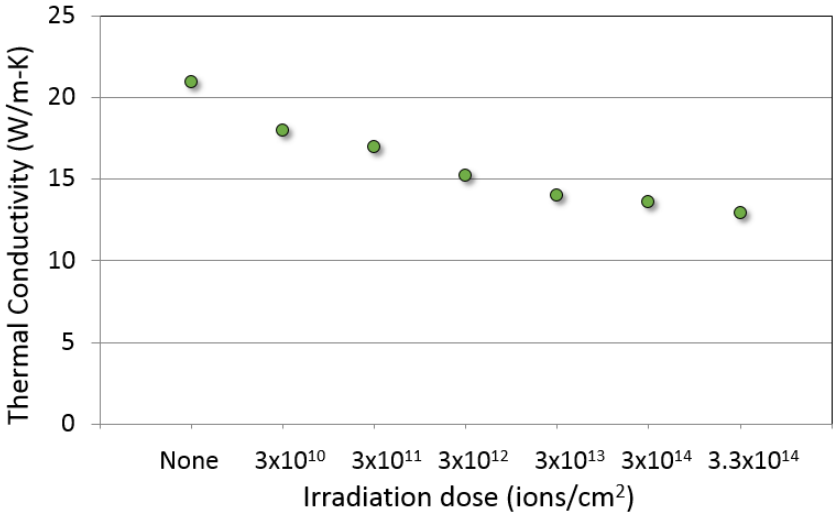

Figure S2.26. Thermal conductivity of nanocrystalline Zr as function of ion irradiation.

Activity 4: Gamma Irradiated Bulk Zircaloy Study

A major obstacle for the proposed research was integration of electron transparent zircaloy specimen (sectioned from the bulk) with the MEMS devices for in-situ TEM testing. The issue was the planarity of the specimen (irrespective of FIB sectioned or electropolished or ion milled). Since the MEMS devices are highly planar, any warpage in the specimen makes it challenging to fix both ends of the specimen on the two planar jaws of the MEMS. In this quarter, we have resolved this issue and have demonstrated it on gamma irradiated zircaloy specimens.

Zircaloy 4 specimens were irradiated at The Penn State Breazeale Reactor (dry cell ^{60}Co irradiator) with gamma rays with > 200 Mega Rads. The new specimen preparation technique involves ultra-microtomy. First, we use a diamond wire saw to cut the specimen to a thickness of 20 micron foils. The foil is then embedded in a polymer at low temperatures. This composite material is then sliced to 100-200 nm thickness using a 45° diamond knife. The slices are collected on a TEM grid and subjected under a nanomanipulation tool. This tool is equipped with vacuum to grip the slices and dual X-Y-□ actuators to precisely orient the specimen. We use a thin layer of water to initiate the bonding between the slice and the MEMS device. Once positioned, we transfer the device to the FIB chamber and secure the two ends of the specimen. Figure S2.27 shows the setup for specimen preparation.

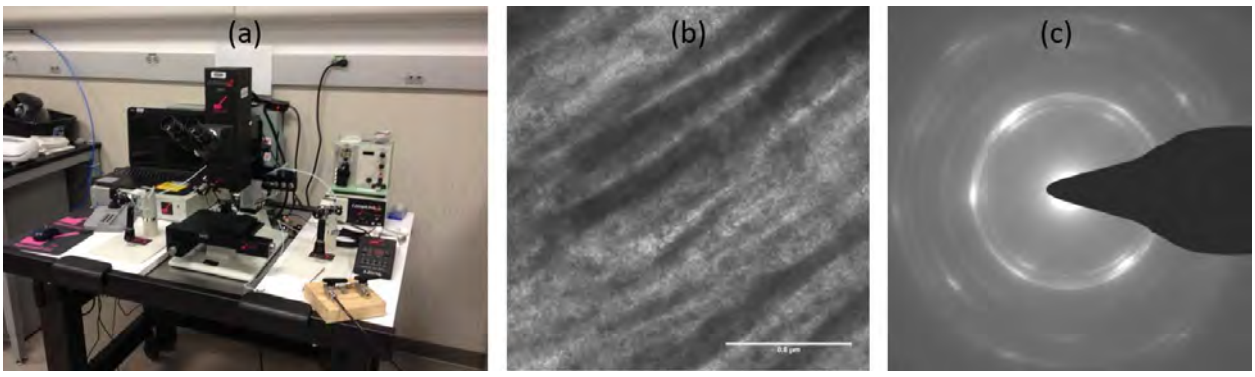

Figure S2.27. **Setup for integrating bulk irradiated samples on MEMS device for in-situ TEM testing.**

Microstructural Control on Gamma Irradiated Specimens: The gamma irradiated specimens showed remarkable loss in crystallinity, which negatively impacts the mechanical and thermal properties. These effects are well documented in the literature. However, not a single study exists on healing such microstructural damages. This is because the conventional process of annealing requires very high temperature. We therefore observe that a significant contribution opportunity exists in novel processes for microstructural healing. This motivates us to set up the key objectives to minimize defects, residual stress and amorphized grain structures.

We first point out that one needs very high atomic mobility to achieve these objectives. In addition to thermal stimulus, the literature contains evidence of electrical or mechanical annealing [89, 90]. These processes are typically not viewed as favorable because of the possibility of adverse effects. We propose that significantly higher mobility can be achieved at lower temperatures if accompanied by electrical current and mechanical stress. Our hypothesis

starts with very small current density (30% of the electromigration failure limit). Electrical current is a very effective stimulus to generate and flow vacancies. This is due to the electron wind force arising from the momentum transfer between conduction electrons and metal ions. Inside the grains, the uniform lattice structure means there is hardly any momentum transfer. The opposite is true at the grain boundaries, where most of the vacancy generation and motion takes place Wu and Ho (2012). Dashed blue and red arrows in Figure S2.28a schematically show this.

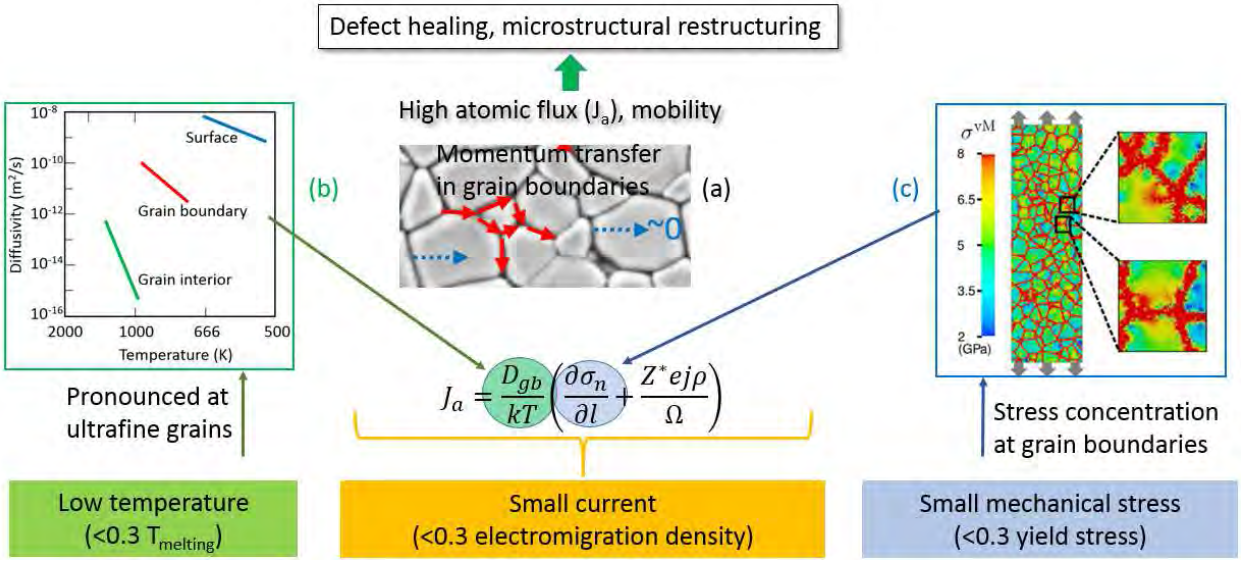

Figure S2.28. **Hypothesis proposed for microstructural healing.**

The synergy of temperature, current and stress fields is obvious from the four driving forces in the atomic flux balance equation Lin and Basaran (2005). These are (1) atomic or vacancy concentration gradients, (2) the electron wind force, (3) temperature gradients, and (4) mechanical stress gradients. Equation 1 shows these contributions to the total atomic flux, J De Orio et al. (2010).

$$J_1 = -D\nabla N;\quad J_2 = \frac{NeZ^*D\rho}{kT}j;\quad J_3 = -\frac{NDQ\rho}{kT^2}\nabla T;\quad J_4 = \frac{ND\Omega}{kT}\nabla\sigma \qquad \text{(S2.8)}$$

Where, D is diffusivity, k is Boltzmann's constant, T is absolute temperature, N is vacancy concentration, Z* is effective charge number, e is the elementary charge, j is current density, Q is the heat of transport, f is the vacancy relaxation factor, Ω is the atomic volume, and σ is the hydrostatic stress. Along the grain boundary, where the diffusion is fastest, we can re-write Tan et al. (2011),

$$J_a = \frac{D_{gb}}{kT}\left(\frac{\partial\sigma_n}{\partial l} + \frac{Z^*ej\rho}{\Omega}\right) \qquad \text{(S2.9)}$$

<u>Synergy with temperature:</u> Since self-diffusion is an Arrhenius type function of temperature Hoffman and Turnbull (1951); externally applied temperature will exponentially promote the

atomic flux. This is shown in Figure S2.28b, which also shows that grain boundaries have orders of magnitude higher diffusivity compared to grain interior. The implication for ultrafine grains is thus *even more pronounced atomic mobility*.

Synergy with stress: Mechanical stress field also has a synergistic effect on the electrical annealing process. According to Equations 1 and 2, the vacancy flux decreases as soon as internal stresses build up in the metal due to vacancy transport from cathode end to anode end. The role of an external mechanical field is to counter the effects of the internal stress and the net effect will be higher vacancy flux and mobility Kirchheim (1992). This effect is very pronounced for ultrafine grains, where stresses are highly localized at the boundaries, whereas the grain interior stresses are smaller and more uniform. Figure S2.28c shows that the local value of the stresses can be very high to influence the electrical current induced atomic mobility. This is why the simultaneous effect of the current, temperature and stress is more pronounced than the individual stimuli. Our preliminary results also support that the synergy is more pronounced Alam et al. (2014; Wang et al. (2014) than the individual stimuli. It is important to note that the electrical annealing process is orders of magnitude faster than thermal annealing because of the very high atom drift velocity,

$$V_a = \left(\frac{D}{kT}\right)|e|Z^* j\rho \qquad \text{(S2.10)}$$

In comparison, thermal annealing generates order of magnitude smaller vacancy concentration and thermal drift speed is negligible compared to electrical drift speed Asoka-Kumar et al. (1996). Figure S2.29 shows the successive phases of microstructural healing in irradiated specimen

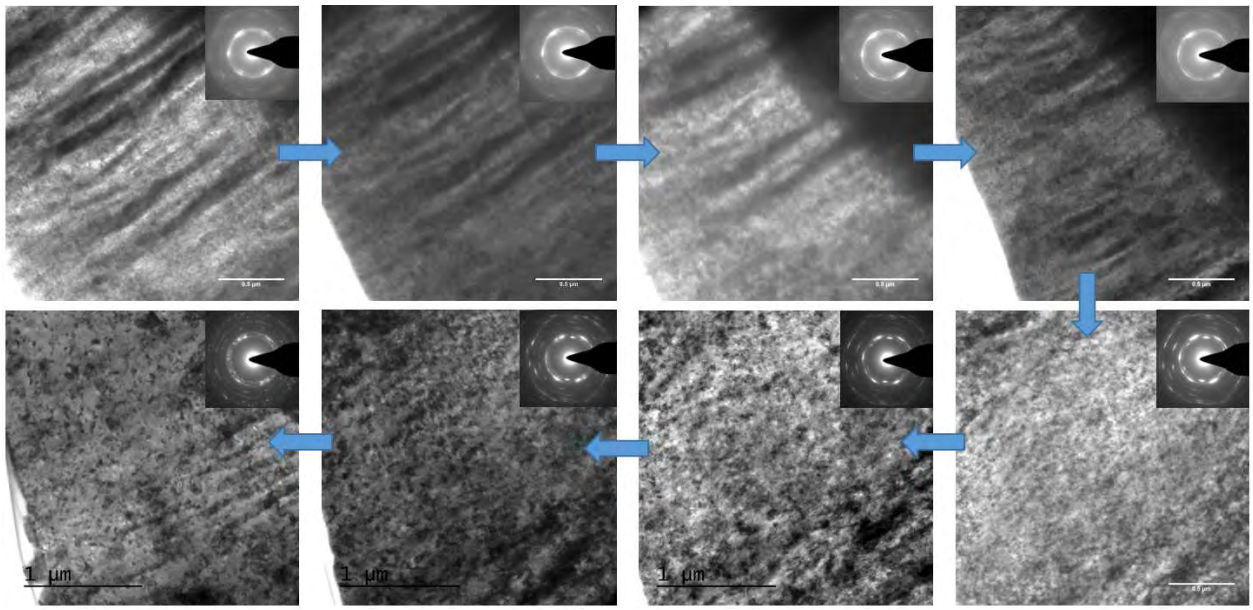

Figure S2.29. **Successive stages in microstructural control using thermo-electro-mechanical annealing**.

Neutron Irradiation of Zircaloy: While the co-PI (Haque) is working on Gamma irradiated samples, he is irradiating the Zircaloy specimens at the The Penn State Breazeale Reactor. These specimens will be secured by the radiation safety office till end of October to be deemed safe to handling. It is expected that the next quarter will involve these neutron irradiated specimens.

WORK IN YEAR-3:

In year 3, our project focuses on the Tasks 5 (In-situ TEM measurements of thermal conductivity as function of irradiation and mechanical stressing) and 7 (Identification of key microstructural parameters that link irradiation induced damage and environment dependent thermomechanical coupling based on quantified data).

In this quarter, in-situ TEM experiments were deferred to the next one because of instrument unavailability. The JEOL 2010 TEM was decommissioned by Penn State. A new FEI Tecnai has been added. The co-PI (Haque) has accordingly ordered a new TEM holder that is capable of running the in-situ experiments on MEMS platforms. The holder arrived only in January 2016 after being ordered in September 2015. Currently, we evaluating the holder for its functionality.

In addition, we are waiting for the Isotope Committee at Penn State to release the neutron irradiate zircaloy specimens to us for experimentation. The specimens are still very hot to be released.

Due to the unavailability of the TEM, our activities in the first quarter of the third year was limited in gamma irradiated specimen preparation. These specimens will be tested for Tasks 5 and 7 as soon as the TEM holder is onlone.

We also have setup up ex-situ experiments under the infrared microscope so that Task 5 can be completed on time. The results of these experiments are currently being analyzed.

January to April 2016 Activities:

Neutron Irradiated Bulk Specimens: Penn State University's Isotope Committee has released the bulk zircaloy specimens irradiated in the Breazeale Nuclear Reactor for 10 MW-hr. More samples have been irradiated with 100 MW-hr, which will be studied upon release by the committee. TEM specimen preparation from the bulk coupons have started with the gamma irradiated (> 200 M rads) zircaloy. In the previous quarter we developed a nanoskiving based technique to achieve this. However, the concern of the microstructure amorphization due to the extreme shear stresses due to skiving was visited in this quarter.

In the new process, we start with thin sectioning the bulk specimen to 25 microns using a diamond wire saw. This specimen is then polished to 5 microns thickness. Next we chemically polished the film with (0.25% HNO_3 and 0.25% HF (49%) solution which further reduced the specimen to <300 nm. We also experimented with electropolishing, where the electrolyte is 40 ml. $HClO_4$ (70%) : 160 ml. C_2H_5OH with Platinum (Pt) cathodes. The voltage and current values were around 20-22V and 0.6 A respectively and temperature < 25C. The etching is very aggressive and is very nonuniform We

therefore discontinued the electropolishing and adopted the chemo-mechanical polishing. The specimen is then mounted on a MEMS device and investigated in a TEM. Figure S2.30 shows the results from this activity.

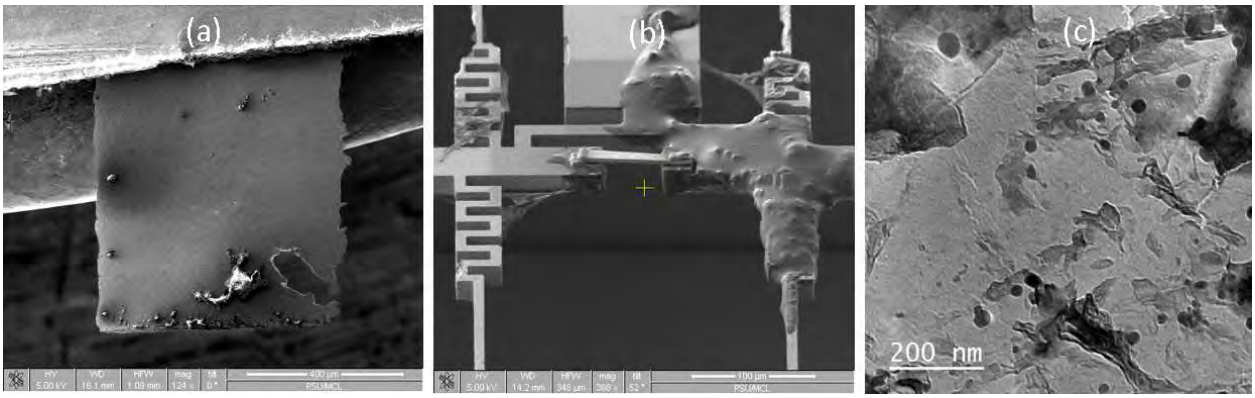

Figure S2.30. (a) TEM specimen preparation from bulk gamma irradiated zircaloy (a) after mechanical and chemical polishing (b) integration with a MEMS device and (c) TEM image of the microstructure.

The literature predominantly practices polishing/focused ion beam techniques, which are serial in nature and are time consuming. In this quarter, we studied the prospect of reactive ion etching of the zircaloy specimens. The technique is used is etching microelectronic materials and the etch rate can vary from few nm/min to microns/min depending on the etch chemistry. If successful, the process can make remarkable contribution to TEM specimen prepation from bulk forms. We prepared a mask and then used a Versalock RIE tool with the following plasma conditions: 20 sccm Cl2 and 30 sccm Ar, RF1 150W, RF2 700W, Pressure 5 mTorr. Figure S2.31 shows our findings.

While Figure S2.30 suggest successful specimen preparation, the electron diffraction images shows significant damage in the specimen, which could be due to irradiation or the specimen preparation process itself. Successive stages in microstructural control using thermo-electro-mechanical annealing. To investigate this we performed Xray diffraction studies on the material before and after irradiation. The results are given in Figure S2.32. The results indicate significant radiation damage that near amorphizes the specimen.

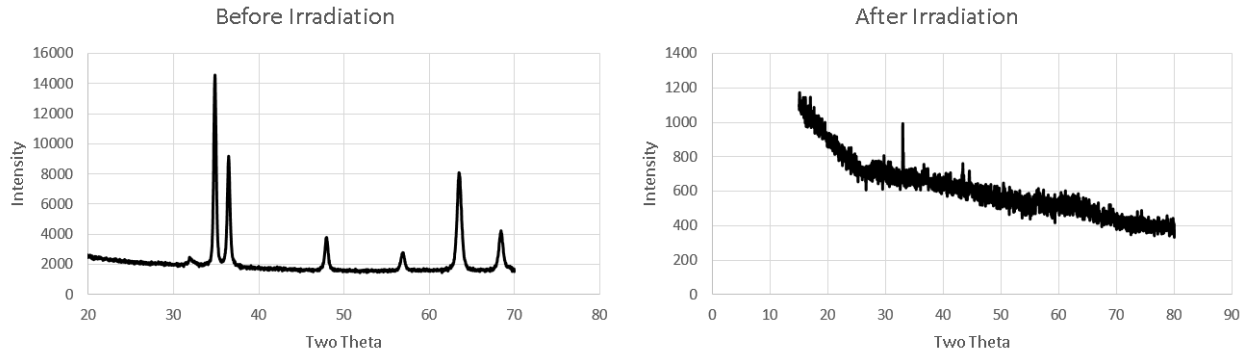

Figure S2.32. Xray diffraction results from irradiated and fresh zircaloy.

To carry out the in-situ TEM testing, we integrated the electron transparent specimens with the MEMS devices. The experiments were not successful because of a specimen holder problem that caused excessive drift in the images. We therefore setup electron backscattered diffraction (EBSD). This technique is SEM based and allows characterization of crystallographic orientation and phases. The primary requirement is that the specimen must be mirror polished. We performed the sample preparation using mechanical polishing with up to 50 nm diamond particle and then with a vibratory mechanical station. Figure S2.32 shows the EBSD scans of the specimen. It very clearly chows the extent of irradiation damage (the grain size became very small). This result agrees very well with the findings from the TEM and Xray diffraction (Figures S2.30 and S2.31)

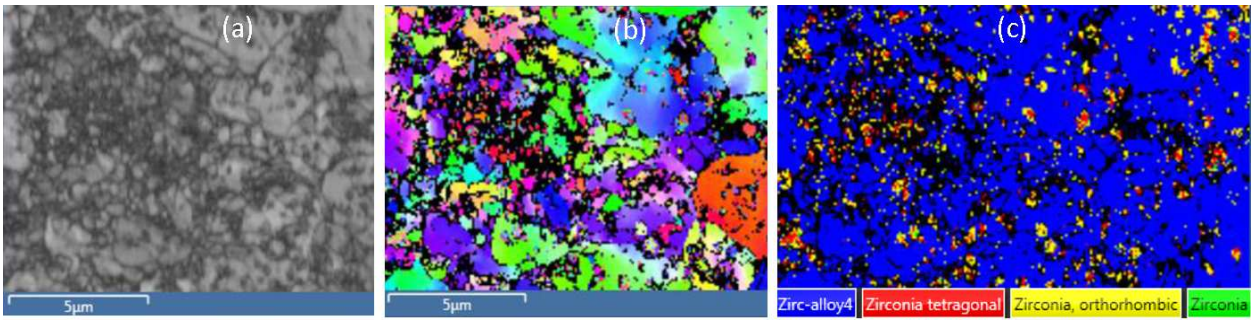

Figure S2.33. EBSD results from irradiated zircaloy suggesting reduction in grain size as well as phase changes.

An important finding from our EBSD study is the phase change, where about 8% of the material transformed from hexagonal to tetragonal configuration. Small amount of orthorhombic and zirconia phases were also observed. In the next quarter, we aim to perform these experiments insitu as function of mechanical stress and thermal loading.

Self Ion Iradiation Effects on Thermo-mechanical Coupling: Our second activity in this quarter

involved sputter zirconium thin films that were irradiated with 800 keV Zr^+ beam using the 6 MV HVE Tandem accelerator at the Sandia National Laboratory. Previously, we performed both mechanical (Figure S2.21) and thermal (Figure S2.26) characterization for dosage from 10^{12} ions/cm^2 to $3.2x10^{14}$ ions/cm^2. In this quarter, we performed extensive tests to investigate how mechanical strain infliences thermal transport. Please note that such coupling does not exist for bulk materials. We have demonstrated that grain sizes below or comparable to electron mean free path can induce such coupling. However, that study involved specimens without any irradiation. We therefore design experiments as function of ion irradiation dose. Specifically, we performed 5 experiments for each of the radiation dosage where the specimens were mechanical strained using a MEMS actuator and simultaneously heated by a MEMS heater. The experiments were performed under an infrared microscope to measure the temperature gradient, which was then used to calculate the thermal conductivity. More details on the experimental procedure is given in Figure S2.25

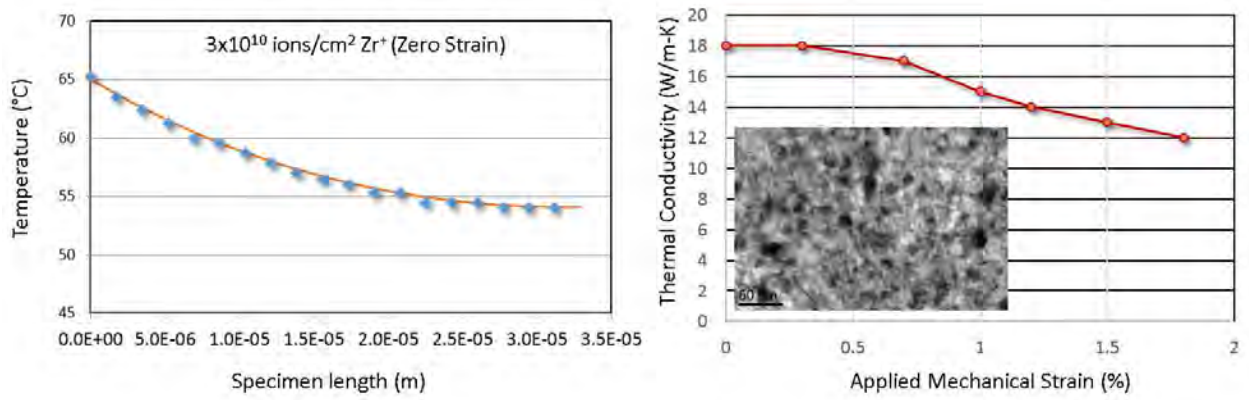

Figure S2.34. Thermo-mechanical coupling for $3x10^{10}$ ion/cm^2 dose (left) thermal conductivity at zero strain (right) strain-thermal conductivity data. The average grain size before irradiation was 10 nm.

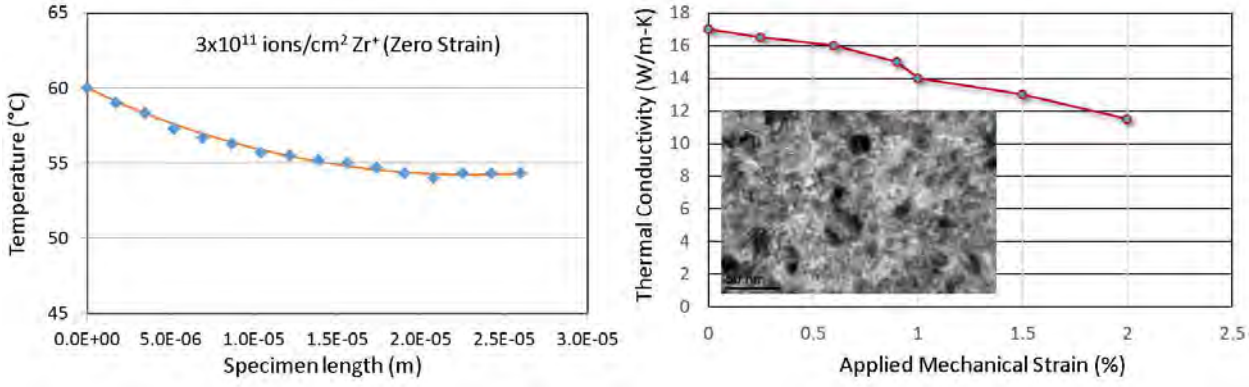

Figure S2.35. Thermo-mechanical coupling for $3x10^{11}$ ion/cm^2 dose (left) thermal conductivity at zero strain (right) strain-thermal conductivity data. The average grain size before irradiation was 10 nm.

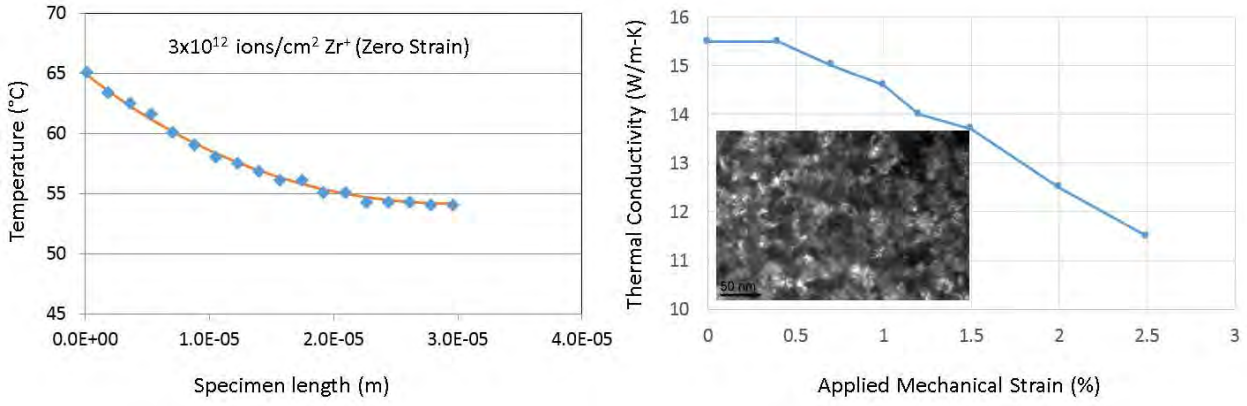

Figure S2.36. Thermo-mechanical coupling for 3x10^{12} ion/cm^2 dose (left) thermal conductivity at zero strain (right) strain-thermal conductivity data.

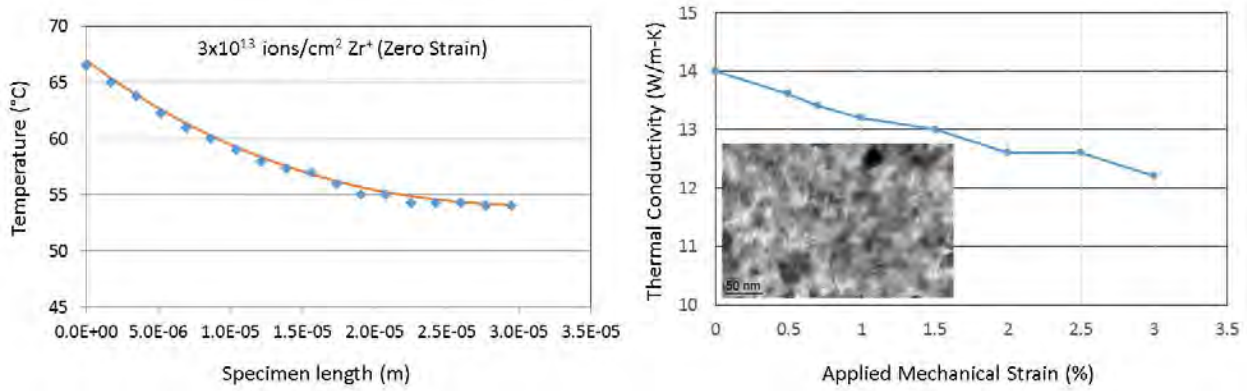

Figure S2.37. Thermo-mechanical coupling for 3x10^{13} ion/cm^2 dose (left) thermal conductivity at zero strain (right) strain-thermal conductivity data.

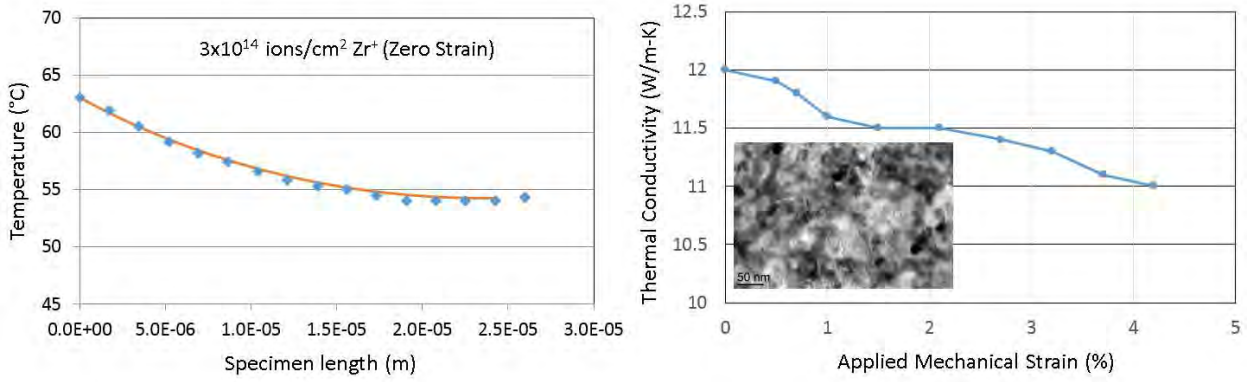

Figure S2.38. Thermo-mechanical coupling for 3x10^{14} ion/cm^2 dose (left) thermal conductivity at zero strain (right) strain-thermal conductivity data.

Figure S2.34-38 show remarkable effect of irradiation on thermal conductivity, which can be

explained by the amount of damage in the lattice. It is also interesting to notice the strong strain-thermal conductivity coupling. However, the experimental data suggests that the grain growth due to irradiation plays a dominat role. As seen in the TEM images, the grain grows to much larger than the electron mean free path (~15 nm in metals). Once the grain size is much larger than this value, the strain-thermal conductivity coupling decays. For example, even at 5% strain, the $3x10^{14}$ ion/cm^2 dose specimen (which also has the larget grain size) show only 8% decrease in thermal conductivity compared to the 33% change in the for $3x10^{14}$ ion/cm^2 dose. These results therefore suggest strong grain size dependence and relatively little influence of deformation itself. This is obvious from the large strain of the highly irradiated specimens, yet smaller change in thermal conductivity.

April 2016 to July 2016 Activities:

Early Stage Damage Prognostics (quantifiable parameter connecting irradiation damage): In this quarter, our objective was to identify and quantify microstructual parameters that can be extracted to connect the irradiation dosage and temperature with the properties. The typical parameter is stacking fault/dislocation loops or defect clusters that are observed as function of the displacement per atom (dpa). However, this is a very cumbersome process to count the areial density of the defects observed in the TEM. The Loops are also visible after annealing processes are carried out. Vacancies are also very critical evolution parameter for irradiation and can be detected by positron annihilation spectroscopy. While the technique is extremely sensitive the problem essentially is its dependence on the (a) alloying elements, for example misleading trend of vacancy density can be seen with irradiation dosage in pure Zr, whereas alloying elements may make the data irreproducible (b) structural traps linked to dislocations, excess defects formed in deformation or polymorphic transformation and the interactions of vacancies with impurity atoms (Atomic Energy, Vol. 67(1), pp. 534-538, 1989). For example, the annihilation parameters are altered when positrons interact with the defects characteristic of lattice instability arising from strain-induced polymorphic transitions in titanium--zirconium alloys.

Since in all the possible forms of radiation damage essentially lowers the electron density as well as velocity, change in electrical resistivity has also been investigated in the literature. The common practice is to study the recovery process. However, the focus of this study was to detect and quanity fy damages at earlier stages for prognostics. It is known that up to neutron fluence of 10^{20} n/cm^2 at temperatures below 100 C does not show any measurable changes (Rosenbaum, 2013). Instead of measuring resistance or resistivity as function of recovery, we designed resonant resistance sensing scheme. This is essentially an AC circuit (instead of conventional DC measurements) that contains RLC elements tuned in such a way that the circuit is driven to its resonant mode. When an AC signal is supplied to a series RLC circuit, AC voltage appears across the resistor R with the same frequency, but at different amplitude and lagging the supply signal. The amplitude of the AC voltage is a function of frequency and is the maximum when the input frequency is equal to the resonance frequency of the circuit. The circuit is shown in Figure S 2.39 below. The resistance R here is the specimen which is irradiated at various dosage. Voltage across the resistance is measured using an nanovoltmeter. The circuit can be modified in the future for automatic detection of the resonance using a micro-controller IC.

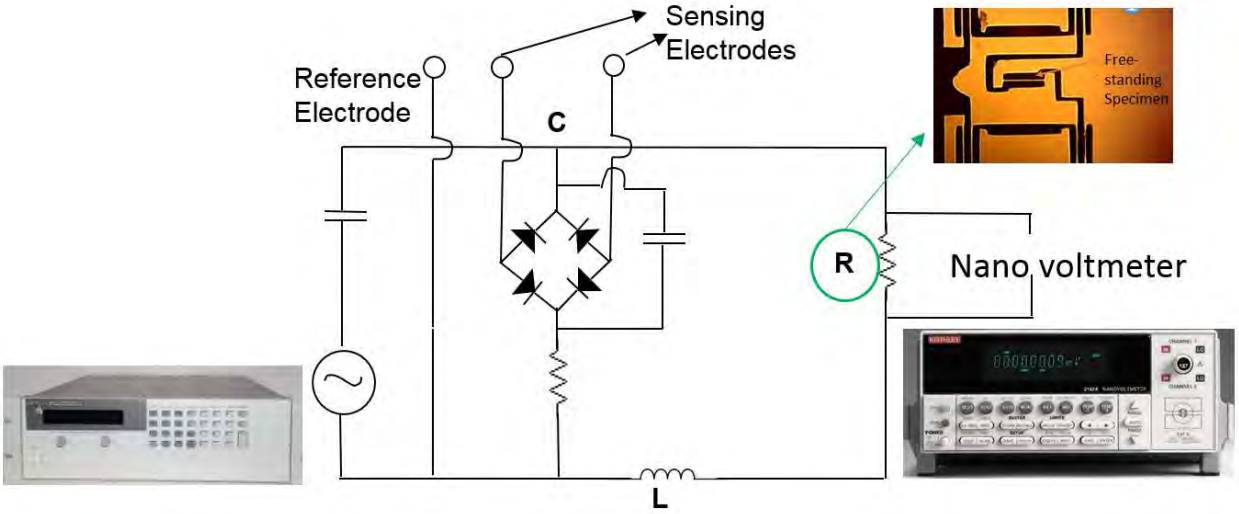

Figure S2.39. Experimental setup showing the circuit for resonant sensing of defects in irradiated specimens. Instead of DC signals, this circuit is driven at resonance, where the circuit is extremely sensitive to minute changes in resistance, capacitance or inductance.

To study the effect of irradiation damage using the resonant circuit, we prepared a set of zirconium thin film specimens that were hanging freestanding in MEMS device. The microelectrodes were co-fabricated with the specimens. These specimens were connected to the circuit shown. The samples were previously exposed to various self ion irradiation dosage as given in Figure S 2.40 below. The experimental results were very promising. However, to convincingly represent the irradiation damages, further experimentations including temperature, contact resistance and time dependence has to be rigorously studied.

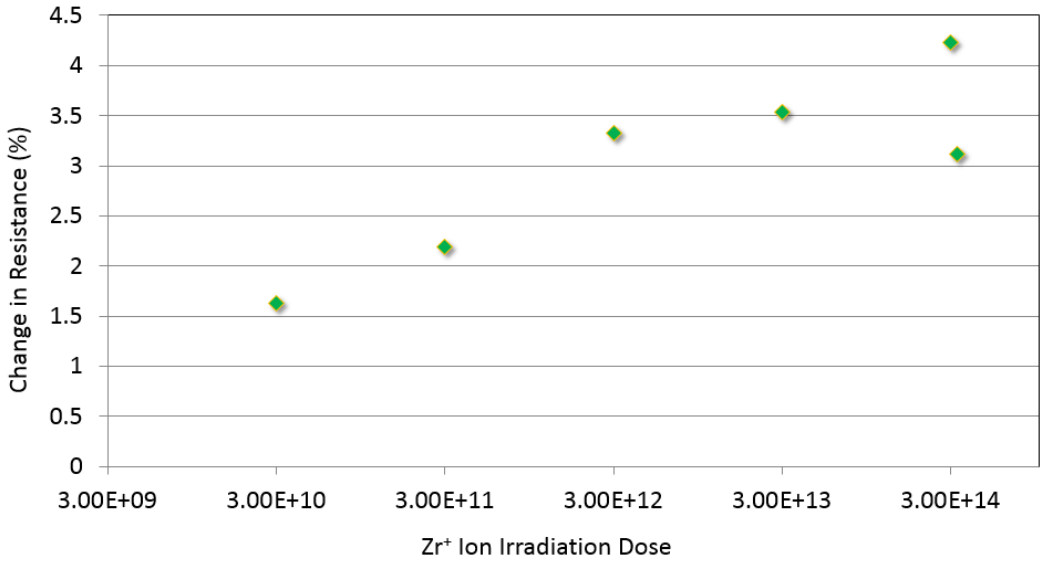

Figure S2.40. Percentage of changes in resonant circuit resistance as function of irradiation.

It is important to note that the conventional practice is to perform such experiments at very low temperatures (<100K), where the resistance to be measured is very low, which increases the resolution of resistivity change measurement. However the thermodynamics of defect induced electron density is probably more important than just the numerical value of the change in the measurements. Or in other words, our measurements might have a temperature dependence that could be avoided at lower temperature levels. We are currently translating the experimental setup for low temperature platforms. The advantage would not only be corroboration of the obtained results but also increase the resolution due to low temperature.

TEM Evidence to Support Data: We performed extensive TEM characterization of the ion irradiated specimens to correlate the microstructure with the data. Figure S2.41 shows the results, which clearly show a pattern, but is inconclusive in its current form. This study will be revisited upon the completion of low temperature study.

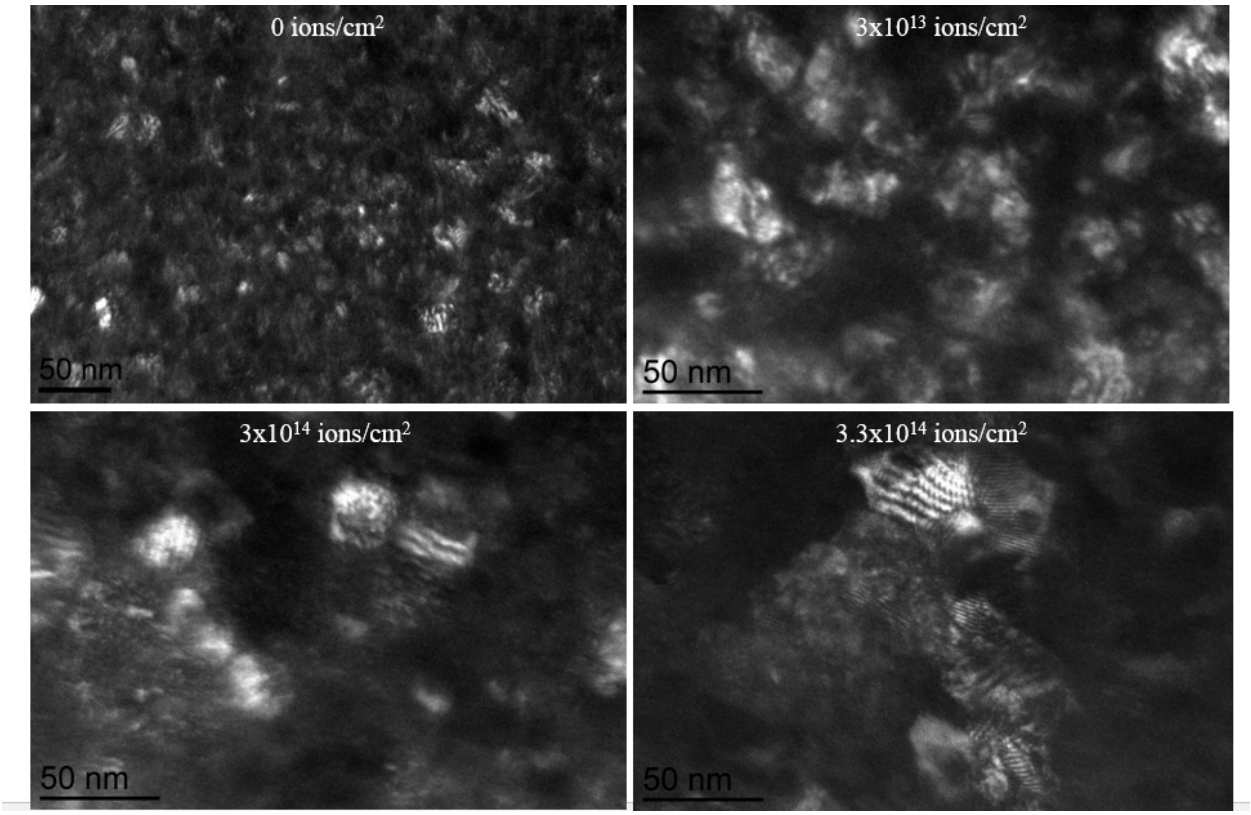

Figure S2.41. Dark field images showing the evolution of defect structures.

Facile TEM Specimen from Bulk: In this study, we explored non-FIB based options for preparing TEM specimens from the bulk. The literature shows increasing utility of focused ion beam based specimen fabrication. However, the procedure is very inefficient for integration with a MEMS device, which is a key feature of the present research project. We explored the option of dry etching of zircaloy after manual polishing to about 20 um thickness. Next, we apply two dry process, one

with CF4 chemistry and the other with Chlorine chemistry.

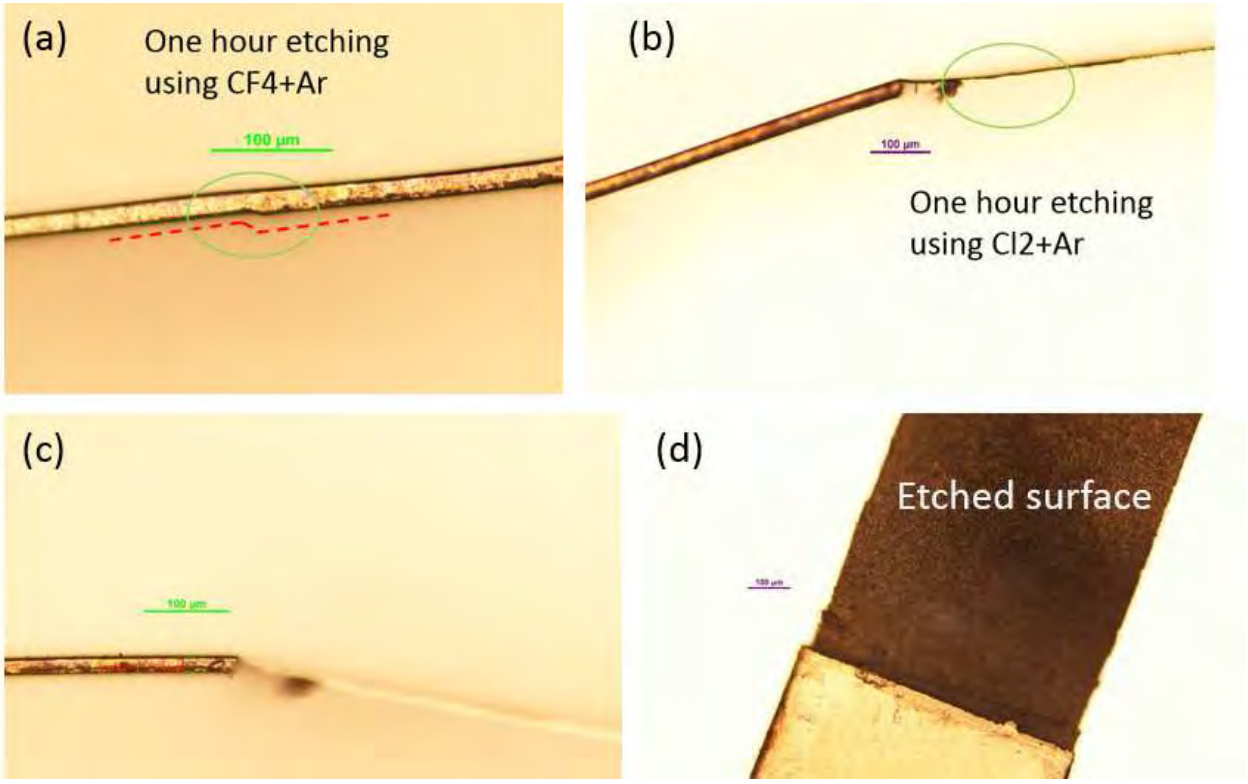

Figure S2.42. Novel dry etch process for FIB-free zircaloy specimen preparation from the bulk

As shown in Figure S2.42, the combined argon chlorine plasma is more effective that the CF4 plasma. The results are very promising because dry etching is the most reliable to way preparing samples free from mis-handling. However, the drawback is the higher surface roughness (very clearly visible under optical microscope) of the etched specimens. Such high surface roughness could be due to microscopic surface contaminants (that do not get etched by chlorine plasma). We are currently extending this study.

We also explored the wet etching process, using HNO_3 (0.5%)+HF (0.25%) solution for 20 min. The sample was checked in SEM. The thickness goes down from around 3um to around 620 nm. Figure S.243 shows out preliminary results. However, surface roughness remains to be an issue if we continue to measure mechanical properties inside the TEM.

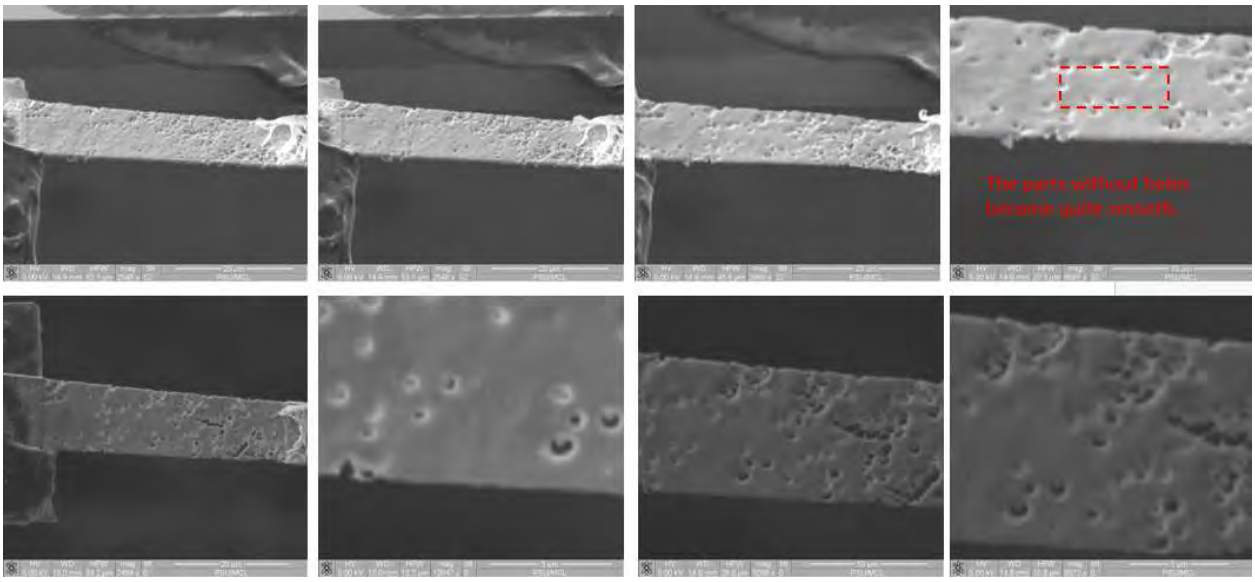

Figure S2.43. Preliminary results on wet etched TEM sample preparation for massively parallel specimen fabrication.

August 2016 to October 2016 Activities: In this quarter, we made further progress on the massively parallel specimen preparation (from bulk irradiated specimens) activity. A representative experiment experiment was performed in-situ inside the TEM to complete the demonstration of the process. A new direction in this quarter was to explore the possibility of actively controlling the microstructure so that irradiation damages could be healed. Preliminary results for this concept is shown in this report, where we pass electrical current inside the specimen insitu inside the TEM to observe the influence on microstructure.

In-situ TEM Testing of the Gamma Irradiated Zircaloy: In the previous quarter, we started developing chemical (dry and wet) etching based massively parallel process for nuclear materials specimen preparation. In this quarter, we performed in-situ TEM tests as well as thermal conductivity tests on these specimens. These results are described below. Figure S2.44 shows the SEM image of a specimen mounted on our MEMS Multiphysics testing device. It also shows the stress strain diagram for the gamma irradiated zircaloy (30 Gy/s). The results indicate significant damage in the specimen in terms of stiffness, however a remarkable increase in the yield strength (about 800 MPa) is seen. It is known that yield strength is related to grain size by the Hall-Petch rule, therefore it is more relevant to cite the grain size. This is obvious after examining our data (Figure S2.44b) with that from the literature. In our specimen, the average grain size is about 3.5 microns, which is 15 times larger than the reference data for mean grain size of 200 nm (Figure S2.44c), therefore one would expect much smaller yield strength compared to the reference (about 585 MPa). However, this is not the case. Rather, our specimen shows 800 MPa yield stress, which might be related to the radiation induced hardening. It is interesting to note that the specimen can sustain about 6% strain, which is rather high for the plane strain configuration of our specimen. For example, 100 nm thin films of metals show very low fracture toughness (<5 MPa $\sqrt{m}$) and mechanical strain (<2%) compared to the bulk counterpart, which arises mainly because of the thickness (plane strain)

governed mechanical loading. Therefore, when considering that our data is plane strain loading while the reference data is bulk (plane stress), one can appreciate that the specimen shows remarkable ductility or fracture toughness compared to bulk. For example, the strain hardening mechanism is clear in our data (the specimen shows unusually large elastic deformation up to 3.5%), which is not seen for the 200 nm grain size reference data. This is clearly shown by the 1 GPa failure stress in figure below. Classical theories from the literature cannot explain the combined increase in strength and ductility. We hypothesize that the dry etching chemistry might have altered the defect structures inside the material to heal them. To prove this, we need to study more specimens and also model the data so that the plane strain conditions are correctly juxtaposed on the literature data (plane stress)

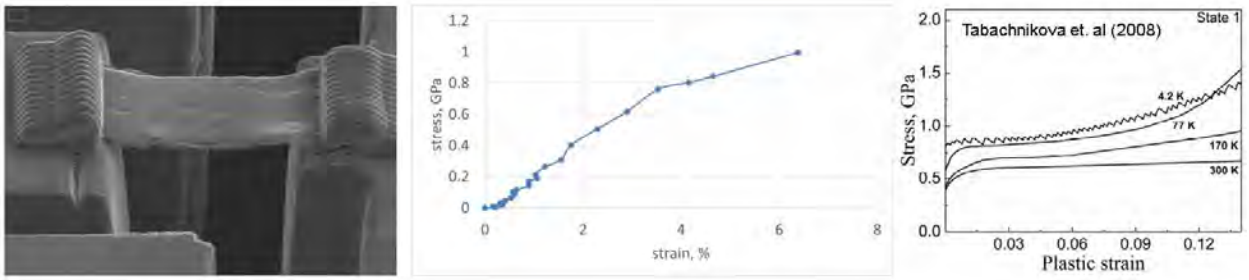

Figure S2.44. (a) SEM image of a gamma irradiated specimen (b) mechanical testing data for a 100 nm thick specimen prepared by massively parallel dry etch (c) data from the literature (Materials Science Forum Vols. 584-586 (2008) pp 452-457)

We then performed in-situ TEM tests on these specimens. Figure S2.45 shows the results.

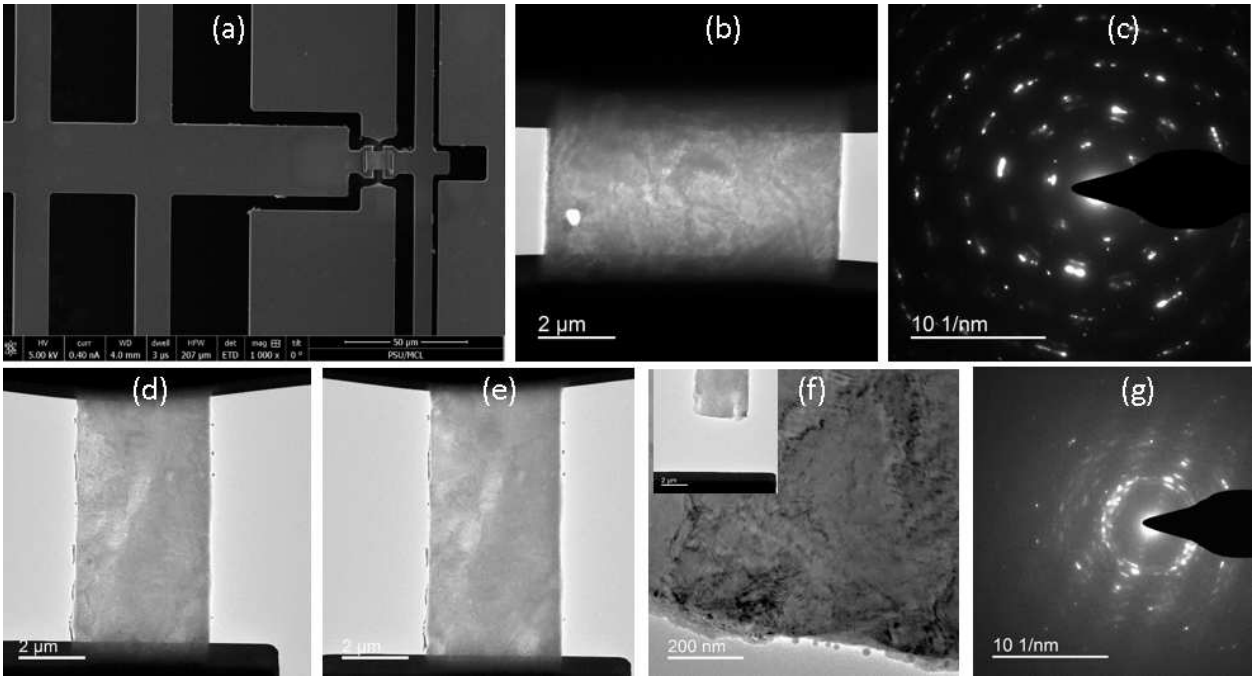

Figure S2.45. (a) SEM image of a MEMS device with specimen (b) low magnification TEM image and (c) electron diffraction data (d) initial and (d) just before failure conditions (f) TEM

image of after failure with inset showing a low magnification image (f) electron diffraction after failure.

In the TEM experiments we observed the change in microstructure as function of externally applied mechanical strain. The strain was directly related to the voltage applied on the MEMS actuators so that 3.5 V is about 6% strain. The TEM images corresponding to the applied voltage (strain values are given in the figure caption) is shown below. Very clearly, strength and ductility were influenced by the motion of the sub-grain structures as shown. The effect of strain not just to move them but also to reduce their effective volume content. This is clearly seen by comparing zero strain and the prior to fracture instants (Figures S2.46 a and c). It is still unclear how the chemical etching processes result into such ultrafine microstructure. Nevertheless, their role is to impede the dislocation motion, thereby increasing the yield strength as seen in the stress strain diagram (Figure S2.44b). These sub-grain structures also indicate the origin of the strain hardening observed during the mechanical testing.

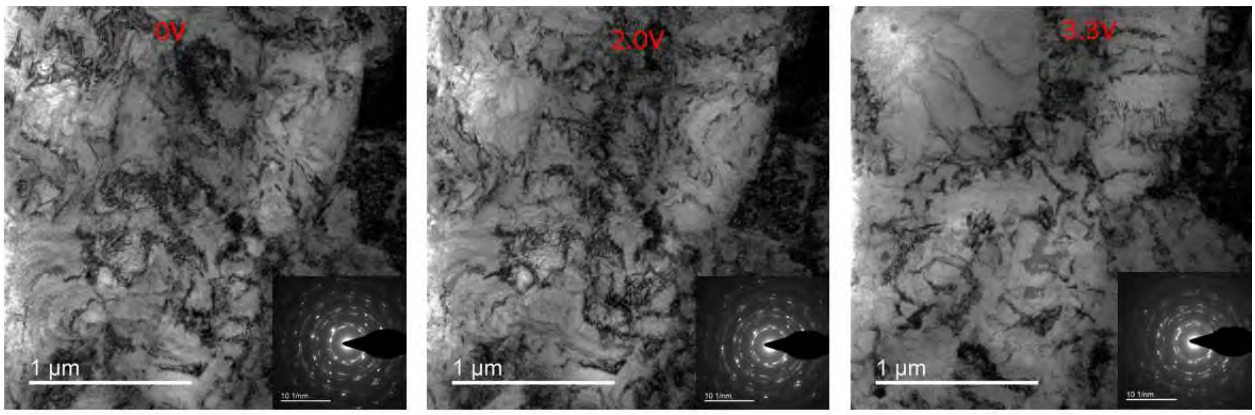

Figure S2.46. TEM images (with inset showing the electron diffraction pattern) for the specimen at (a) 0% (b) 2.5% and (c) 6% applied strain.

Microstructural Control In-situ TEM: This research direction is motivated by our hypothesis that moderate current density can bring about significant changes in radiation damaged metals. This may lead to active control of microstructure. To study this hypothesis, we perform insitu TEM electrical annealing experiments.

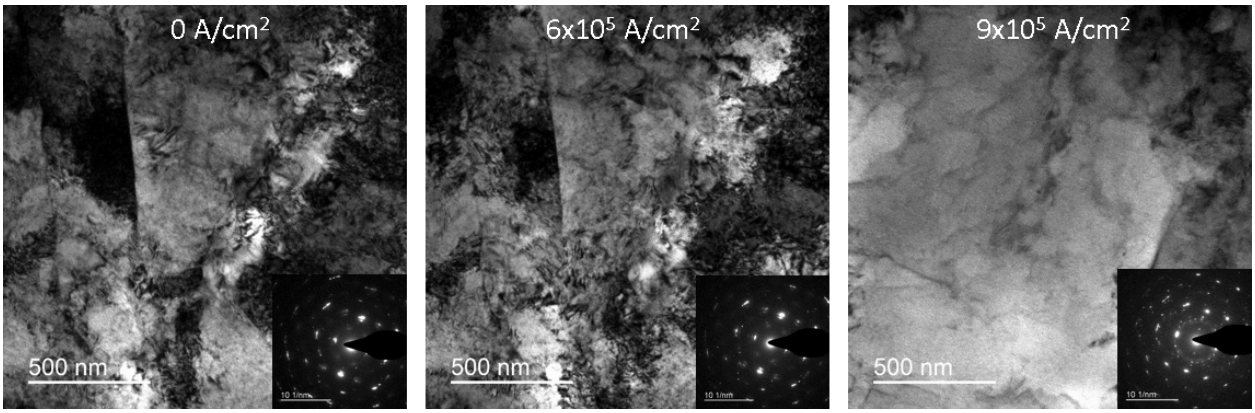

Figure S2.47. TEM images (with inset showing the electron diffraction pattern) for the specimen at various levels of applied current density (a) 0 (b) $6x10^5$ A/cm^2 and (c) $9x10^5$ A/cm^2.

Remarkable influence of the microstructure is seen in Figure S2.47. It appears that the electrical current is able to sweep out the sub-grain structures and defects. The electron diffraction patterns (inset) also show this clearly through sharpening of the spots and the rings. The preliminary results therefore are highly encouraging for a comprehensive study not just controlling the microstructure, but also measuring the corresponding mechanical properties.

Finally, intriguing microstructural dynamics is observed at even higher (~$1x10^6$ A/cm^2) current density in the time space. Figure S2.48 shows how the microstructure changes with time for a constant current density. Here, the same locations are shown for two different levels of current density, except allowing about 5 minutes for the microstructural changes to occur.

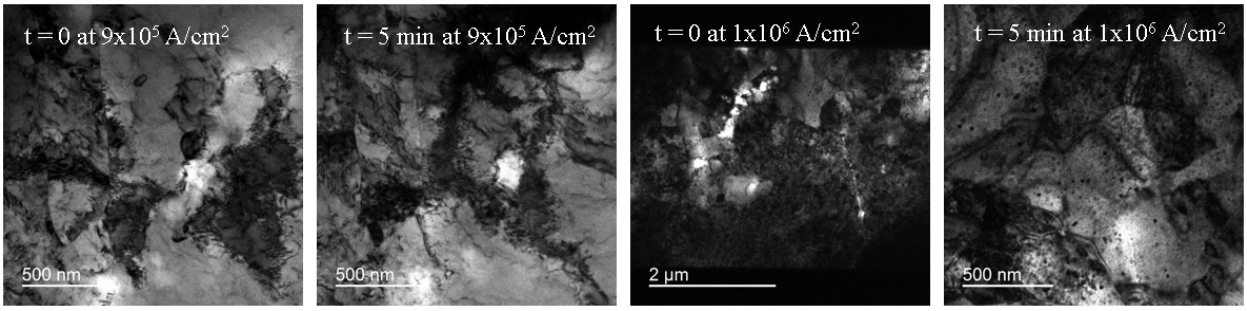

October 2016 to December 2016 to Activities: In this quarter, we analyzed the experimental data obtained on thin films of Zr, zircaloy and bulk zircaloy. Since this is the last quarter of this project, we also assessed the achievements of the in-situ TEM and thermo-mechanical characterization as proposed. In addition to the proposed activities, a new direction, i.e., thermo-electro-mechanical treatment based microstructural rearrangement was introduced and demonstrated with preliminary results. These are summarized below,

Size Effects on Mechanical Properties under Radiation: This study was motivated by the hypothesis that nanocrystalline zirconium would exhibit better resistance to irradiation by reducing irradiation

induced dislocation and cavity density. This is because grain boundaries in nanocrystalline systems are effective sinks for radiation-induced defects. Also the volume fraction of grain boundary increases non-linearly with grain size increasing the radiation tolerance. In nanocrystalline materials, the fraction of grain boundaries significantly increases and the diffusion length for interstitials to reach the grain boundaries greatly shortens, both of which indicate the pronounced role that grain boundaries may play in enhancing the radiation tolerance. A large increase in the fraction of grain boundaries and shorter diffusion length for interstitials to reach the grain boundaries indicate the pronounced role of that grain boundaries may play in enhancing the radiation tolerance. From a fundamental perspective, mobility of the grain boundaries now becomes is the central mechanism behind microstructural alterations during radiation. There is also indication that radiation tolerance could be size dependent and strongly influenced by temperature.

A contribution of this study was developing procedures for nanocrystalline (in particular, grain size around 10 nm compared to the typical values around 100 nm in the literature), which allowed us to study the extreme size effects. This is achieved by physical vapor deposition, where we were able to obtain specimens for both zirconium and stoichiometric zircaloy. A challenge was to integrate these specimens with MEMS based mechanical testing setup, which arised from the residual stress of the specimen. In-situ TEM tests were performed on both unirradiated and Zr^{+} ion irradiated specimens. Figure S2.49 shows the essence of the experimental results.

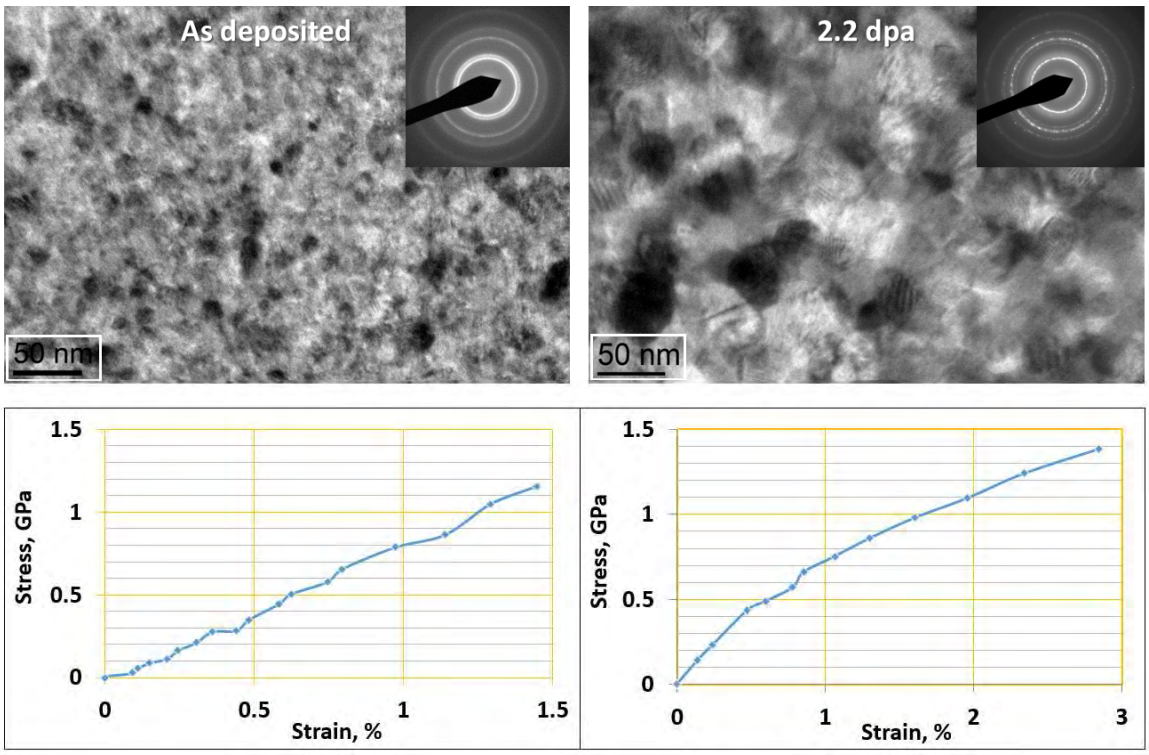

Figure S2.49. Size and irradiation effects on mechanical properties (left) unirradiated and (right) irradiate at 2.2 displacement per atom damage.

We found that the primary effect of self-ion irradiation is to inject vacancies and their clusters in the nanocrystalline metal. How these defects instrument the evolution of microstructure (and hence properties) appears to be strongly governed by the resulting grain size. Below a crossover grain size, it is theorized that the grain interior is dislocation starved and a large fraction of the atoms reside in the grain boundaries, away from their equilibrium position. At this grain size, irradiation implies abundant supply of vacancies, which on one hand decrease elastic stiffness, on the other hand promote diffusional grain boundary migration. Grain growth is very sensitive to the applied damage level. We also found that above the crossover size, higher doses of irradiation implies dislocation loops and clusters can be accommodated at least partially by the grain interior. It is hypothesized that this results in the observed plastic deformation in the assumed previously dislocation starved grains.

For grain sizes below 100 nm, no evidence of active dislocation free channels or shear bands in the strain hardened grain interior were observed. As a result and contrary to plastic instability typical in bulk materials, we observe sustained strain hardening indicating improved radiation tolerance at the 10-30 nm grain size range (Figure S 2.49). In this study, we suggest the existence of a critical grain size for favorable grain size effects to manifest, which is 20 nm for the study of Zirconium here. For metallic materials, this could be the point of inflection in the strength vs. grain size plot, or the grain size below which reverse Hall-Petch behavior is seen. Theoretical models suggest this critical or crossover size (d_c) to be in the range of 12-15 nm for most metals. We hypothesize that radiation induced defects are actually beneficial at this grain size, which are normally dislocation starved. In this case, the defects provide the nanocrystals mechanisms for both grain growth and plastic deformation.

Size Effects on Thermo-mechanical Properties under Radiation: Thermo-mechanical coupling was studies from two perspectives, (i) temperature dependent fracture toughness and (ii) strain dependent thermal conductivity. This constituted a comprehensive coupling that is initiated by both thermal and mechanical domains. The first set of studies were performed inside the TEM so that the mechanisms behind fracture could be visualized. The second set was studied under an infrared microscope to capture the thermal transport.

We observed that the temperature effect on fracture toughness is primarily due to the grain growth. For grain sizes below 25 nm, the fracture toughness is very small. However, this is not just due to the absence of plasticity (the grains are starved from statistically significant dislocations). Rather, the mechanics is driven by the specimen geometry (plane stress), which must be accounted for. Therefore, as the grain sizes grow, they are populated with dislocations and this mechanism inhibits fracture. Nevertheless, the fracture toughness never reaches the bulk value, which are typically reported under plane strain condition. The grain growth is also temperature dependent and slows down at higher temperatures, most likely because of the back-stresses from the thermo-mechanical stresses at the grain boundaries. This is evident from Figure S2.50.

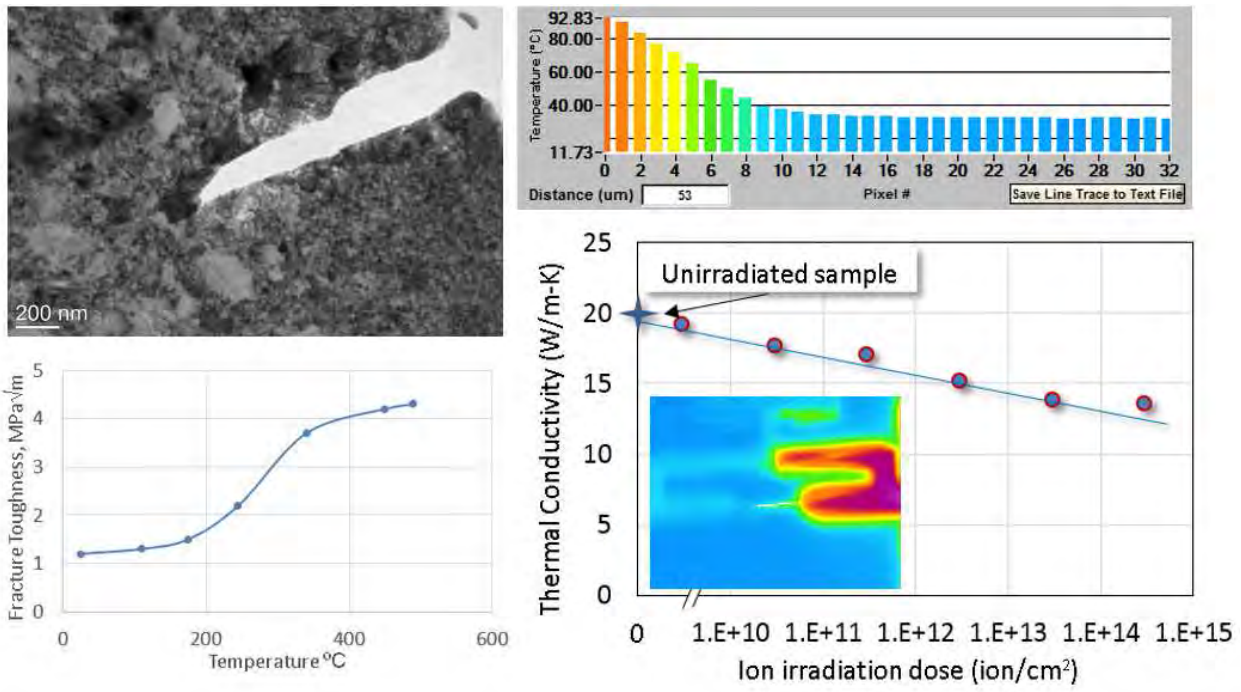

Figure S2.50. Thermo-mechanical coupling (a) temperature-fracture toughness and (b) irradiation – thermal conductivity.

We have also performed thermal conductivity measurements on as-deposited zirconium and irradiated specimens. For the grain sizes relevant to this study, there are two competing mechanisms influencing thermal transport. Firstly, thermal conductivity is expected to decrease with increase in ion irradiation doses because of the introduction of new defects. Obtained results are consistent with this premise where thermal conductivity drops down to 13.6 W/m-K for irradiation of $3x10^{14}$ ions/cm^2 (2.1 dpa). This is similar to the finding on UO2 (about 55% decrease for the high fluence and 35% for the low fluence) specimens. The nanocrystalline nature of zirconium thin film means that the electron scattering occurs primarily at the grain boundaries since the mean free path of electrons is in the same order of grain size. The ion irradiation induces defects (vacancy or interstitial) within the lattice. The grain boundaries act as sinks to the defects induced by ion radiation. This is attributed to the 'loading-unloading' effect of the grain boundaries especially in nanocrystalline metals. Not all the radiation induced defects are loaded near grain boundary. In such a case, the electron scattering in the grain interior becomes significant at high defect volume. Accumulation of defects at the grain boundaries should further increase the electron scattering thereby decreasing the thermal conductivity. The second mechanism is the irradiation induced grain growth. The grains grow from nominally 10 nm to about 40 nm. Electron mean free path in zirconium is about 10 nm, which means that heat transfer in the un-irradiated samples is strongly influenced by the confinement of electrons inside individual grains and the increased scattering at the grain boundaries. For grain sizes larger than the electron mean free path, thermal conductivity is expected to increase because the confinement effect is relaxed. Therefore, this mechanism tends to increase the thermal conductivity with irradiation. Figure S2.50 suggests that the decrease of the thermal conductivity due to the defects dominates the increase due to grain growth, since the thermal

conductivity trend is downwards.

Alternative explanation of the decreasing trend of the thermal conductivity is the morphological change in the material during irradiation. In-situ TEM studies show the electron diffraction patterns clearly indicating oxidation of zirconium at about $3x10^{14}$ ions/cm^2 (2.1 dpa). The appearance of an additional ring representing the {220}planes in ZrO_2 can be explained by the formation of an oxide at the metal surface and the strongly enhanced athermal oxygen diffusivity due to ion irradiation. Thermal conductivity of ZrO_2 is phonon dominated and is about 1.7 W/m-K, which is more than 10 times smaller than that of zirconium, which could reduce the overall measured value of thermal conductivity.

SECTION 3 (S3)

Environment, Temperature, and Microstructure Dependent Thermomechanical Coupling Measurements on Irradiated Samples (Dr. Vikas Tomar)

STATUS:

Task 4: Setup Zircaloy samples obtained from Task1 to various test environments containing oxygen, water, CO_2, sodium containing oxygen, and LiOH solutions and perform high temperature and chemistry dependent nano/micro thermomechanical measurements based on surface enhanced Nanomechanical Raman spectroscopy (COMPLETED)

Task 6: *In-situ* Nanomechanical and micromechanical SERS based measurements of environment dependent thermal conductivity, diffusivity as a function of stress/strain (COMPLETED)

Task 7: Identification of key microstructural parameters that link irradiation induced damage and environment dependent thermomechanical coupling based on quantified data (COMPLETED)

Task 9: *In-situ* Nanomechanical and micromechanical SERS based measurements to understand the effect of temperature up to 1000 ^oC on environment dependent coupled thermal and mechanical properties.

Year 3 Goal: This task has been ongoing, (COMPLETED).

Task 10: Establishment of microstructure-irradiation-stress-environment-temperature correlations using Bayesian uncertainty quantification procedures that affect separate effect multiphysics properties of Zircaloy. Development of empirical relations predicting such correlations.

Year 3 Goal: This task has been ongoing, (COMPLETED).

In the following results from the tasks are described.

Part I: Nanomechanical Characterization of Thermo-mechanical Properties of Irradiated Zirconium with Consideration of Microstructure

Sample Preparation

For this study, two manufacturing processes are considered: rolling, as well as rolling and annealing. Additionally, two levels of irradiation are considered: 1 keV and 100 eV. Each sample was irradiated to a total fluence of $5x10^{22}$ m^{-2}, at these energies, prior to nanoindentation testing. In total, six different irradiated Zr samples were considered. In addition to these, unirradiated rolled and rolled and annealed Zr samples were also tested for the purpose of comparison. The rolling process is such that the material is plastically deformed by compressive forces between two constantly spinning

rolls. These forces act to reduce the thickness of the metal and affect its grain structure, as well as to induce compressive residual stresses. Annealing is a process where a metal is heated to a given critical temperature and then allowed to cool slowly. This softens the material and relieves internal stresses, as well as increasing the homogeneity of the microstructure. Prior to testing, each sample was mechanically polished and then cut into pieces approximately 3 mm x 3 mm. The rolled and rolled and annealed samples, as well as their respective microstructures are shown in Fig. S3.1.

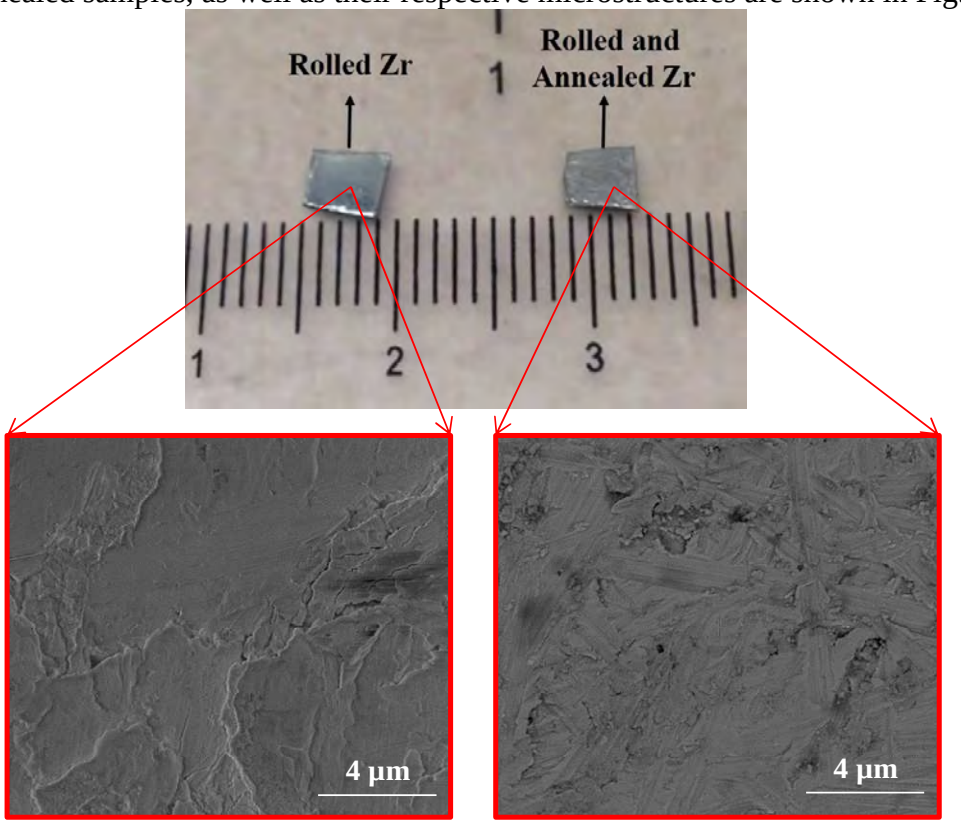

Figure S3.1: Rolled and rolled and annealed Zr samples and their respective microstructures. Rolled Zr grains are significantly smaller and grain boundaries and much more clearly defined in comparison to rolled and annealed Zr grains.

The rolled samples tend to have smaller, more defined grains, while the rolled and annealed samples tend to have larger grains, with boundaries that are more difficult to distinguish, which supports our expectations relative to the manufacturing processes used. A visual comparison of the microstructure of each sample variation are shown in Fig. S3.2.

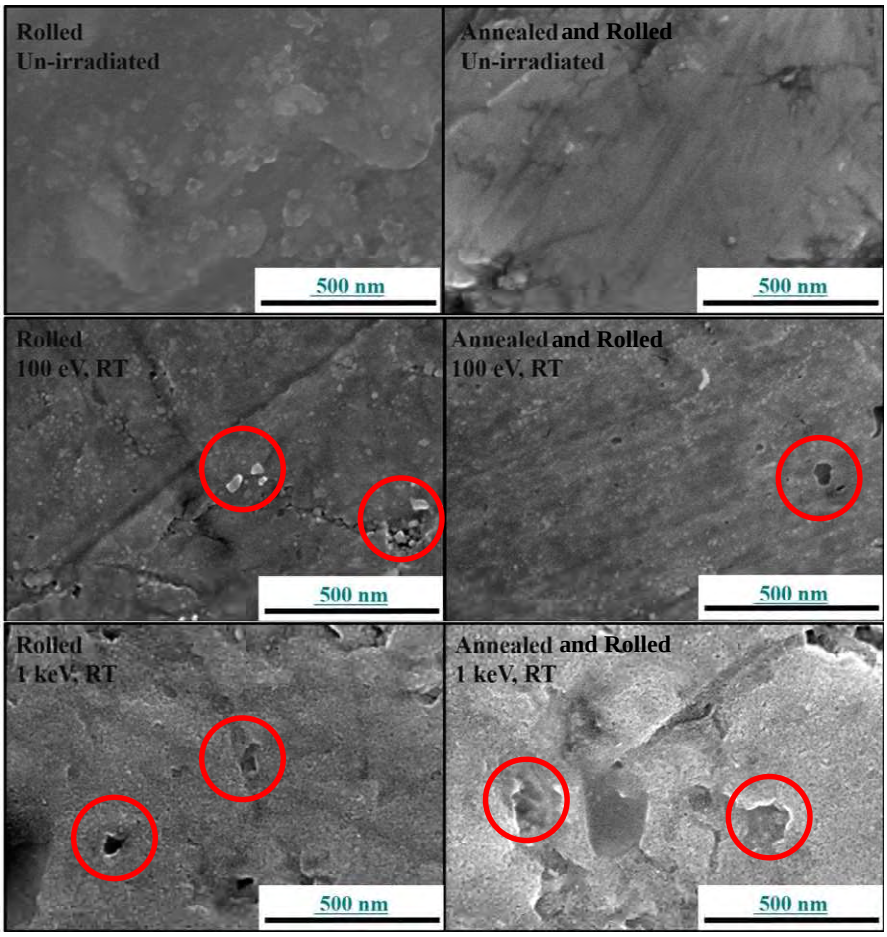

Figure S3.2: SEM images of each sample variant. Rolled 100 eV samples exhibit small blisters and surface voids, while the rolled and annealed counterparts exhibit only surface voids. Surface voids are abundant on both 1 keV samples, but blisters are absent. These features are shown in red.

The 100 eV irradiated sample variants exhibit the formation of small blisters and surface voids. The damage is more apparent on the rolled sample, but both samples clearly exhibit damage. The 1 keV irradiated samples exhibit small blisters, similar to the 100 eV irradiated samples, but the void sizes increase significantly. These voids are more apparent on the rolled and annealed samples.

Experimental Procedure

High temperature nanoindentation was performed on each sample. The nanoindentation testing scheme included a loading period, with maximum load being achieved in 25 seconds; a dwell period of 500 seconds; and an unloading period, with the load returning to zero in 25 seconds. All tests were performed using a multi-module mechanical tester (Micro Materials Ltd., UK) shown in Fig. S3.3-(a).

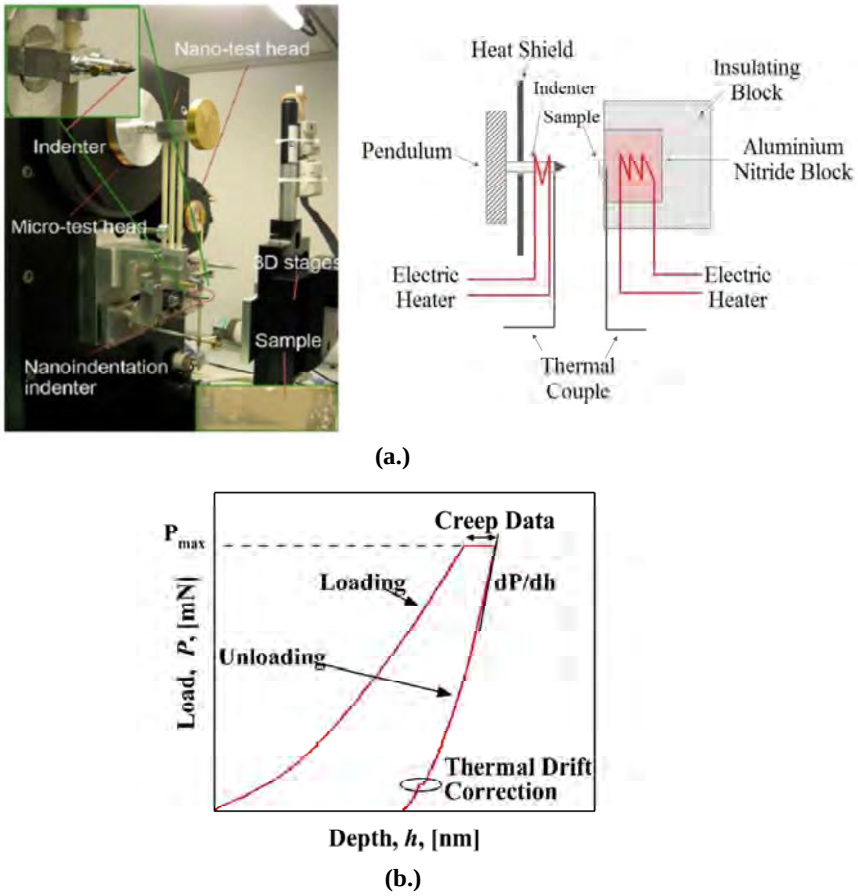

Figure S3.3: Nanoindentation Experimental Setup: (a.) NanoTest multi-module mechanical testing apparatus and schematic diagram of indentation stage (b.) example indentation load-displacement curve.

Before testing, both the sample and the indenter tip were heated to the desired temperature which was closely monitored using thermocouples. After reaching the desired temperature, the apparatus is kept inactive for 2 hours in order to achieve thermal stability. The remaining parts of setup are separated by a heat shield, in order to maintain them at room temperature. The samples were fixed to the indentation stage using a ceramic glue and the area function calibration was performed using fused silica. Tests were then performed 250ºC and 450ºC and using four different loading rates: 2 mN/s, 5 mN/s, 10 mN/s, and 20 mN/s. In all cases, a diamond Berkovich type indenter with a 20 nm radius was used to perform indentations. Indentations are made in an array, with 30 micron separation between indentations at the given loading rate, and 50 microns between indentations at different loading rates and different temperatures. For a given loading rate, temperature, and sample; 10 indentations were made for result verification. As the indentations are performed, the load and depth are recorded electronically and a thermal drift correction is automatically implemented. This is done during the unloading period, where 10% maximum load is held for 500 seconds, while the depth is monitored. Between each test, the compliance, as well as the area function was re-calibrated to ensure that there is no influence from potential indenter blunting or plastic deformation.

Experimental Results

Figure S3.3-(b) represents the typical load displacement curve for an indentation experiment performed at room temperature with 400 mN maximum load. In this case, the sample is loaded up to the maximum load and the maximum load is held for around 500 seconds before the unloading period. The reduced modulus in this case is computed from the slope of the unloading curve, hardness is calculated from the maximum load and corresponding maximum depth, and creep data is extracted from the dwell period. Additionally, the indentation stress-strain curves are produced using the loading portion of the load-depth curve.

Oxide Layer

The properties of the samples were measured at high temperature in an open environment. The surface of the samples oxidizes at high temperatures due to the exposure to oxygen. This oxide layer leads to erroneous results in the indentation size effect analysis. The thickness of oxidized layer needs to be determined and adjusted to correctly characterize the hardness size effects. The samples were heated to 800°C and the temperature was maintained for 8 more hours to let sample oxidize and then the temperature was decreased to room temperature gradually. The oxidized layer of the Zr alloy is consisted of elongated columnar grains of ZrO_2. Pawel R et. al. Pawel et al. (1979) measured the parabolic rate constant κ_p of Zr alloy at the temperatures from 900 to 1500°C. The parabolic rate constant κ_p at 800°C is calculated as 1.61 (10^{-2}) $g^2m^4\ s^{-1}$. The linear oxidation rate κ_p' in $m^2\ s^{-1}$ is then calculated by

$$\kappa_p' = \kappa_p \left(\frac{Mo_x}{\rho o_x b Mo}\right)^2, \quad (1)$$

Where Mo_x is the molar mass of ZrO_2 (123.22 g/mol), Mo is the molar mass of oxygen (16 g/mol), ρo_x is the density of ZrO_2 (201.94 (10^6) g/m^3) and b is the number of oxygen atoms in M_aO_b (b = 2). As a result, κ_p' is calculated as 5.86 (10^{-18}) $m^2\ s^{-1}$. The thickness of the oxidized layer can be calculated by

$$s = \sqrt{\kappa_p' t}, \quad (2)$$

The thickness of the oxidized layer of Zr alloy at 800°C after heating for 8 hours is around 400 nm, which is in agreement with the oxide layer measurement from the SEM images shown in Fig. S3.4.

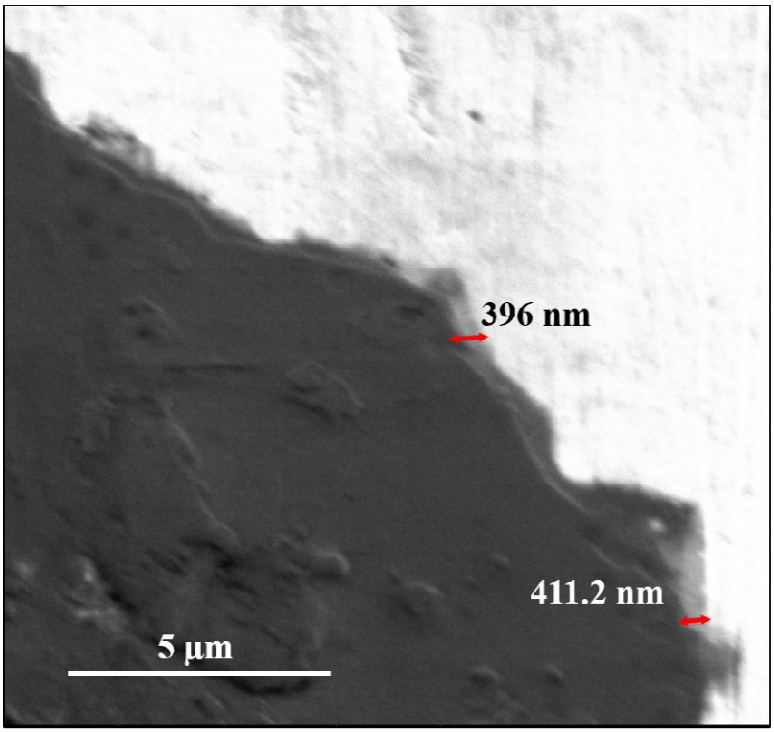

Figure S3.4: SEM images showing the oxide layer thickness on Zr alloy after heating for 8 hours in open environment.

Size Effect

The indentation size effect was observed in all samples in the case of reduced modulus and hardness. Fig. S3.5 shows the effect of depth on these properties. The increasing loading rates correspond to an increase in maximum load and subsequent increase in maximum depth. This allows the indentation size effect on the mechanical properties to be observed and allow for a representative loading rate to be chosen. This representative loading rate corresponds to the lowest loading rate which leads to mechanical properties that are invariable with depth. Sources of variation in these properties with depth can arise from surface and substrate effects, depending upon the indentation depth. It is observed that in each case, this trend follows a decreasing exponential curve, with each property reaching steady-state at or before 4000 nm. Thus, the 20 mN/s loading rate data is used as the representative loading in all cases. This calculation is crucial to the analysis of results in nanoindentation, due to the fact that at low depths, surface effects can greatly influence properties, while at high depths, the substrate can do the same.

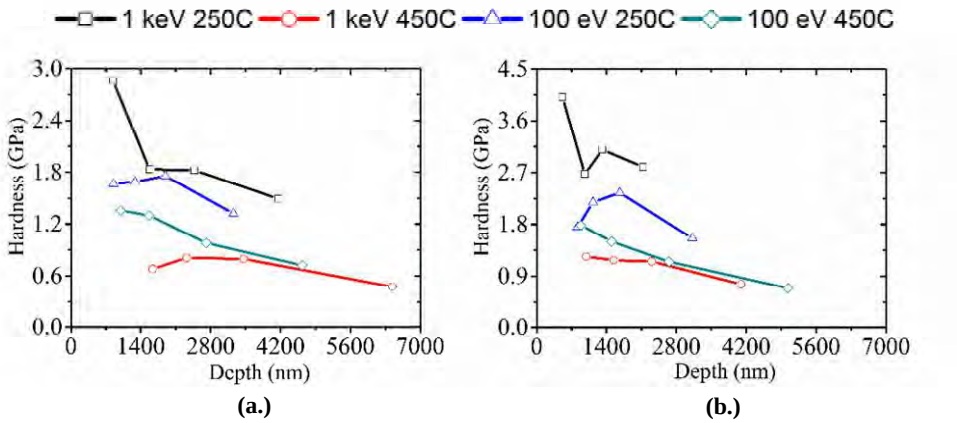

Figure S3.5: Indentation size effect on hardness of (a.) rolled Zr (b.) rolled and annealed Zr. Hardness decreases with increasing indentation depth to a saturation point. The range for depth invariant hardness varies depending on the sample configuration, but is generally between 2 and 6 µm.

In addition to the effect of indentation depth on mechanical properties, the effect on creep properties is also reported for two loading rates in their respective sections.

Reduced Modulus

Reduced Modulus is calculated using the Oliver-Pharr Oliver and Pharr (1992) method given by

$$\frac{dP}{dh} = \frac{2}{\sqrt{\pi}} E_r \sqrt{A}, \quad (3)$$

where $\frac{dP}{dh}$ is the slope of the unloading portion of the load-depth curve, A is the area function of the given indenter, and E_r is the reduced modulus. In all cases, a Berkovich-type indenter was used, meaning that the theoretical area function is given by

$$A = 4{h_c}^2 \tan^2\theta = 24.504{h_c}^2, \quad (4)$$

where h_c is the depth corresponding to the difference in depth between the circle of contact of the indenter and the maximum depth of indentation. However, slight imperfections in the indenter geometry can lead to significant error in the area function calculation and thus, the area function used was obtained by performing indentation tests on a sample of known reduced modulus and hardness, in this case fused silica. The calibration of the area function is repeated after each test in order to ensure that blunting and plastic deformation does not lead to error in the calculation of mechanical properties. After obtaining the reduced modulus of the Zr samples in each case, these values can be related to the Young's modulus of each using the following relation

$$\frac{1}{E_r} = \frac{1-\nu^2}{E} + \frac{1-\nu'^2}{E'}, \quad (5)$$

where E is Young's modulus, ν is Poisson's ratio, and the primed values correspond to the properties of the indenter itself. The results of the reduced modulus calculations are shown in Fig.

S3.6 as function of loading rate.

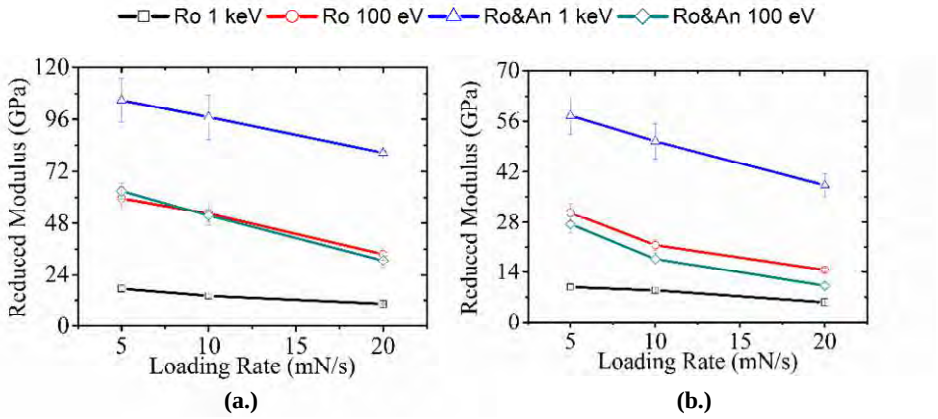

Figure S3.6: Reduced Modulus as a function of loading rate at (a.) 250°C (b.) 450°C. Reduced modulus is highly dependent on microstructure (manufacturing) and irradiation in the 1 keV case. The 100 eV case is nearly invariant with microstructure.

In all cases, with an increase in temperature, there is a decrease in reduced modulus, as expected. The rate at which reduced modulus decreases with temperature varies between cases, with rolled and annealed Zr 1 keV being highly dependent on temperature. The reduced modulus of unirradiated Zr is approximately invariable with manufacturing process at all temperatures. The 100 eV irradiated samples show only slight variations from the unirradiated case, although the temperature dependence of these samples increase. However, we observe a significant change in reduced modulus in the remaining cases. In the case of rolled Zr, the 1 keV irradiated samples see a decrease in reduced modulus compared to the unirradiated case and negligible change in temperature dependence. The opposite is true in the case of rolled and annealed Zr.

Hardness

Hardness is calculated, again, using the Oliver-Pharr method, given by

$$H = \frac{P_{max}}{A}, \tag{6}$$

where P_{max} is the maximum indention load and A is the area function. The results of the hardness calculations as a function of loading rate are shown in Fig. S3.7.

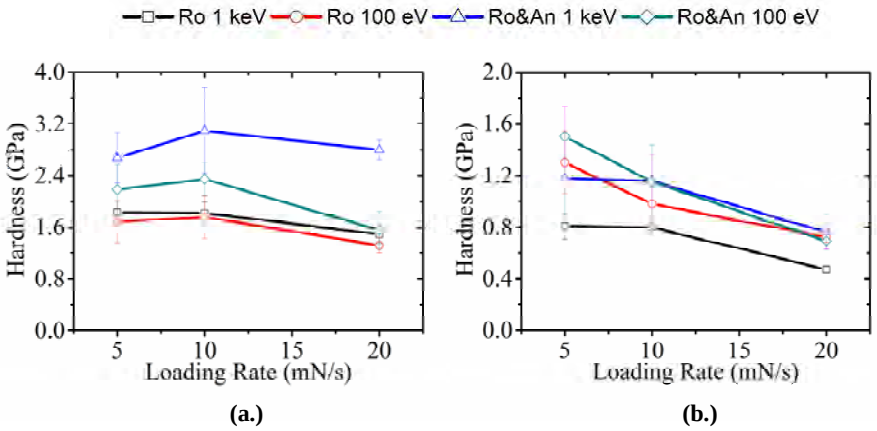

Figure S3.7: Hardness as a function of loading rate at (a.) 250°C (b.) 450°C. Hardness is almost universally greater in the rolled and annealed case. There is a dependence on irradiation as well, but is case dependent.

Hardness also decreases as a function of temperature in all cases, which is as expected, due to the material softening with increasing temperature. An irradiation induced hardening has been observed by other authors in the case of radiation-exposed materials Ahmad et al. (2014) and we see this trend here as well. We observe many of the same trends in hardness as we previously observed with reduced modulus. The hardness of unirradiated Zr is invariable with manufacturing process, as is 100 eV irradiated Zr. We observe the greatest increase in hardness from 1 keV irradiation in the case of rolled and annealed Zr.

Creep Properties

To observe and quantify the creep behavior of the Zr samples at elevated temperatures, the Power-Law creep relation was used. The creep strain rate using Power-Law creep Gan and Tomar (2010; Dean et al. (2013) is given by

$$\dot{\varepsilon} = A\,\sigma^{n} exp\left(-\frac{Q}{RT}\right), \tag{7}$$

where σ is the stress, n is the stress exponent, Q is the creep activation energy, R is the universal gas constant, and T is the temperature. The creep rate is calculated using the dwell period of the indentation test. The indentation depth is recorded, while being subjected to a constant load, over a given period of time, in this case, 500 seconds. A curve fitting is performed on the resulting depth-time data using the following relation Gan and Tomar (2010)

$$h = h_i + at^b + kt, \tag{8}$$

where h_i is the initial depth, t is the time in seconds, and a, b, and k are fitting constants. The creep rate is then calculated using the slope of the creep curve, found using equation (8) as shown in Fig. S3.8. The results are reported for 10 mN and 20 mN loading rates, but again only the data from the 20 mN loading rate tests should be considered. In all cases, the creep rate increases with temperature, as expected.

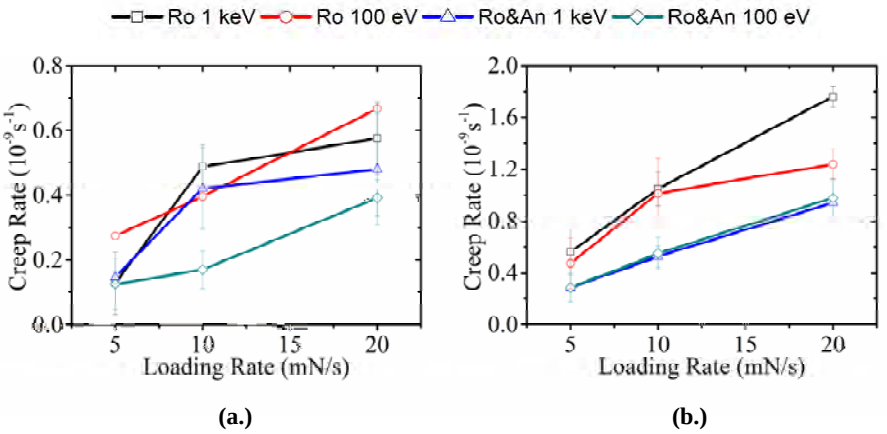

Figure S3.8: Creep rate as a function of loading rate at (a.) 250°C (b.) 450°C. Creep rate is generally higher in the case of rolled Zr and increases with microstructure.

The rolled 1 keV and 100 eV irradiated Zr samples exhibited higher creep rates, when compared to the other samples, which were nearly invariable with manufacturing process and irradiation. The stress exponent is calculated using the following relation Gan and Tomar (2010)

$$n = \frac{\ln(d\dot{\varepsilon})}{\ln(d\sigma)}, \tag{9}$$

where $\dot{\varepsilon}$ is the creep strain rate and σ is the stress. The indentation strain rate here is given by

$$\dot{\varepsilon} = \frac{dh}{dt}\frac{1}{h(t)}, \tag{10}$$

where h is the indentation depth and t is time and the stress is given by

$$\sigma = \frac{P}{A}, \tag{11}$$

where *P* is the constant load applied during the dwell period and *A* is the area function of the indenter. The results of this calculation as a function of loading rate are shown in Fig. S3.9.

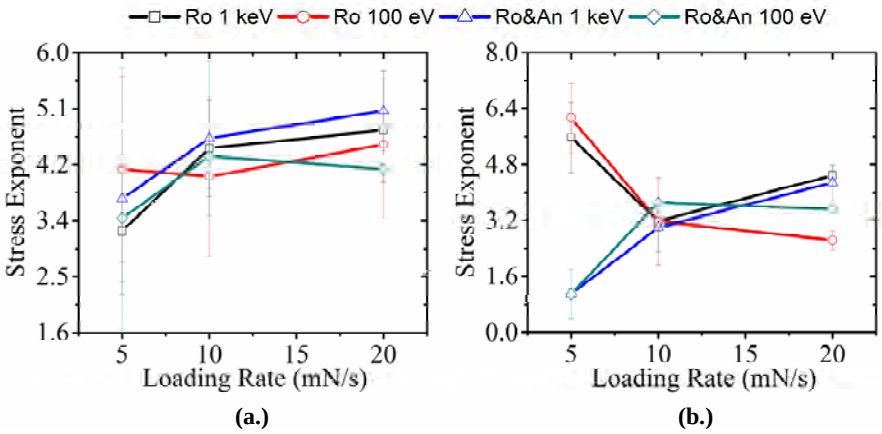

Figure S3.9: Stress Exponent as a function of loading rate at (a.) 250°C (b.) 450°C. Stress exponent, in nearly all cases, decreases with temperature. Aside from this, there are no discernable trends. Creep activation energy is calculated using the following relation, for two given temperatures

$$Q = \frac{R \ln\frac{\dot{\varepsilon}_1}{\dot{\varepsilon}_2}}{\frac{1}{T_2} - \frac{1}{T_1}}, \tag{12}$$

where R is the universal gas constant, $\dot{\varepsilon}$ is the strain rate, and T is the temperature, where the subscripts 1 and 2 correspond to temperatures 1 and 2. In the case of using data from more than two temperatures, the creep activation energy can be found by plotting the strain rate, as a function of the reciprocal temperature, performing a curve fitting, and observing the slope. The activation energy is then found using a simple conversion, using the universal gas constant. The results of this calculation are shown in Table 1.

	Sample	**Activation Energy (J/mol)**	
		Rolled	Rolled & Annealed
10 mN/s	1 keV	9439.03	9292.685
	100 eV	9495.028	9595.865
20 mN/s	1 keV	7917.355	8491.51
	100 eV	7508.009	7370.454
	Unirradiated	5333.70	10973.0

Table 1: Summary of creep activation energy at 10 mN/s and 20 mN/s. Activation volume depends solely on microstructure. Irradiation effects are negligible.

In all cases, the activation energy for rolled Zr samples was higher than rolled and annealed samples. In the case of the effect of irradiation on activation energy, we observe the opposite

trends between rolled Zr and rolled and annealed Zr. For example, of the rolled Zr samples, the 100 eV irradiated ones have the highest activation energy, while of the rolled and annealed Zr samples, the 100 eV samples have lowest activation energy. The thermal activation volume Gan and Tomar (2010) is given by

$$V^* = k_B T \left. \frac{d \ln \dot{\varepsilon}}{d\sigma} \right|_{\varepsilon, T}, \tag{13}$$

where k_B is the Boltzmann constant, T is the temperature, $\dot{\varepsilon}$ is the strain rate, and σ is the stress. The result of this calculation is shown in Fig. S3.10.

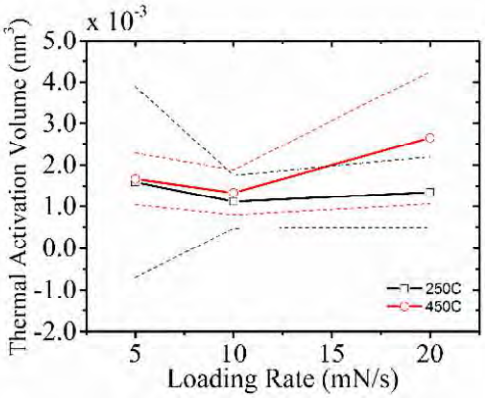

Figure S3.10: Thermal activation volume as a function of loading rate. Thermal activation volume increases with temperature. Here, major lines here represents the average value of thermal activation volume among the three different sample variants, while the error lines here indicate the range of values.

The major lines here represents the average value of thermal activation volume among the three different sample variants, while the error lines here indicate the range of values. The thermal activation volume increases with temperature in nearly all cases, as expected. The rate on increase of thermal activation volume with temperature varies in each case and no discernable trends can be found.

Indentation Stress-Strain Curves

Indentation stress strain curves were calculated for each sample using the loading portion of the load-depth data obtained using nanoindentation. These properties are calculated using the loading portion of the load-depth curve. The indentation stress is given simply by

$$\sigma_{indentation} = \frac{P}{A} = p_m, \tag{14}$$

where P is the load and A is the area function of Berkovich indenter used. This indentation stress is a term synonymous with mean contact pressure in indentation. It should be noted, this stress in not equivalent to the axial stress obtained from a uniaxial tension or compression testing. The indentation plastic strain is more difficult to obtain. In fact, using a Berkovich indenter tip, the strain cannot be directly obtained and instead an approximation is used, based on a constant indentation strain rate. This strain rate is determined using equation (10). While the strain rate is not a controlled parameter during indentation and is thus non-constant, during the loading period,

there is very little variation in strain rate and thus a constant strain rate can be assumed for each sample variation. Using this constant plastic strain rate, the plastic strain at the corresponding loads can be extracted, while the elastic strain is simply found using Hooke's Law and the nanoindentation derived values of Young's modulus. These indentation stress-strain curves are shown in Fig. S3.11.

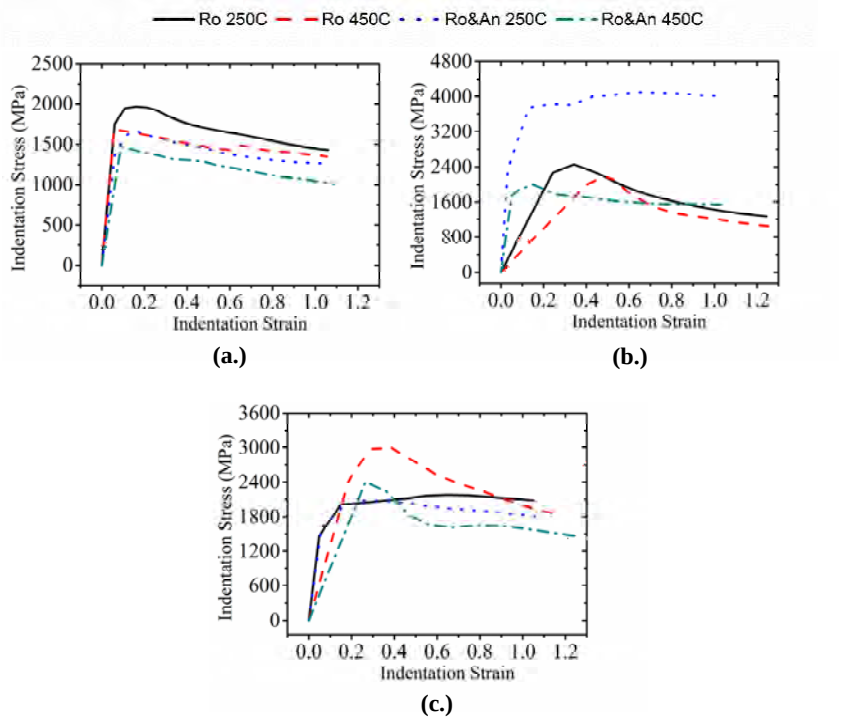

Figure S3.11: Indentation Stress-Strain Curves for Zirconium (a.) Unirradiated (b.) 1 keV (c.) 100 eV. Irradiation hardening is present in all cases and post-yield softening is observed in most cases.

We observe that the indentation yield strength of the irradiated samples each increase relative to the unirradiated ones. In most cases, the yield strength decreases with temperature, except in the case of 100 eV irradiation for rolled and rolled and annealed Zr. Most curves show some amount of softening after the initial yielding.

Anand Viscoplastic Model

In addition to the use of the Power Law creep model, the Anand viscoplastic model was used to characterize the high temperature behavior of the Zr samples. The creep plastic strain rate in the Anand model Chen et al. (2005; Zhang et al. (2009) is given by

$$\dot{\varepsilon}^p = A\, exp\left(-\frac{Q}{RT}\right)\left[sinh\left(\zeta\frac{\tilde{\sigma}}{s}\right)\right]^{1/m}, \qquad (15)$$

where A, ζ, and m are constants, Q is the activation energy, R is the universal gas constant, $\tilde{\sigma}$ is the saturation stress, and s is a state variable. The Anand parameters are found using a series of curve fittings and are summarized in Table 2.

Parameter	Rolled 1 keV	Rolled 100 eV	Rolled 100 eV (700ºC)	Rolled & Annealed 1 keV	Rolled & Annealed 100 eV	Rolled & Annealed 100 eV (700ºC)
A (1/s)	6.3E+05	9.6E+04	3.0E+06	5.0E+05	2.9E+03	5.0E+05
Q (J/mol)	5.3E+04	7.6E+03	4.0E+04	5.0E+04	7.5E+03	5.0E+04
m	0.99	0.23	1.01	1.04	0.56	0.87
n	-0.97	-0.94	-0.94	-0.92	-0.95	-0.91
a	49.15	7.75	5.18	8.99	29.5	26.3
ζ	1.00	1.00	1.00	1.00	1.00	1.00
ŝ (MPa)	300	1.9E+04	3.6E+03	2.2E+03	7.3E+03	2.0E+04
h_0 (MPa)	1.5E+10	4.1E+09	1.4E+12	5.2E+10	3.1E+10	2.5E+10

Table 2: Anand parameters for rolled and rolled and annealed samples.

A comparison between the indentation stress-strain responses found using the method detailed in the previous section and the Anand viscoplastic model are shown in Fig. S3.12. The response dictated by the Anand model is represented by the dotted lines. These stress-strain curves below are at a strain rate of between 0.1 and 0.2 s^{-1}.

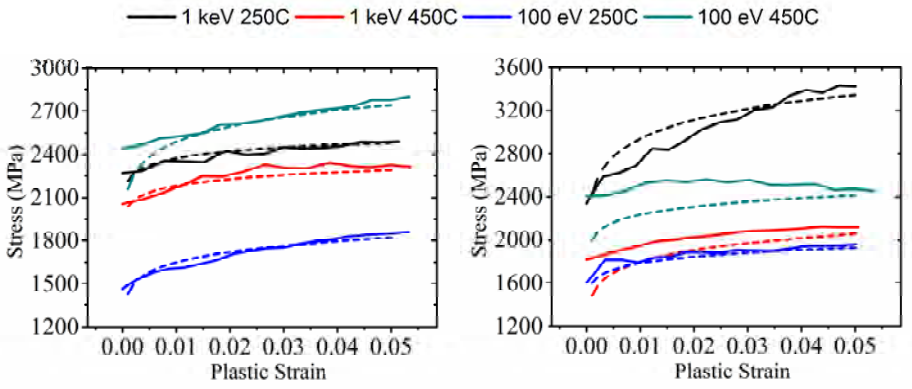

Figure S3.12: Comparison of Anand model to indentation stress-strain for initial plastic deformation of (a.) Rolled Zr (b.) Rolled & Annealed Zr. The dashed lines represent the response from the Anand model, while the solid lines represent the experimental data. The model accurately represents the initial plastic response in most cases.

We can observe that the Anand model does a reasonable job of characterizing the immediate response of the rolled Zr samples, but is not as accurate in the case of rolled and annealed Zr. There are a number of faults associated with the use of the Anand viscoplastic model for this purpose, which will be later detailed in the discussion section.

Discussion

A summary of the results of the mechanical and creep property analysis of irradiated Zr in comparison to unirradiated Zr is shown in Table 3.

		1 keV		**100 eV**	
		Magnitude	Temperature Dependence	Magnitude	Temperature Dependence
Reduced Modulus	Rolled	Moderate Decrease	Significant Decrease	Negligible Change	Significant Increase
	Rolled & Annealed	Significant Increase	Significant Increase	Negligible Change	Significant Increase
Hardness	Rolled	Moderate Increase	Significant Increase	Moderate Increase	Negligible Change
	Rolled & Annealed	Significant Increase	Significant Increase	Moderate Increase	Negligible Change
Yield Strength	Rolled	Moderate Increase	Negligible Change	Moderate Increase	Significant Increase
	Rolled & Annealed	Moderate Increase	Significant Increase	Moderate Increase	Negligible Change
Creep Rate	Rolled	Moderate Increase	Significant Increase	Moderate Increase	Negligible Change
	Rolled & Annealed	Moderate Increase	Negligible Change	Moderate Increase	Moderate Increase
Stress Exponent	Rolled	Significant Decrease	Significant Decrease	Significant Decrease	Negligible Change
	Rolled & Annealed	Significant Decrease	Significant Decrease	Significant Decrease	Significant Decrease
Activation Energy	Rolled	Significant Increase	N/A	Significant Increase	N/A
	Rolled & Annealed	Moderate Decrease	N/A	Significant Decrease	N/A
Thermal Activation Volume	Rolled	Significant Increase	Significant Increase	Moderate Increase	Negligible Change
	Rolled & Annealed	Significant Decrease	Negligible Change (Reverse)	Significant Decrease	Negligible Change

Table 3: Summary of mechanical and creep properties of irradiated Zr in comparison to unirradiated Zr.

In all cases, the effect of temperature on the mechanical and creep properties is as expected,

excluding a few outlying data points. As temperature increases, the material softens and flow stress decreases, leading to reduced modulus decreasing, hardness decreasing, yield strength decreasing, creep rate increasing, stress exponent decreasing, and thermal activation volume increasing. With respect to irradiation and manufacturing process, reduced modulus and hardness exhibit similar trends. 100 eV irradiated samples exhibit invariability with respect to manufacturing process, while 1 keV irradiated samples exhibit opposite trends with respect to manufacturing process. For example, in the case of rolled Zr, reduced modulus of 1 keV irradiated samples decrease relative to unirradiated samples. The opposite is true for rolled and annealed Zr. The difference in peak reduced modulus between the rolled and rolled and annealed Zr samples can be explained by the increased ductility due to the annealing process. This effect, however, is not as significant as the effect of radiation damage. Hardness and indentation yield strength follow very similar trends with respect to one another as well. Both properties increase when subjected to radiation, in comparison to their unirradiated counterparts. The accepted explanation for the increase in hardness and yield strength is the mechanism of vacancy agglomerates. Essentially, vacancies are formed due to atomic displacements in the presence of radiation. These vacancies coalesce and bond to one another, which creates a significant obstacle to the motion of dislocations due to external stresses. At higher temperatures, not only does flow stress decrease, but these vacancies become more mobile and lead to an decrease in yield strength and hardness, in most cases. We observe the opposite trend in the case of indentation yield strength in the 100 eV irradiated samples, which is a phenomena known as the yield strength anomaly and is commonly observed in precipitation hardening superalloys. These results could be a consequence of the somewhat subjective method for determining the yield strength based on indentation derived stress-strain curves. Assuming this is not the case, we observe this effect solely at lower irradiation energies. Dpa is proportional to average irradiation energy and thus, we can surmise that at lower irradiation energies, the void density is lower in comparison to higher irradiation energies, based on our understanding of the relationship between void density and dpa. Additionally, void radius increases significantly with temperature, as the void density decreases S. D. Harkness and Li (1971). The result of the two mechanisms means that the voids present in the 100 eV samples at high temperature should be very large and relatively immobile in comparison to the smaller voids. This could explain the increase in indentation yield strength with temperature in these cases.

The creep rate of the rolled and annealed samples all increase relative to their unirradiated counterparts. Of these samples, we see an increase in temperature dependence only in the 100 eV irradiated samples. The creep rate for the rolled samples also tends to increase relative to the unirradiated samples. The increase in creep rate is likely a result of the vacancy growth that occurs during radiation. Under increasing load, these vacancies act to strengthen the material, as they are obstacles to dislocation motion. However, under constant load, like in thermal creep testing conditions, the increased mobility of these vacancies, relative to the material itself, leads to greater creep strain rates, in comparison to unirradiated material. Greater irradiation energy thus leads to greater creep strain rates, which is the trend we observe in our data. This phenomena also explains the decrease in stress exponent in the case of the irradiated samples, in comparison to the unirradiated ones. With higher stress exponent, the stress required to produce a given plastic strain rate is lower in comparison to a lower stress exponent. The activation energy of creep appears to be

solely dependent on manufacturing process, as the irradiated samples exhibit similar values for this parameter, while the unirradiated samples form the maxima and minima of the set. The annealing process acts to increase the material's immediate resistance to high temperature effects and creep, which supports the result of high activation energy in the rolled and annealed samples. We observe the same trend in the case of thermal activation volume. The increase in thermal activation volume of rolled and annealed Zr suggests a higher deformation work is required for dislocation motion. This also supports the creep rate findings in relation to rolled and rolled and annealed Zr. The effect of manufacturing process on creep properties, before irradiation, are very significant. However, after irradiation, the creep response of all irradiated materials are similar, although creep is slightly more significant in rolled Zr samples. This is likely due to the swelling and irradiation creep that occurs prior to testing, during the irradiation process. The thermal creep deformation, while additive in respect to the irradiation creep deformation and swelling, is relatively insignificant. This explains the vastly different creep response of the irradiated Zr in comparison to the unirradiated Zr.

Strictly speaking, stress-strain curves cannot be produced using pyramidal indentation. Only spherical indentation can be used for this purpose due to the inherent geometric relationships present in an indenter of such geometry. The indentation stress-strain curves produced in this work are not to be interpreted strictly as the stress-strain response of the irradiated Zr samples. The indentation stress, also known as mean contact pressure, in this case is significantly higher than the actual stress exhibited in the loading conditions. Any reference to indentation yield strength carries the same consequence. While the magnitude of these stress values cannot be directly compared to actual stress experienced by the material, we can observe important trends and characteristics relative to each sample due to the proportionality between the reported stress values and the actual stresses experience by the material. Additionally, the strain values reported are based on a simple approximation, under the assumption that the plastic strain rate in the portion of the loading load-depth curve utilized is relatively constant. While this is a valid assumption, the result is, again, only an approximation.

Traditionally, the Anand viscoplastic model has been used to characterize the high temperature response of solders and similar materials Zhang et al. (2009). This model, as well as similar ones have been used to characterize the stress-strain response of metals Anand (1982; Brown et al. (1989; M. Kothari and Anand (1998). The use of such a model is very convenient for implementation in simulations, such as finite element analysis. The Anand viscoplastic model in particularly is already implemented into ANSYS and ABAQUS. Thus, this model was utilized in an attempt to capture the high temperature indentation stress-strain response of the Zr samples. Initial attempts to model the full plastic response of the samples proved unfruitful, but a decent approximation can be made when considering only the initial plastic response. The fault in this case is due to the nature of the Anand model. If, for example, the 250ºC and 450ºC indentation stress-strain response of a given sample are of the same shape, just with different yield strength, then the Anand model can easily characterize the response. However, if these two curves differ in shape or the elastic modulus is significantly different, the Anand model can, at best, only accurately characterize a single curve, leading to an error in the other curve. The complexity of the curve also factors into the ability of the model to characterize the response, but the most significant source of error is the variation between curves at

different temperatures. The Anand model requires an idealized relationship between stress and temperature for a given sample variant, which in most cases, is not realistic. If studying immediate plasticity effects, the model can be utilized to reasonable accuracy as shown.

Conclusion

The mechanical and creep properties of rolled and rolled and annealed Zr are investigated, in addition to the indentation stress-strain response of these materials. The mechanical properties (reduced modulus, hardness, indentation yield strength) of irradiated Zr all increase relative to that of the unirradiated Zr samples. In most cases, the rolled samples exhibit higher reduced modulus, hardness, and indentation yield strength. While the manufacturing process (rolling or rolling and annealing) is significant in determining these properties, the effect of irradiation damage is more significant. Not only this, but the combination of irradiation energy and manufacturing process yielded a unique mechanical response. Thus, it is crucial to consider both these effects in the design of nuclear fuel cladding, where these materials are typically used.

The creep properties (creep rate, stress exponent, activation energy, thermal activation volume), unlike the mechanical properties appear to be highly dependent on manufacturing process. The irradiation process, regardless of irradiation energy, invokes a similar creep response. The main consideration in regards to creep behavior is thus, the manufacturing process. While the irradiation energy should also be considered, its effect is much less significant.

Part II: Nanomechanical Characterization and Stress Mapping of Irradiated Zirconium-alloys in a Corrosive Environment Using Raman Spectroscopy

II.1: Sample Preparation for Corrosion

One hour prior to testing, all samples were polished with SiC paper. Immediately before electrolyte submersion, the samples were degreased with a solvent and rinsed with distilled water. These methods are in accordance with the ASTM G5. Prior to mechanical testing, samples were again degreased with a solvent and rinsed with distilled water. No further polishing are performed to ensure corrosion effects are accurately represented.

Experimental Procedure and Preliminary Results

Phase 1: Electrochemical Corrosion

Zircaloy samples of dimensions 15 mm x 5 mm x 1 mm will be subjected to electrochemical corrosion in H_2O, NaOH, CO_2, and LiOH electrolyte solutions. A 1 L Gamry Multiport Corrosion Cell, as well as a Gamry Interface 1000, as shown in Fig. S3.13 is utilized for this analysis.

Figure S3.13: Gamry 1 L Multiport Corrosion Cell with Interface 1000 potentiostat control (not shown).

A graphite counter electrode and a Ag/AgCl reference electrode is utilized with the corrosion cell. Testing is in accordance with the ASTM G5 and G59, with the exception of the sample specifications. Rather than a cylindrical, threaded sample, a plate sample is utilized to later accommodate mechanical testing. Samples are mounted to the sample holder using an epoxy. The electrical potential applied between the working electrode (specimen) and the reference electrode is measured over one week periods and is shown in below.

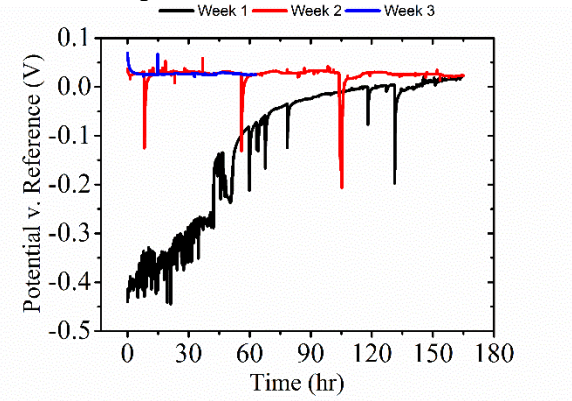

Figure S3.14: Corrosion potential measured from Zircaloy-4 sample in 1 M NaCl solution at room temperature in one week periods.

Using the polarization resistance technique, the corrosion rate of each sample is obtained. The

polarization resistance is given by

$$R_p = \left.\frac{\partial \Delta E}{\partial i}\right|_{i=0,\ \frac{dE}{dt}\to 0}, \tag{16}$$

where i is the current density and ΔE is the corrosion potential. The corrosion current density is related to the polarization resistance by the Stern-Geary coefficient, B and is given as

$$i_{corr} = 10^6 \frac{B}{R_p}, \tag{17}$$

where R_p is in ohm-cm^2, i_{corr} is in μA/cm^2, and B is in V. The Stern-Geary coefficient is given by

$$B = \frac{b_a b_c}{2.303(b_a + b_c)}, \tag{18}$$

where b_a and b_c are the anodic and cathodic Tafel slopes. Finally, the corrosion rate is then given as

$$CR = 3.27 \times 10^{-3} \frac{i_{corr} EW}{\rho}, \tag{19}$$

where EW is the equivalent weight in g and ρ is the density of the corroding material in g/cm^3. Tafel scans are performed after each one week period and are shown below.

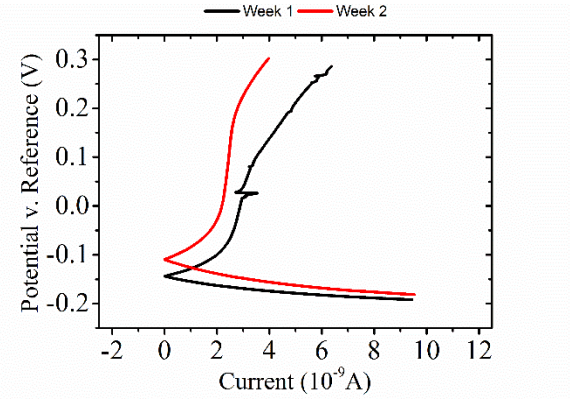

Figure S3.15: Tafel scans recorded at the end of each week of 1 M NaCl electrolyte exposure at room temperature.

From these scans, the Tafel constants/slopes are determined and later used to determine the corrosion rate. The constants for the respective scans are summarized below.

	Anodic Tafel Slope (V/dec)	Cathodic Tafel Slope (V/dec)
Week 1	918.3E-3	61.20E-3
Week 2	2.225	95.90E-3

Table 4: Summary of Tafel slopes determined from Tafel scans at the end of each week of NaCl electrolyte exposure at room temperature.

Finally, using these Tafel constants and the polarization resistance, we can determine the corrosion rates in each respective case. The polarization resistance curves are shown below.

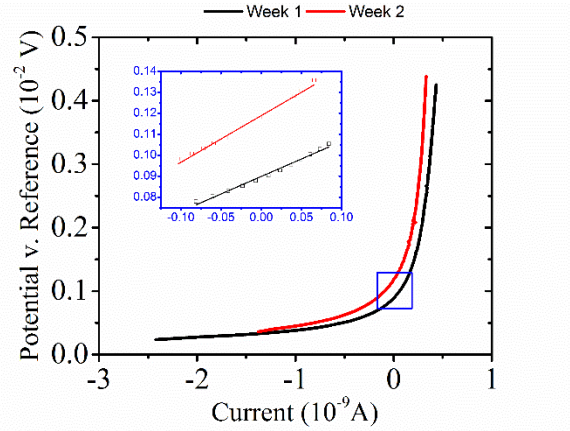

Figure S3.16: Polarization resistance at the end of each week of 1 M NaCl electrolyte exposure at room temperature.

	Corrosion Rate (mpy)
Week 1	8.282E-3
Week 2	9.902E-3

Table 5: Measured corrosion rates determined from polarization resistance at the end of each week of NaCl electrolyte exposure at room temperature.

This procedure will be later repeated and corrosion rate will be determined for Zircaloy-2 and Zircaloy-4 samples in 0.01 M, 0.1 M, and 1 M H_2O, NaOH, H_2CO_3, and LiOH electrolyte solutions at room temperature, 250°C, and 450°C. These samples will be subjected to electrochemical corrosion for increasing periods of time in each of the electrolyte solutions previously mentioned.

An electrochemical corrosion reaction under kinetic control obeys Eq. 29, the Tafel equation

$$I = I_0 \exp(2.303(E - E_0)/\beta) \quad (20)$$

In a corrosion system, we have two opposing reactions: anodic and cathodic. The Tafel equations for the anodic and cathodic reactions in a corrosion system can be combined to generate the Butler-Volmer equation (Eq. 30).

$$I = I_{corr}[\exp\left(\frac{2.303\,(E-E_{corr})}{\beta_a}\right) - \exp\left(\frac{2.303\,(E-E_{corr})}{\beta_c}\right) \quad (21)$$

Where I is the measured current from the cell in amperes, I_{corr} is the corrosion current in amperes, E is the electrode potential, E_{corr} is the corrosion potential in volts, β_a is the anodic β Tafel constant in volts/decade, and β_c is the cathodic β Tafel constant in volts/decade. Most modern corrosion tests perform a more sophisticated numerical fit to the Butler-Volmer equation. The measured data are fit to Eq. 30 by adjusting the values of E_{corr}, I_{corr}, β_a, and β_c.

Polarization resistance model

For the polarization resistance model, we simplified Eq. 30 further more by restricting the to be very near to E_{corr}. Then, the current-versus-voltage curve approximates a straight line. The

slope is, therefore, called the polarization resistance, R_p. The Stern-Geary equation for polarization resistance is

$$I_{corr} = \frac{1}{R_p} \frac{\beta_a \beta_c}{2.303\,(\beta_a + \beta_c)} \tag{22}$$

In a polarization resistance experiment, you record a curve of current versus voltage as the cell voltage is swept over a small range of potential that is very near to E_{corr}. In experiments a numerical fit of the curve yields a value for the polarization resistance, R_p.

Data analysis

So far, we have performed two corrosion tests. One is unirradiated zircaloy sample, the otherone is irradiated zircaloy sample. From compare their corrosion test data, we can find some clue about how does the radiation affect zircaloy corrosion resistence. In Fig. 3.17, we showed the corrosion rate of unirradiated sample in both palarization resistance model and Tafel model.

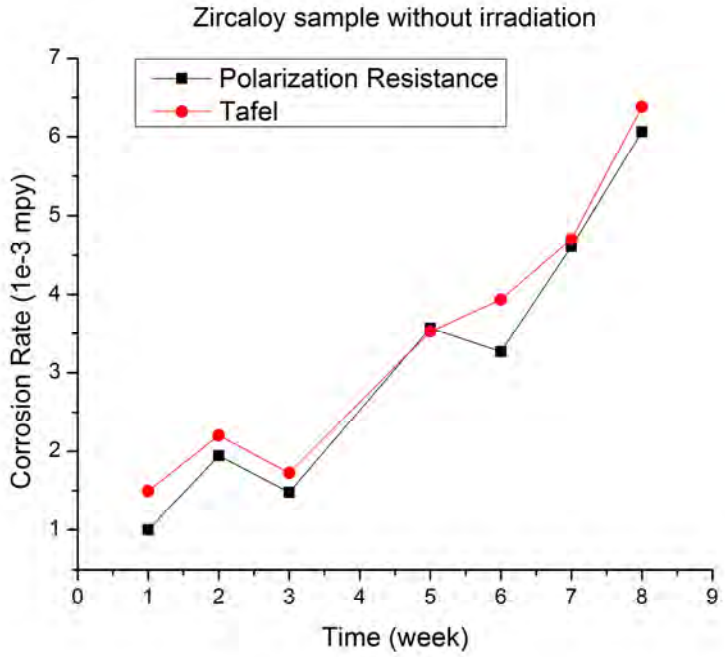

Figure3.17. corrosion rate of unirradiated sample

In Fig. 3.18, we showed the corrosion rate of irradiated sample in both palarization resistance model and Tafel model.

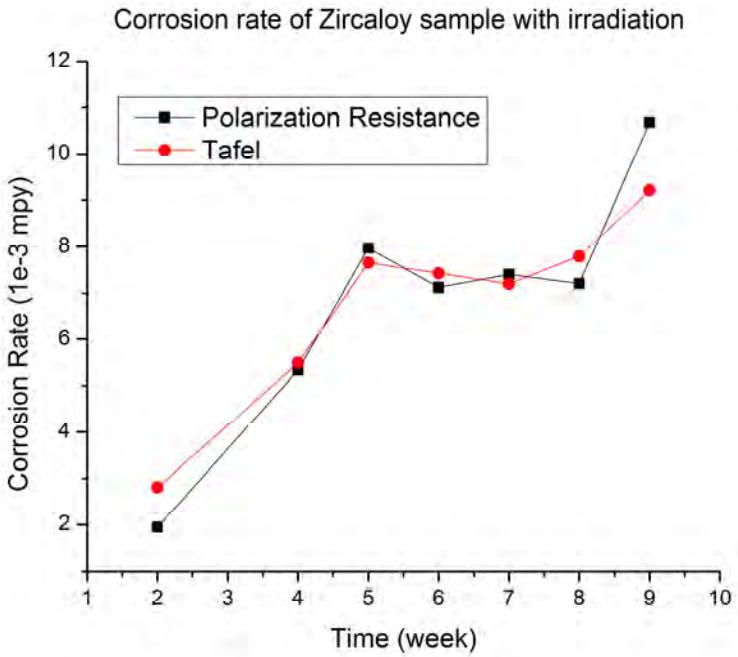

Figure3.18. corrosion rate of irradiated sample

In Fig.3.19, we compared the corrosion rate of unirradiated and irradiated samples in both palarization resistance model and Tafel model.

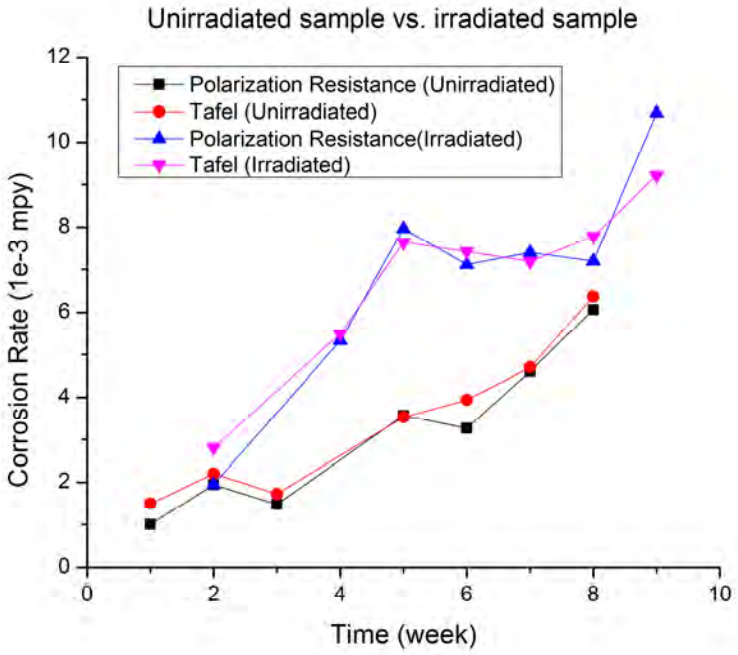

Figure3.19. Comparison of unirradiated and irradiated samples

It's obvious that zircaloy samples after irradiation will have a higher corrosion rate. Which consistents with common sense and our expection, radiation will reduce the material's corrosion

resistance.

II.2: Sample Preparation for Mechanical Testing and Raman Mapping

Sample Preparation

Prior to mechanical testing each sample is degreased with a solvent and rinsed with deionized water. The samples are then mounted to the indentation stage using epoxy for loading. For the purpose of initial tests, the sample is mounted flat against the stage along the thickness of the sample. The next stage of testing will utilize a bending configuration and an 8.8 x 2 x 1 mm sample with a center crack. The importance of this configuration is further explained later.

Experimental Procedure

The MicroMaterials NanoTest, as shown in Fig. S3.3 is utilized to apply load to the samples, using a flat-punch indenter. For the purpose of initial tests, the sample is mounted flat against the stage along the thickness of the sample and the load is applied on the opposite side, in a compression configuration. The next stage of testing will utilize a bending configuration and an 8.8 x 2 x 1 mm sample with a center crack. The importance of this configuration is further explained later. The loading rates utilized in each case are 2 mN/s, 5 mN/s, 10 mN/s, and 20 mN/s with maximum loadings of 50 mN, 100 mN, 200 mN, and 400 mN, respectively. Load-displacement curves for a non-corroded Zircaloy-4 sample and a corroded Zircaloy-4 sample (2.5 weeks exposure to 1 M NaCl at room temperature) are shown below.

The as-received Zircaloy-4 plate has been cut into small pieces and been performed three-point bending tests. According to ration of length, width and thickness in the ASTM E 1290-08 Standard, the dimension of sample is 8.8mm*2.0mm*1.0mm. The crack locates in the middle of one edge with dimension of 1.0mm*0.2mm. After the cutting, the samples were sent to mechanical polishing to reduce the roughness of the surface. As metal does not have Raman Effect, in order to use the Raman spectroscopy to measure the stress of sample, Raman sensitive material needs to be introduce into the measurement. So after mechanical polishing, the samples were coated with silicon on the one side of the surface with dimension of 8.8mm*2.0mm. The thickness of the coated silicon layer is 1um. The dimension of the sample is shown in the Fig. S3.20 (a), and the real photo of coating sample is shown in the Fig. S3.20 (b). In order to analysis the microstructure effect of the material, the SEM figure of the surface has been taken and shown in the Fig. S3.21.

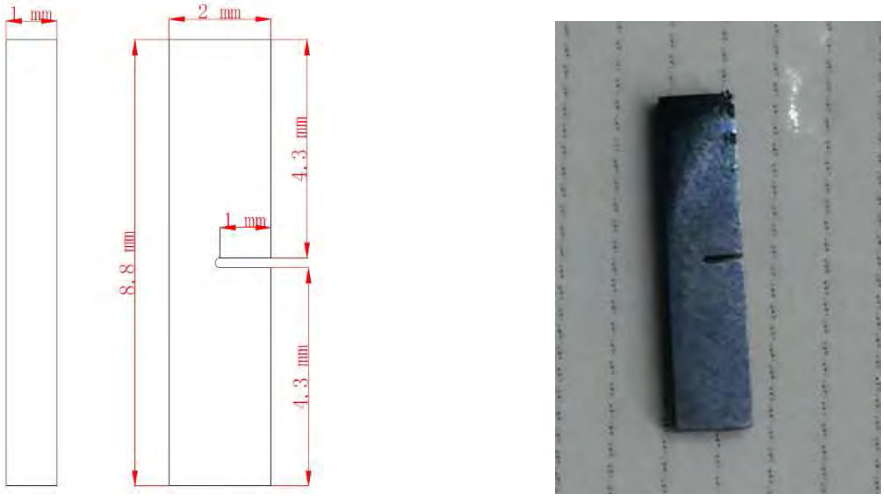

(a) (b)

Figure S3.20. (a) Dimension of the Zircaloy sample; (b) photo of coated Zircaloy sample with 1 um silicon.

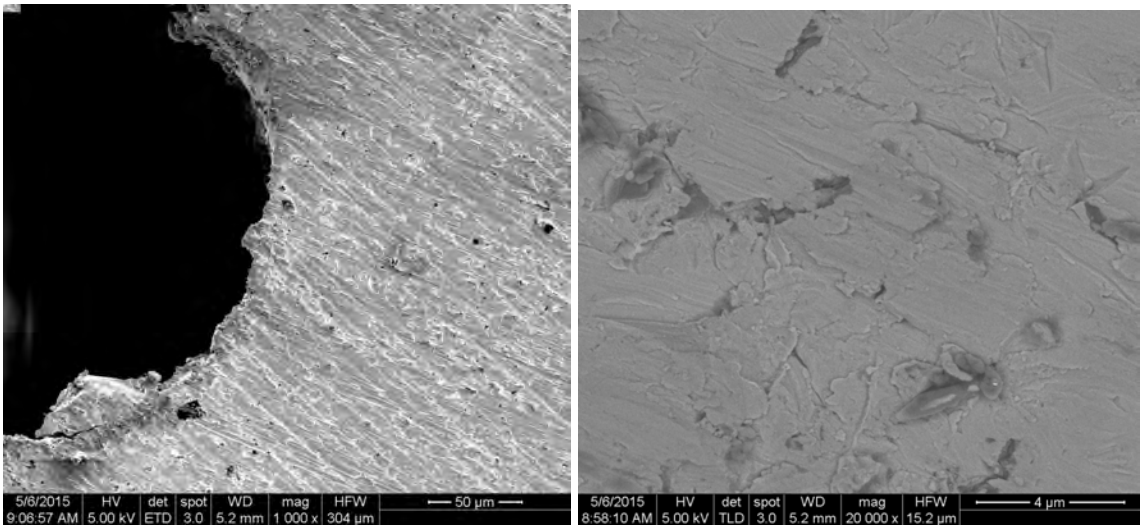

Figure S3.21. SEM figures of the Zircaloy sample surface

II.3: Experimental Setup

All tests were performed using a multi-module mechanical tester (Micro Materials Ltd., UK). The load ranges from 0.1 mN to 500 mN, with the accuracy of better than 0.1 mN. The Raman laser used in this research is 514.5 nm Ar+ laser (Modu-Laser Inc, UT). The laser was directed to the sample using single mode fiber (SMF), and then focused using an objective. The objective in is the long working distance (20.5 mm) objective with the magnification of 50X (Mitutoyo, NO. 46-399). The back-scattered laser was collected by the same objective and sent to the spectrometer (Acton SP2500, Princeton Instruments Inc., NJ). The motorized linear stage (MAX 300, Thorlabs, NJ, USA) that is controlled by a 3-Channel controller (BSC 203, Thorlabs, NJ, USA) can move in 3 directions with the minimum incremental movement of 60 nm. The move range of the stage in 3 direction is 4.0 mm. The objective, dichromic mirror and collimator are mounted on the stage as the Figure S3.22 shows.

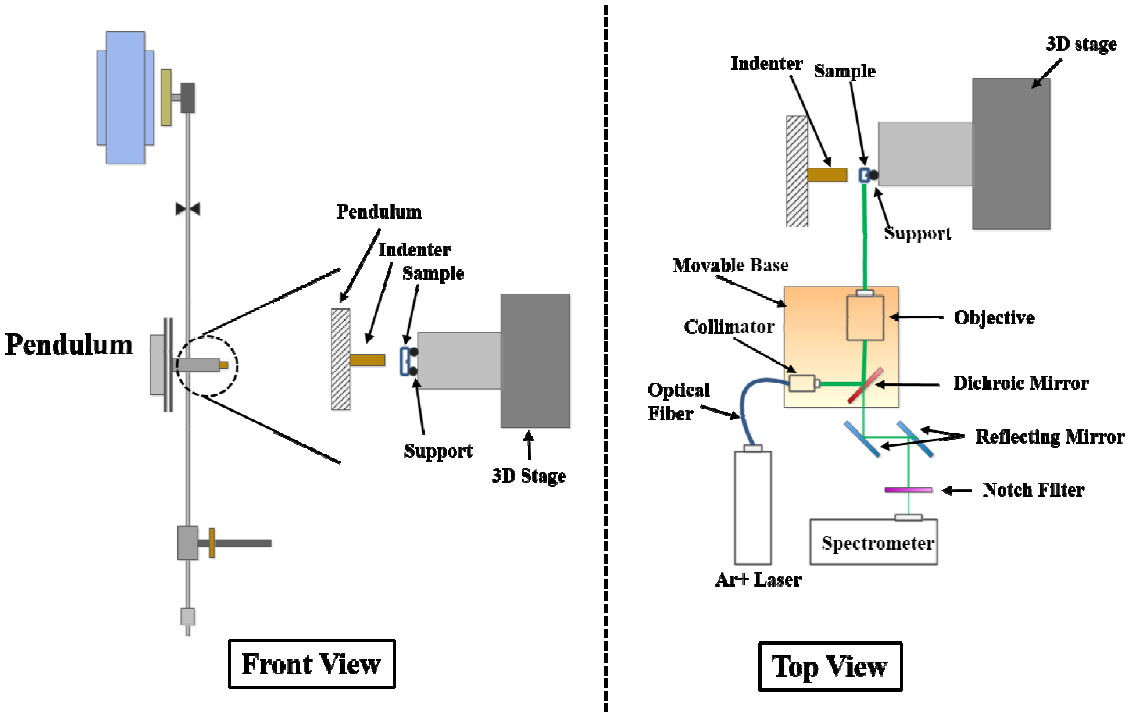

Figure S3.22. Three-point Bending Test with Nanomechanical Raman Spectroscopy

The overall procedure of experiments are listed as the following.

(1) Heat the sample and the indenter to target temperature and keep inactive for thermal stability;

(2) Scan the area of crack tip using Raman nanomechanical spectroscopy while the three points bending tests on the samples with an initial crack to predict crack tip temperature field. The local temperature is calculated through the relation between temperature and Raman shift;

(3) Separate the Raman shift caused by the temperature and strain on the sample;

(4) Mapping the temperature filed around the crack tip.

4. Experimental Results

Indentation Curve

Figure S3.23 represents the typical load displacement curve for a three-point bending experiment done at room temperature with 400 mN maximum load. In this case, the sample is loaded up to the maximum load, the maximum load is hold for Raman scanning and then unloading happens.

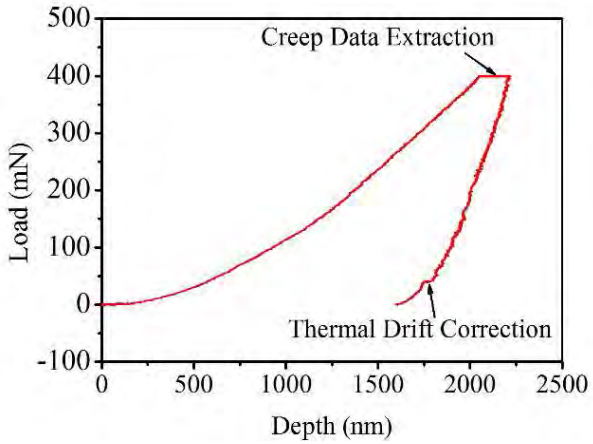

Figure S3.23. Typical Load- Displacement Curve of the three-point bending test

Separate Raman Shift Caused by Temperature and Strain

The charge-coupled device (CCD) of the Raman spectroscopy system captures Raman spectrum using discretized pixels. More pixels of the CCD will result in more accurate measurement of the Raman peak. However, even with high resolution CCD cameras, this discretized capturing process introduces measurement error of the Raman peak position. The accuracy of the Raman peak detection can be improved by fitting the Raman shift spectrum. Gaussian fitting, Lorentzian fitting and Voigt fitting have been used to fit the Raman spectrum. Three fittings provide very similar results in this research which are shown in shown in the Figure S3.24.

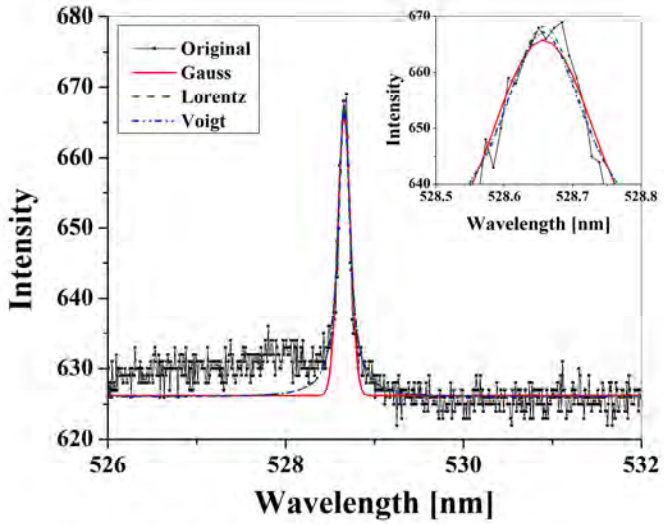

Figure S3.24. Comparison of fitting curves using Gauss, Lorentz and Voigt functions respectively

As the Raman shift is not only affected by the temperature but also the strain, it is necessary to separate the Raman shift caused by these two factors. The compressive load was applied to the samples without crack at different temperatures. At a specific temperature, the Raman shift is almost

linearly affected by mechanical strain. Temperature does not affect the linearity of the dependence of Raman shift on strain, but the slope decreases as temperature increases. The relation between the Raman shift and the compressive strain is shown in the Figure S3.25 (a) and (b).

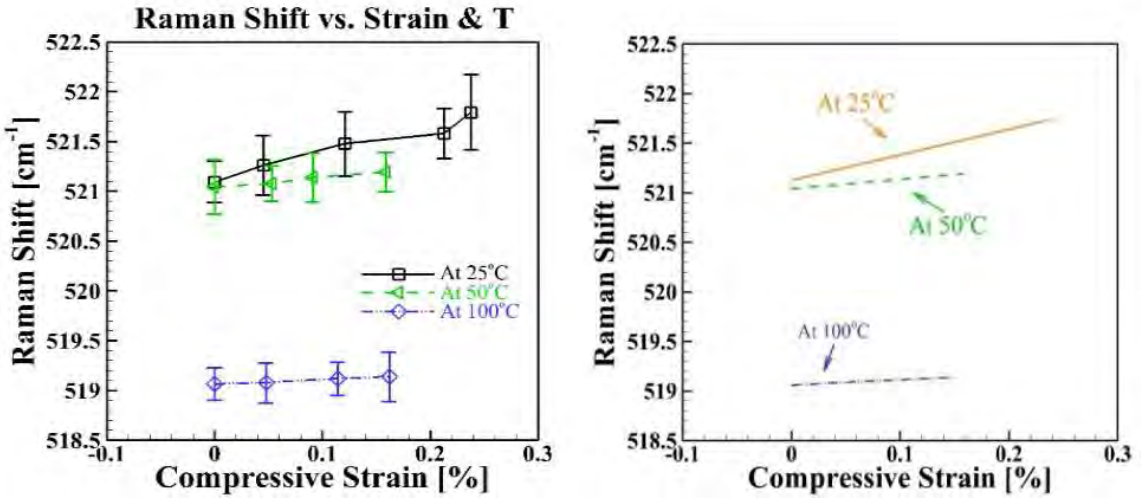

Figure S3.25. (a) Raman shift as a function of strain at different temperature; (b) Raman shift as a function of strain at different temperature, linearly fitted.

Temperature Field

The area of crack tip was scanned using Raman nanomechanical spectroscopy while the three points bending tests on the samples with an initial crack to predict the temperature field. The local temperature is calculated through the relation between temperature and Raman shift. After get the Raman spectrum is acquired at each scanning points, the stress information was integrated to generate false color images and shown in the Fig. S3.26. The test was performed without load at the temperature of 100 ℃.

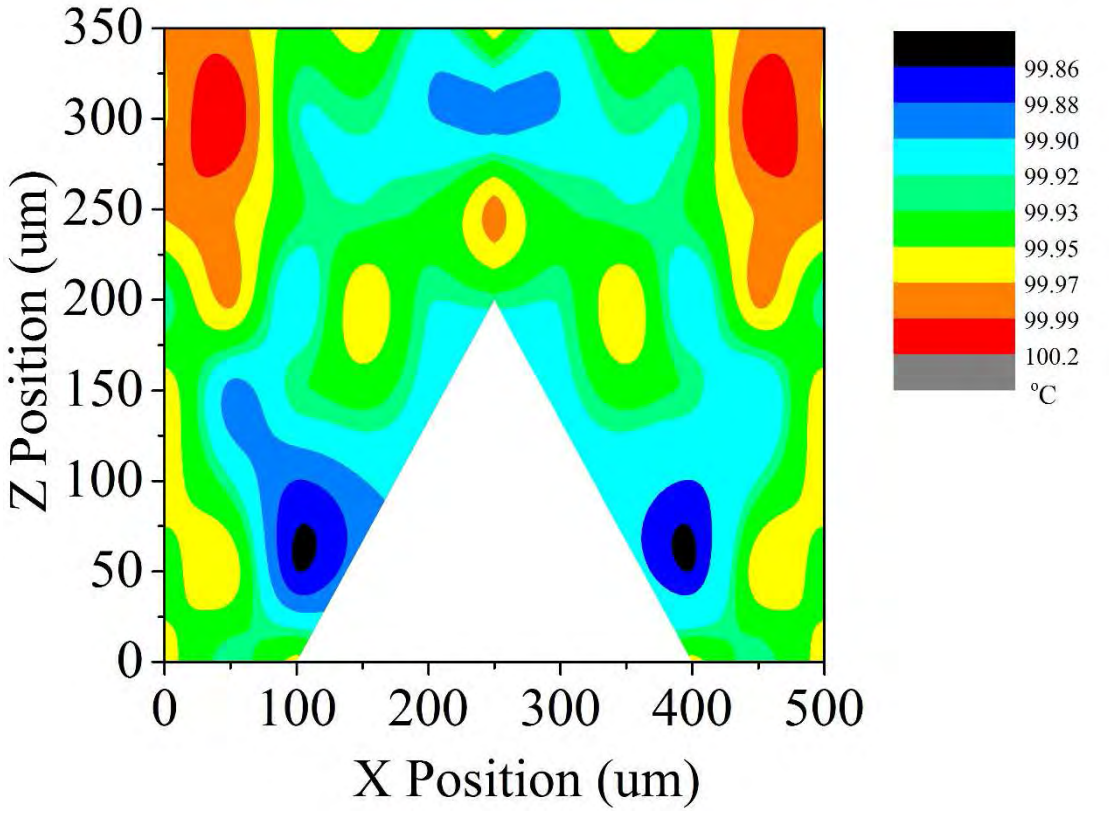

Figure S3.26. Temperature of the crack tip area without load at overall temperature of 100 ℃

The micro-Raman method is a noncontact and nondestructive method for thermal conductivity measurements. In our case, we want to use micro-Raman method to measure thermal conductivity of the irradiated Zr specimen. However, there's a thin silicon film on our specimen, which means that the film thermal conductivity, film thickness, substrate thermal conductivity and interface thermal resistance all have effects on the heat transfer process (Fig.3.27). Therefore, we need to build heat transfer model to find the relationship between the local temperature and substrate thermal conductivity.

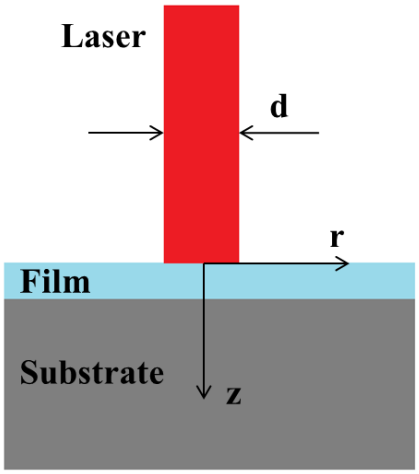

Figure 3.27. Film and substrate in cylindrical coordinate system

Assuming the film thickness is much smaller than the substrate thickness, the substrate is relatively an infinite half-plane, in this case:

$$\frac{\partial t_f(r,z)}{\partial r^2} + \frac{1}{r}\frac{\partial t_f(r,z)}{\partial r} + \frac{\partial^2 t_f(r,z)}{\partial z^2} = 0 \tag{23}$$

$$\frac{\partial t_s(r,z)}{\partial r^2} + \frac{1}{r}\frac{\partial t_s(r,z)}{\partial r} + \frac{\partial^2 t_s(r,z)}{\partial z^2} = 0 \quad . \tag{24}$$

Where t_f is the temperature in the film, and t_s is the temperature in the substrate.

Because of the continuity of the heat flow and temperature at the interface between the substrate and the film, the boundary conditions are:

$$t_f(r,z) = t_s(r,z) \qquad at \quad z = \delta \tag{25}$$

$$K_f \frac{\partial t_f(r,z)}{\partial z} = K_s \frac{\partial t_s(r,z)}{\partial z} \qquad at \quad z = \delta \tag{26}$$

$$K_f \frac{\partial t_f(r,z)}{\partial z} = -f(r) \qquad at \quad z = 0;\ 0 < r < \frac{d}{2} \tag{27}$$

$f(r)$ is the intensity of the Gaussian laser beam, $R_0 = d/2$

$$f(r) = \frac{2P}{\pi R_0^2} \exp\left(-\frac{2r^2}{R_0^2}\right) \tag{28}$$

By taking the Hankel transform of the order zero to equation (11-15), we will get transformed

equations

$$\frac{d^2T_f(\xi,z)}{dz} - \xi^2 T_f(\xi,z) = 0 \tag{29}$$

$$\frac{d^2T_s(\xi,z)}{dz} - \xi^2 T_s(\xi,z) = 0 \tag{30}$$

With boundary conditions to be:

$$T_f(\xi,\delta) = T_s(\xi,\delta) \tag{31}$$

$$K_f \frac{\partial T_f(r,\delta)}{\partial z} = K_s \frac{\partial T_s(r,\delta)}{\partial z} \tag{32}$$

$$K_f \frac{\partial t_f(r,z)}{\partial z} = -\frac{P}{2\pi} \exp\left(-\frac{R_0^2\xi^2}{8}\right) \tag{33}$$

For the transformed equations, we will have solution in following format:

$$T_f(\xi,z) = A(\xi)e^{\xi z} + B(\xi)e^{-\xi z} \tag{34}$$

$$T_s(\xi,z) = C(\xi)e^{-\xi z} \tag{35}$$

$C(\xi)$ can be found using boundary conditions, and coefficients $A(\xi)$ and $B(\xi)$ can be expressed in terms of $C(\xi)$. Then, by using the inverse Hankel transform, the temperature distribution in specimen will be found as,

$$A(\xi) = \frac{P}{2\pi} \frac{(K_f - K_s)\exp(-R_0^2\xi^2/8)}{K_f\xi[K_s - K_f + \exp(2\xi\delta)(K_f + K_s)]} \tag{36}$$

$$B(\xi) = \frac{P}{2\pi} \frac{(K_f + K_s)\exp(-R_0^2\xi^2/8)}{K_f\xi[K_s - K_f + \exp(2\xi\delta)(K_f + K_s)]} \tag{37}$$

Then we can show:

$$T_f(\xi,z) = \frac{P}{2\pi} \frac{\exp(-R_0^2\xi^2/8)}{K_f\xi[K_s - K_f + \exp(2\xi\delta)(K_f + K_s)]} \left[(K_f - K_s)e^{\xi z} + (K_f + K_s)e^{-\xi z}e^{2\xi\delta}\right] \tag{38}$$

By using inverse Hankel transform, we get

$$t_f(r,0) = \int_0^\infty \xi T_f(\xi,0) J_0(\xi r) d\xi \tag{39}$$

$J_0(\xi z)$ is the zero order Bessel function. Now we get the relation between local temperature and substrate thermal conductivity. The average temperature of the surface is

$$\tilde{t} = \frac{1}{\pi R_0^2}\int_0^{R_0} t_f(r,0)2\pi r dr$$

$$= \frac{2}{R_0^2}\int_0^{\infty} \xi T_f(\xi,0)\int_0^{R_0} J_0(\xi r)\, r dr d\xi$$

$$= \frac{2}{R_0}\int_0^{\infty} T_f(\xi,0) J_1(\xi R_0)\, d\xi$$

$$= \frac{P}{R_0 \pi k_f}\int_0^{\infty} \frac{\frac{k_f-k_s}{k_s+k_f}+\exp(\frac{z\delta}{R_0}\lambda)}{\lambda[\frac{k_s-k_f}{k_s+k_f}+\exp(\frac{z\delta}{R_0}\lambda)]} \exp(-\frac{\lambda^2}{8}) J_1(\lambda)\, d\lambda \qquad (40)$$

Where $\lambda = R_0\xi$. If the thermal conductivity of the substrate is much less than that of the film and the thickness of thin film is much less than the diameter of the laser beam, then

$$\tilde{t} = \frac{P(k_s+2k_f)[I_0(1)+I_1(1)]}{\sqrt{2\pi}R_0 e k_s k_f} \qquad (41)$$

Where $I_0(1)$ is the zero-order modified Bessel function of the first kind, and $I_1(1)$ is the first-order modified Bessel function of the first kind. Now we get the relation between local temperature and thermal conductivity of the substrate.

II.4. Temperature distribution & thermal conductivity distribution

In experiment, we use Raman scanning the crack tip while heating the sample to a target temperature (100 C) under the constant load condition (200 mN). Fig. S3.28 and Fig. S3.29 show the data gather points and temperature distribution around crack tip respectively.

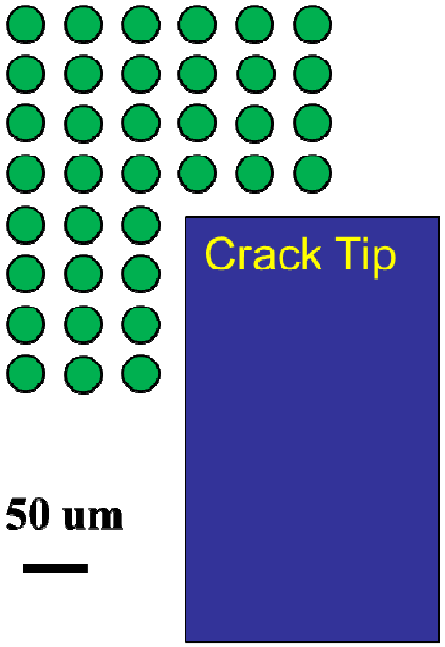

FigureS3.28. Laser scanning points (left side)

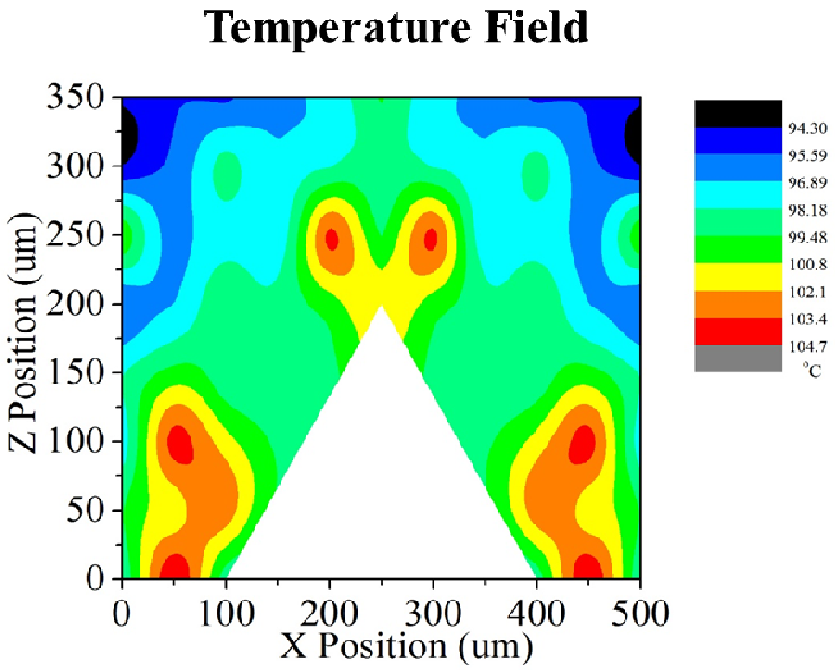

Figure S3.29. Temperature distribution

Therefore, from the equation we get in 3.4, we can calculate the substrate thermal conductivity in

each laser scanning point. At last, we get thermal conductivity field, which is showed in Fig. S3.30.

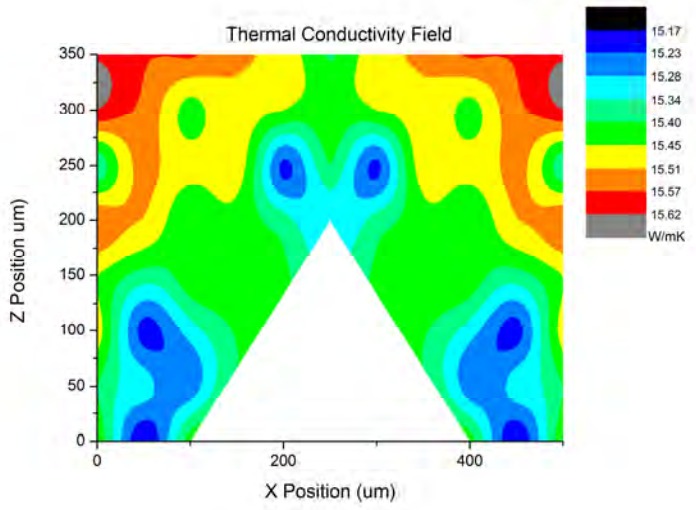

Figure S3.30. Thermal conductivity field

The following picture shows the thermal conductivity distribution of both non-irradiated and irradiated samples at room temperature condition.

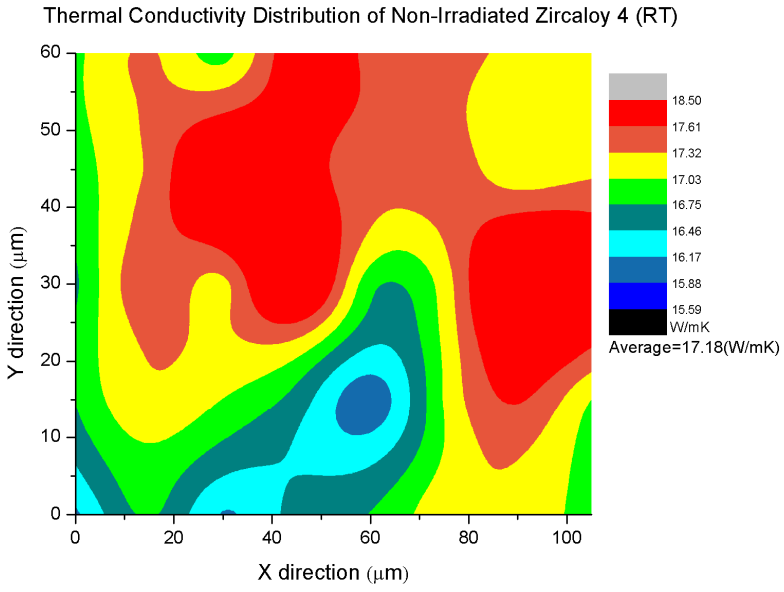

Figure S3.31 Thermal conductivity distribution for non-irradiated zircaloy

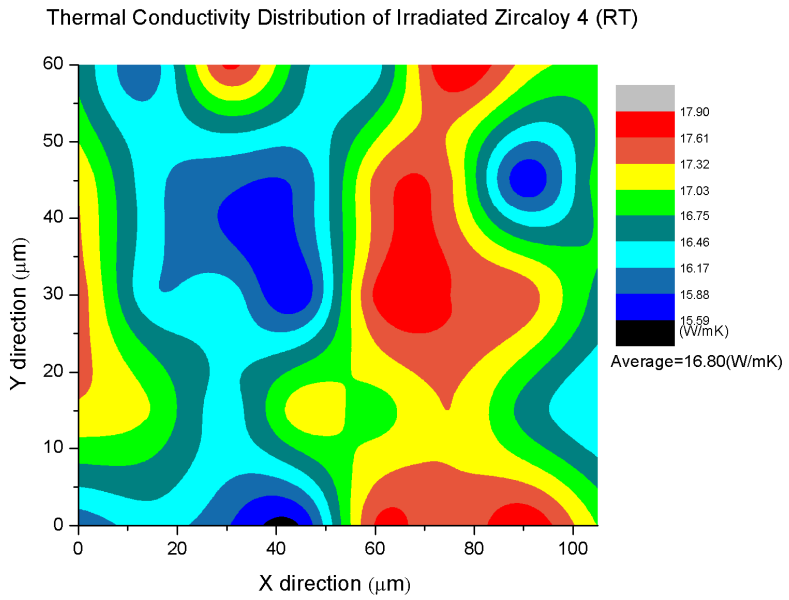

Figure S3.32 Thermal conductivity distribution for irradiated zircaloy

As we can see, the average thermal conductivity for non-irradiated zircaloy sample is 17.18 W/mK and the average thermal conductivity for irradiated zircaloy sample is 16.80 W/mK. The average thermal conductivity decreases about 2% after irradiation.

Part III: Phase-field modeling and Nuclear Code Translation of the Data (to MOOSE Framework)

Microstructure evolution under irradiation involves complex processes, including diffusion, interaction, clustering, and thermal recovery of voids. Point defects produced by displacement cascades interact with each other, aggregate into clusters and thus form voids/bubbles. Some of these point defects are recrystallized at high temperature when the energy of the material system exceeds its activation energy for the recombination. These processes can be only captured at the mesoscopic length and time scales.

The phase-field modeling has been used for mesoscale simulations to study the phase transformation and the kinetics of microstructure evolution in a wide range of materials and processes, including but not limited to solidification; Grafe et al. (2000; Loginova et al. (2001), solid-state phase transformations Wang and Khachaturyan (1997; Jin et al. (2001), grain growth Kazaryan et al. (2000), solute-dislocation interactions; Hu and Chen (2001), crack propagationAranson et al. (2000; Karma et al. (2001). In the phase-field model, the microstructure is represented by means of phase-field variables which are continuous across interfacial regions. The phase-field variables considered in modeling are of two kinds, one being concentration field variable which represent conserved features such as composition, vacancy concentration, density etc. and other one is order parameters depicting the non-conserved micro-structural features such as grain orientation, void concentration etc., to name few. In the phase-field model, microstructure evolution is governed by the Cahn-Hilland diffusion equation for concentration field Cahn and Hilliard (1958)

and Allen-Cahn equation for order parameters. This model uses thermodynamic free energy obtained from atomistic simulations, thermodynamic calculations, and experiments Hu and Henager Jr (2009b). The phase-field variables evolve such that the total free energy of the material system reduces.

Recently, in the last few years, the phase-field model has been applied to study the change of microstructural features under irradiation, such as nucleation and growth of gas bubbles and voids, and evolution of precipitate morphology Hu and Henager Jr (2009a; Millett et al. (2011a; Millett et al. (2011b; Crosby and Ghoniem (2012; Crosby and Ghoniem (2013) . However, the change of interfacial energy induced by the crystallographic mismatch between grains under irradiation has not been explicitly taken into account in such works. Fundamentally, if the evolution of irradiation damage can be correlated to fractal dimension at the microstructure level in terms of irradiation energy, the change of interfacial energy between grains under irradiation can also be predicted as a function of the magnitude of irradiation exposure energy. Also impact of irradiation energy on thermo-mechanical properties of the material can be quantified based on how microstructural changes such as void formation affects material properties.

1. Dislocation-vacancy interaction model

In present work, we primarily concentrate on capturing the microstructural changes during irradiation based on void formation and void clustering and relating effects of stress and thermal conductivity. Under irradiation point defects are created within the cascade leading to an increase of the point-defect concentration with the irradiation dose. Point defects act as barriers, reducing the mean free path of phone, which leads to the decrease of thermal conductivity. Different with other materials, zircaloy doesn't contain voids during irradiation. The dominant point defect clusters in zircaloy are dislocation loops. Therefore, the thermal conductivity of zircaloy doesn't have a large decline after irradiation. To capture the decrease in thermal conductivity, our new model mainly focuses on simulate the interaction between point defects and dislocation loops.

In last report, we introduced a dislocation model by using phase field method, it's based on linear elastic theory. It uses order parameters to describe the discontinuous relative displacements between the two lattice planes below and above the slip plane, measured in units of Burgers' vectors. The eigenstrain caused by this misfitting could be written as a dyadic product of the Burgers vector and the unit vector normal to the slip plane.

$$\varepsilon_{ij}^{0}(\alpha, m_{\alpha}) = \frac{b(\alpha, m_{\alpha})_i n(\alpha)_j}{d} \qquad (42)$$

a) Free Energy formulation

To account the vacancy diffusion, one more variable is added to the model, Cv, which stands for the vacancy concentration. Therefore, the total energy is also different from the previous model. Now, there are four terms in the total free energy E^{total}: the elastic strain energy E^{elas}, the crystalline energy E^{crys}, the gradient energy E^{grad} and chemical free energy E^{chem}. $E^{total} = E^{elas} + E^{crys} + E^{grad} + E^{chem}$. The elastic energy is calculated using the linear

elasticity theory of Khachaturyan and Shatalov [4]. It's given as

$$E^{elast} = \frac{1}{2} f\left[C_{ijkl}\tilde{\varepsilon}_{ij}^{0}(k)\tilde{\varepsilon}_{ij}^{0}(k)^{*} - e_i\tilde{\sigma}_{ij}^{0}(k)\Omega_{ik}(e)\tilde{\sigma}_{ij}^{0}(k)^{*}e_l\right]\frac{d^3k}{(2\pi)^3} - \sigma_{ij}^{appl}\int\varepsilon_{ij}^{0}(r)d^3r$$

Where the symbol f characterizes a principal value of the integral (excluding the point k = 0), and the superscript * defines a complex conjugate. C_{ijkl} is the elastic modulus tensor, and $\varepsilon_{ij}^{0}(r)$ is the stress-free strain,

The crystalline energy is a general Fourier expansion series, proposed for a3D periodical crystalline potential whose degenerated minima are located at the crystal lattice sites. A simplified approximation was employed,

$$E^{cryst} = \int dr \sum_{\alpha,m_\alpha} A\sin^2 \pi\eta(\alpha, m_\alpha, r)$$

The gradient penalty term to be used in PFM simulations of dislocations must be a bit more complicated than the normal case. In particular, it should not penalize the gradient across the area enclosed by a dislocation loop, otherwise, there will appear an unphysical interface with an extra energy proportional to the area.

$$E^{grad} = \varepsilon\sum_{\alpha}\int[\vec{n}^{\alpha}\times\nabla\eta]^2 dV$$

This gradient function will ensure gradient energy only comes along the dislocation loop, there's no contribution outside the slip plane.

Finally, the chemical free energy of vacancy can be described by the ideal solution model considering the dilute nature of vacancy concentration,

$$E^{chem} = \frac{1}{V_m}\int C_v E_v^f + RT[C_v\ln C_v + (1-C_v)\ln(1-C_v)]dV$$

b) Kinetic equations

For the non-conserved order parameter, such as η, which is introduced to describe the dislocation core area, is governed by the time dependent Allen-Cahn equation. It assumes the evolution rate of the order parameter is linearly proportional to the thermodynamic driving force or the first order functional derivative of the total free energy,

$$\frac{\partial\eta}{\partial t} = -L\frac{\delta(E^{elas} + E^{crys} + E^{grad})}{\delta\eta}$$

For the evolution of local vacancy concentration, we introduce a reaction-diffusion model to describe both long-range vacancy transport and short-range vacancy absorption at dislocation core associated with dislocation growth. The combined reaction-diffusion equation is give as,

$$\frac{\partial C_v}{\partial t} = \nabla\left(M_v\nabla\frac{\delta E^{total}}{\delta C_v}\right) - \sum_{\alpha}\frac{\partial\eta_\alpha}{\partial t}$$

The first term of above equation is from the standard Cahn-Hilliard equation while the second one is the reaction term that describes local vacancy annihilation at dislocation cores. The proportionality of unity in the second term reflects the fact that a missing atomic plane or a vacancy loop is an ideal source of vacancies. It should also be noticed that vacancy concentration is a non-conserved field variable only at dislocation cores, while it's still a conserved variable outside the core region.

c) Preliminary results

Dislocation growth and vacancy absorption

In the following pictures, we show how the dislocation core and vacancy concentration changes during simulation. The model is built with uniformly distributed vacancy concentration. The dislocation lays on the slip plane with a normal vector <0, 0, 1>, which is along the Z-axis. The burger's vector is <1, 0, 0>, which is along the X-axis. The stress free strain inside the dislocation core has only one non-zero component σ_{13}. Therefore, a shear loading is applied as the external force.

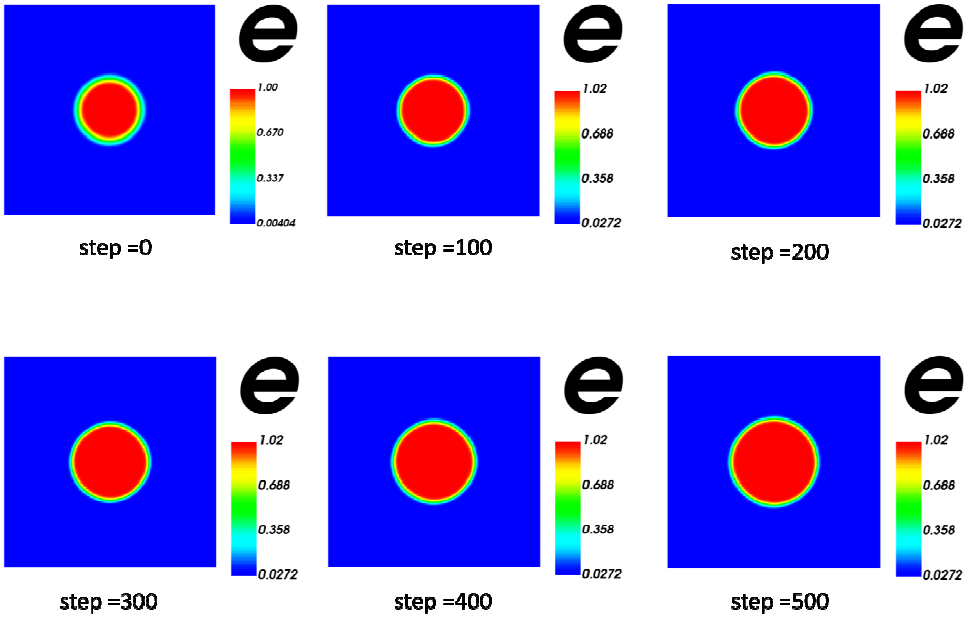

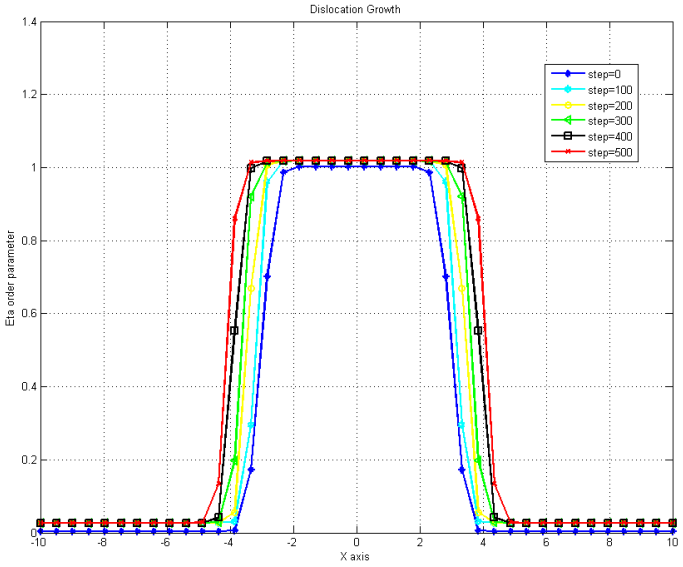

Figure S3.33 Dislocation loop growth

The above picture shows the dislocation core growth during the simulation. This is mainly caused by the external loading and the vacancy absorption. Next, we are going to show the vacancy distribution associated with the dislocation growth process.

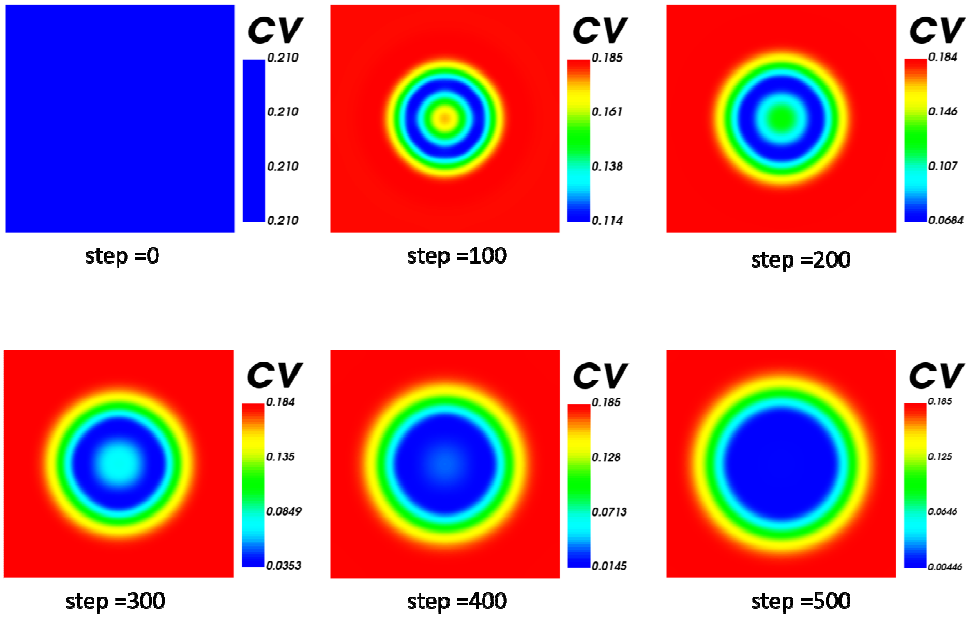

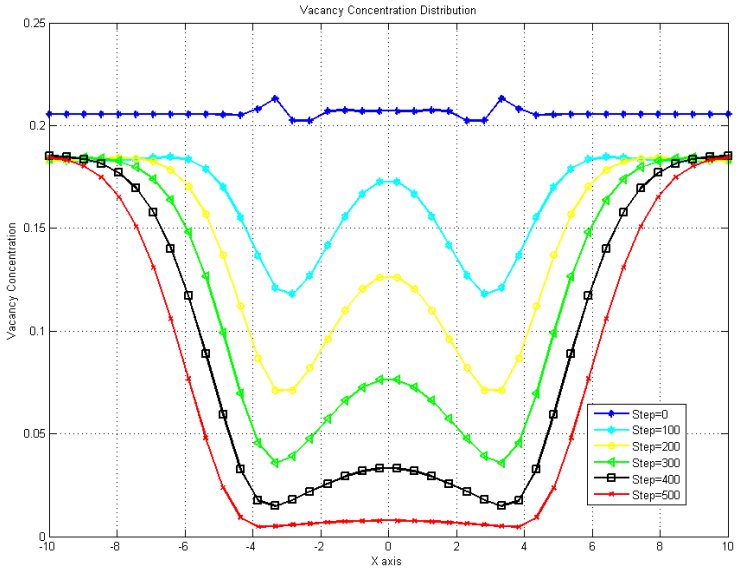

Figure S3.34 vacancy concentration distribution change

We can get several important points from this plot. As we see, the vacancy concentration in the domain is decreasing, this is mainly caused by the vacancy absorption of dislocation core. The absorption starts at the interface of dislocation, and it's absorbing vacancies both inside and outside the dislocation core. Therefore, vacancy concentration distribution looks like a double well function at the beginning part. However, as the absorption goes on, the vacancy concentration at the center keeps decreasing. Then the vacancy concentration distribution becomes a single well function. If this simulation goes long enough, the system will reach a quasi-steady-state. In this situation, the vacancy concentration inside the dislocation core will become very low and reach the equilibrium value. As the dislocation grows larger and larger, its influence zone also grows larger. The vacancy gradient drives vacancy diffuse toward the dislocation core area. However, if it's far enough from the dislocation, the vacancy concentration keeps as a constant value during the simulation. This is also agree with the first part (Cahn-Hilliard equation) of the kinetic equation.

d) Vacancy Source

Since the dislocation core acts as a vacancy sink, the vacancy concentration in the simulation domain keeps decreasing, this will gives an increasing thermal conductivity, which is unphysical. Therefore, we need to introduce a vacancy source into this simulation to account the irradiation cascade effect. To do this, we can simply add a source term into the governing Cahn-Hilliard equation,

$$\frac{\partial C_v}{\partial t} = \nabla\left(M_v \nabla \frac{\delta E^{total}}{\delta C_v} \right) - \sum_{\alpha} \frac{\partial \eta_\alpha}{\partial t} + p_v$$

The last term in above equation is the source term. The generation rate can be calculated by $p_v \approx d(dpa)/dt$.

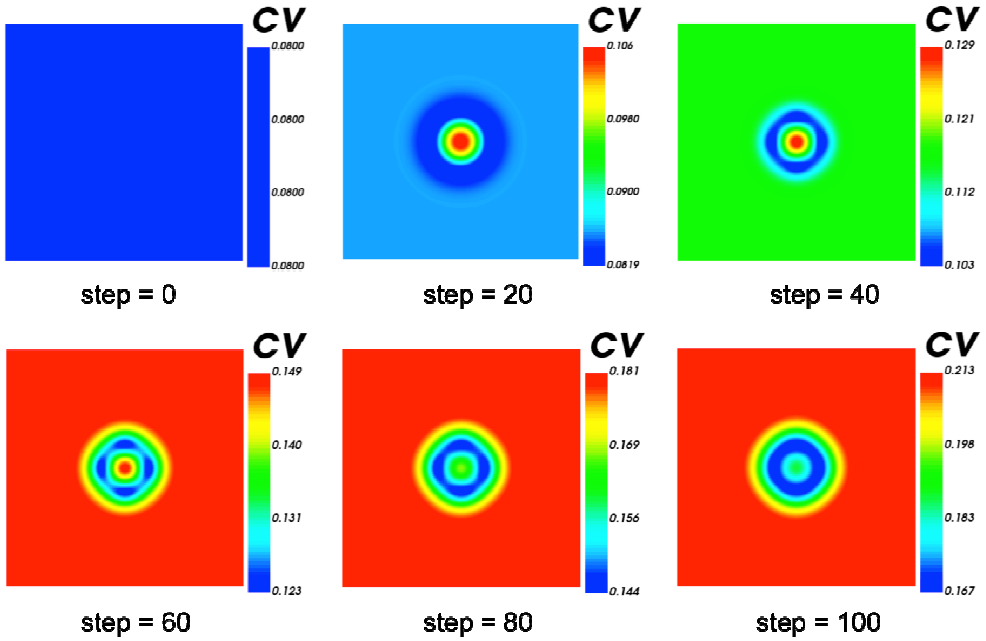

Figure S3.35 Vacancy distribution with vacancy source

Above figure shows the vacancy concentration change after adding the vacancy source term. The biggest difference with before is that the total vacancy concentration is not monotonic decreasing any more. At the beginning part, the vacancy concentration is decreasing, because the dislocation sink strength is high and dominates the simulation. As the simulation goes on, the dislocation sink strength gets lower, because the vacancy concentration field around the dislocation core is approaching its quasi-steady-state. Then the vacancy source starts to dominate the simulation. The total vacancy concentration starts to grow.

e) Effective Thermal Conductivity

Point defects, such as vacancy, will influence the thermal conductivity of the simulation domain, because they will reduce the mean free path of the phonon. Using equation $k = (1 - c_v^2)k_{bulk}$ for the local thermal conductivity at each quadrature point. If we introduce a constant heat flux at one side of the simulation domain, and fix the temperature at the other side. The effective thermal conductivity can be written as,

$$\mathrm{k} = \frac{\mathrm{flux} \times \mathrm{dL}}{|\Delta T|}$$

dL is the length of the simulation domain along the heat flux direction. ΔT is the temperature difference between two boundaries. The effective thermal conductivity is in unit W/m*K.

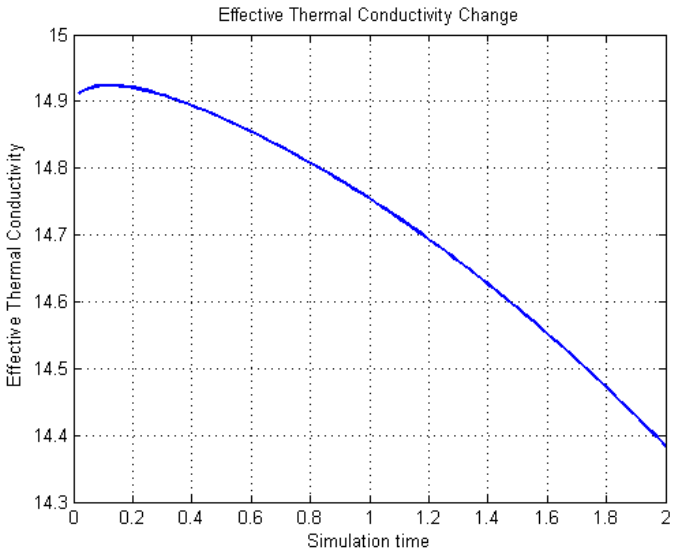

Figure S3.36 effective thermal conductivity

As we can see, in this simple test, the effective thermal conductivity decreases as the vacancy concentration increases, it consists with our expectation.

From this simple test, we show the availability of this model. There are still many things to be done. First of all, we need to plug in correct parameters associated with zircaloy, such as diffusivity, vacancy formation energy. Secondly, the vacancy source in this model is uniformly distributed.

f) Phase field model for zircaloy microstructure

From the existing dislocation model simulation results we can see that dislocation is actually acting as a point defects sink. To avoid dislocation dynamics in our phase field model, the basic idea is that we don't consider any single dislocation loops any more. When we gets to a larger simulation scale, there is no dislocation loops appear in our simulation domain. We can set up an aux variable to account the local abstract dislocation density, and this aux variable η varies in space, but not in time, which means it's just a fixed value to provide information about the dislocation information about the microstructure. The local sink strength for point defects is determined by the local aux variable value, which means if there are more dislocations then it has stronger sink strength for point defects.

The real variables in our model would be c_v and c_i, stands for the vacancy concentration and interstitial concentration. The free energy term is derived in terms of the enthalpy and entropic contributions of both vacancies and interstitials, and is written in form,

$$f^s(c_v, c_i) = E_v^f c_v + E_i^f c_i + k_B T[c_v \ln(c_v) + c_i \ln(c_i) + (1 - c_v)\ln(1 - c_v) + (1 - c_i)\ln(1 - c_i)]$$

Then the total free energy function is described by,

$$F = \int f^s(c_v, c_i) + \frac{K_v}{2}|\nabla c_v|^2 + \frac{K_i}{2}|\nabla c_i|^2 dV$$

Following the standard procedure in the phase field approach, the kinetic equations for the spatial and temporal evolution of the concentration fields have been derived as the Cahn-Hilliard equation,

$$\frac{\partial c_v}{\partial t} = \nabla\left(M_v \nabla \frac{\delta F}{\delta c_v}\right) + P_v - R_{iv} - S_v(\eta)$$

$$\frac{\partial c_i}{\partial t} = \nabla\left(M_i \nabla \frac{\delta F}{\delta c_i}\right) + P_i - R_{iv} - S_i(\eta)$$

The on-going production of vacancies and interstitials due to irradiation is incorporate into the model via the source terms P_v and P_i added to the right hand side of above equation. The vacancy-interstitial recombination term R_{iv} represents a rate of mutual annihilation that is proportional to both the vacancy and interstitial concentrations. The last term is the sink/source term for vacancies and interstitials, it's a function of local dislocation density, and it could be written as,

$$S_v(\eta) = S_r^v \eta^2 (c_v - c_v^{eq})$$

$$S_i(\eta) = S_r^i \eta^2 (c_i - c_i^{eq})$$

The parameters S_r^v and S_r^i describe the efficiency of either nucleation or annihilation. It contains η^2 in the term, so higher dislocation density would give us stronger sink/source effect. For over-saturated vacancy concentrations $c_v > c_v^{eq}$, the last term will be positive, and $S_v(\eta)$ will act as a vacancy sink. Conversely, for under-saturated vacancy concentrations $c_v < c_v^{eq}$, the last term will be negative, and it will act as a vacancy source. It's same for interstitials. In same procedures, we can also add a similar term for the sink/source at grain boundaries.

Point defects have great influences on bulk thermal conductivities. We can calculate local thermal conductivity at each quadrature point based on its vacancy/ interstitial concentration. Then we can calculate the effective thermal conductivity at each simulation time step.
This model is mainly taking care of the microstructure and irradiation dependent thermal conductivity.

g) Strain effect on thermal conductivity

Applying stress/strain on a material provides a mechanism to tune the thermal conductivity of materials dynamically or on demand. Experimental and simulation results have shown that thermal conductivity of bulk materials can change significantly under external pressure (compressive stress). The cladding in the nuclear core is surrounded by coolant. Therefore, external pressure is always loaded on it. As the fission gases accumulate inside the tube, there's also internal pressure acting on the inner surface of the cladding. In this case, the stress and strain distribution will definitely affect thermal conductivity of the cladding material.
S Bhowmick [13] obtains a simple relation that determines the strain and temperature

dependence of thermal conductivity for solid bulks. They compute the thermal conductivity of a solid described by a simple empirical potential Lennard-Jones potential for argon using classical molecular dynamics via the Green-Kubo relations. Based on these calculations, a simple empirical form for the strain/temperature dependence of conductivity is give as,

$$\kappa = AT^{-\alpha}\left(\frac{V}{V_0(T)}\right)^{-\gamma}$$

where A, α, and γ are constants, and V_0 and V are, respectively, the equilibrium unstrained volume and volume of the strained lattice at absolute temperature T, this actually relates to the local strain values. The best fit values of A, α, and γ for the Lennard Jones system are 4.61, 1.45, and 9.59, respectively (the units of κ is W/m K and that of T is K). The result is verified in K. V. Tretiakov's work [14].

For our case of zircaloy, when the structure is strain free, which means strain is zero($\varepsilon = 0$ when $\frac{V}{V_0} = 1$). The above equation will reduce to $\kappa = AT^{-\alpha}$, then we can use reported data to do curve fitting to get values of A and α for zircaloy. The thermal conductivity is reported as:

$$k = 12.767 - 5.4348\times10^{-4}T + 8.9818\times10^{-6}T^2 \quad (Wm^{-1}K^{-1})$$

By using curve fitting method for T from 400K to 700K, we can find the parameters are A=1.911 and $\alpha = -0.33$. For the coefficient γ, dependence of strain, we can use our experiment results to get it. We can measure the thermal conductivity at different compression strain, and use the data fitting to get coefficient γ.

After determine the parameters above, we can add the stress/strain dependence of thermal conductivity to the simulation model. The volume change $\frac{V}{V_0}$ can be determined by solving the local strain tensor. Then by using above equation, we can determine the local thermal conductivity value at each quadrature point. Using the method we have before, we can solve the effective thermal conductivity for the whole domain.

This model is mainly taking care of the stress/strain dependence of thermal conductivity. It could be coupled with the previous phase field model through the tensor mechanics module.

Both microstructure and stress/strain influences on thermal conductivity of materials are counted in the simulation, irradiation effects are mainly counted as vacancy/interstitials source term, heat flux value at boundaries and external loading conditions. There are several things we need to consider when we use this model to predicting thermal conductivity of zircaloy and uranium dioxide.

Zircaloy:

Since there's no voids in zircaloy, the thermal conductivity doesn't change significantly during

irradiation. Therefore, we need to determine the proper parameters and try to capture the really physical phenomena.

- Performing SEM at Raman data points to get detailed information about the local microstructure.
- Determining the irradiation vacancy source. For example, through calculation, if we have a typical fast neutron flux as $5 \times 10^{17}\ nm^{-2}s^{-1}$. Then at 600K, one PKA could produce 40 displaced atoms, and the collision rate is $5\ \frac{collisions}{100nm^2 \cdot 1nm \cdot 1ns}$. We need to use this information to get the proper vacancies/interstitials concentration local change at each cascade event.
- Determining the sink strength of dislocation. Since the typical fast neutron flux is $5 \times 10^{17}\ nm^{-2}s^{-1}$, which is smaller than $5 \times 10^{25}\ nm^{-2}s^{-1}$. The dislocation is only <a> type. The typical dislocation density is $5 \times 10^{21}\ m^{-3}$. Combine dislocation-vacancy interaction simulation result, we can calculate the vacancy sink strength according to local dislocation density.

Uranium dioxide:

The biggest difference with zircaloy is that irradiation will induce voids into the microstructure of uranium dioxide. In this case, dislocations are less important in this model. Moreover, there is no external loading on the pellet, stress/strain dependence of thermal conductivity also plays a very small rule here. As we can see, this makes the uranium dioxide simulation much easier. Instead of having an order parameter for local dislocation density, we now have an order parameter to distinguish the matrix phase and the void phase. And this non-conserved variable will be controlled by the Allen-Cahn equation. We already have some results for this model and showed in previous reports.

2. Influence of Voids in UO_2

Along with the formation of voids and interstitials, fission nuclear reactions also creates gas bubbles trapped in the materials. During irradiation of light water reactor (LWR) fuel, the fission process generates many different fission product atoms, including xenon (Xe) and krypton (Kr) atoms. Because of the extremely low solubility of the noble gas atoms in the UO2 matrix, gas bubbles composed of Xe , Kr, and other gas atoms precipitate within the UO2 grains and, depending on the temperature conditions, gas atom diffusion will result in nucleation and growth of gas bubbles on the grain boundaries. Continuum-level mechanisms, such as fission gas release to the fuel rod environment and volumetric swelling due to bubble growth, are included in nuclear fuel performance assessments. The behavior of fission gas atoms in UO2 has been extensively studied using experiments performed on single crystal and polycrystalline material under a variety of temperature and irradiation conditions for more than 50 years Yulan Li (2012). From these studies a general

picture of the mechanisms that influence the transport and release of fission gas atoms has been developed. A schematic of these processes is shown in Fig. S3.37. First, a gas atom is created within a region of radiation-induced vacancies and interstitial atoms caused by the atomic interactions/cascades during the stopping process following fission. Gas atom diffusion assisted by uranium (U) vacancy clusters then takes over until nucleation of small high pressure intra-granular bubbles.

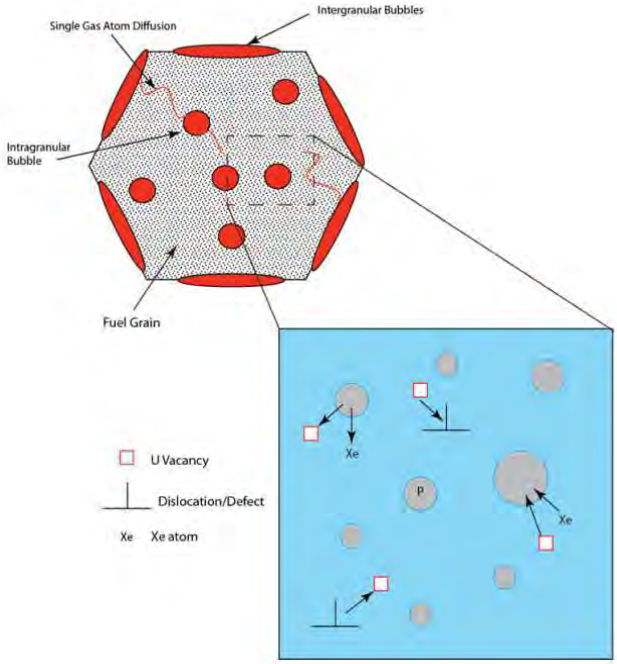

Figure S3.37. Schematic process of thermally induced fission gas diffusion and release from fuels Yulan Li (2012).

Heterogeneous gas bubble microstructure within the grain and along the grain boundaries has been observed in UO_2 fuels. The pre- and post-thermal annealing appearance of the fission gas bubbles within the grain and along the grain boundaries obtained from transmission electron microscopy are shown in Fig. S3.38.

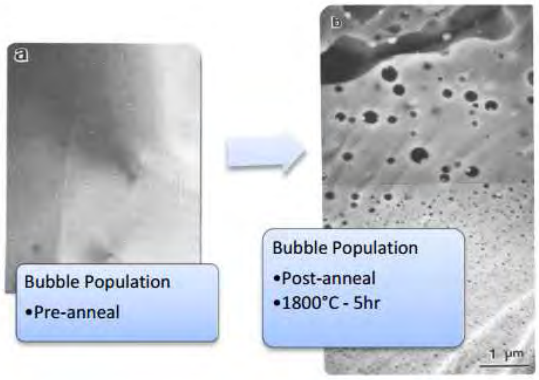

Figure S3.38. Gas bubble formation in UO2 Yulan Li (2012)

It is clearly seen that the gas bubbles near the GB have much larger size than those inside the grain. Structural defects such as dislocations and GBs which act as sinks and/or sources of vacancies, interstitials, and gas atoms, play an important role in gas bubble evolution kinetics and the formation of the heterogeneous gas bubble microstructure in polycrystalline UO2 materials. In order to evaluate the role of the different microstructure mechanisms on the intra-granular bubble distribution and grain boundary bubble nucleation and growth, the current model needs to be extended to incorporate the effect of grain boundaries on gas atom diffusion, grain boundary bubble formation, and growth. Along with the vacancy concentration variable additional conserved phase field variable corresponding the gas bubble concentration needs to be taken into account and additional free energy terms (f_g) needs to be incorporated to capture the material behavior;

$$f_g = E_g c_g + K_B T\left(c_g \log\left(c_g\right) + \left(1-c_g\right)\log\left(1-c_g\right)\right) \qquad (1)$$

here, c_g represents the gas concentration and E_g is the energy barrier for bubble formation. Intergranular bubbles can be introduced in a polycrystalline structure while generating the initial condition and it's impact on the microstructural changes including grain growth can be studied.

Ahmed et al. (2014) has studied grain growth in porous UO_2 due to irradiation. Fig. S3.46 represents microstructural images from the study.

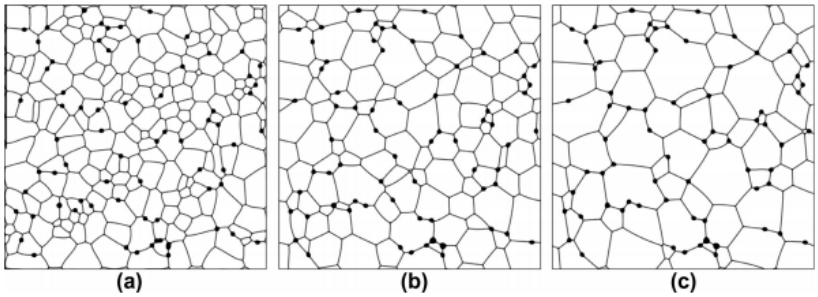

Figure S3.46. Snapshots of microstructure evolution of slightly porous UO2 Ahmed et al. (2014)

Changes in grain size and porosity during irradiation has been evaluated here. It is observed that, as the porosity increases, grain growth in UO2 gradually changes from boundary controlled growth to pore controlled growth. For high porosity levels, the grain growth completely stops after a short evolution time. It is also found that the inhomogeneous distribution of pores leads to abnormal grain growth even without taking into account the anisotropy in grain boundary energy and mobility. The following figure shows the voids nucleation process in uranium dioxide matrix during irradiation.

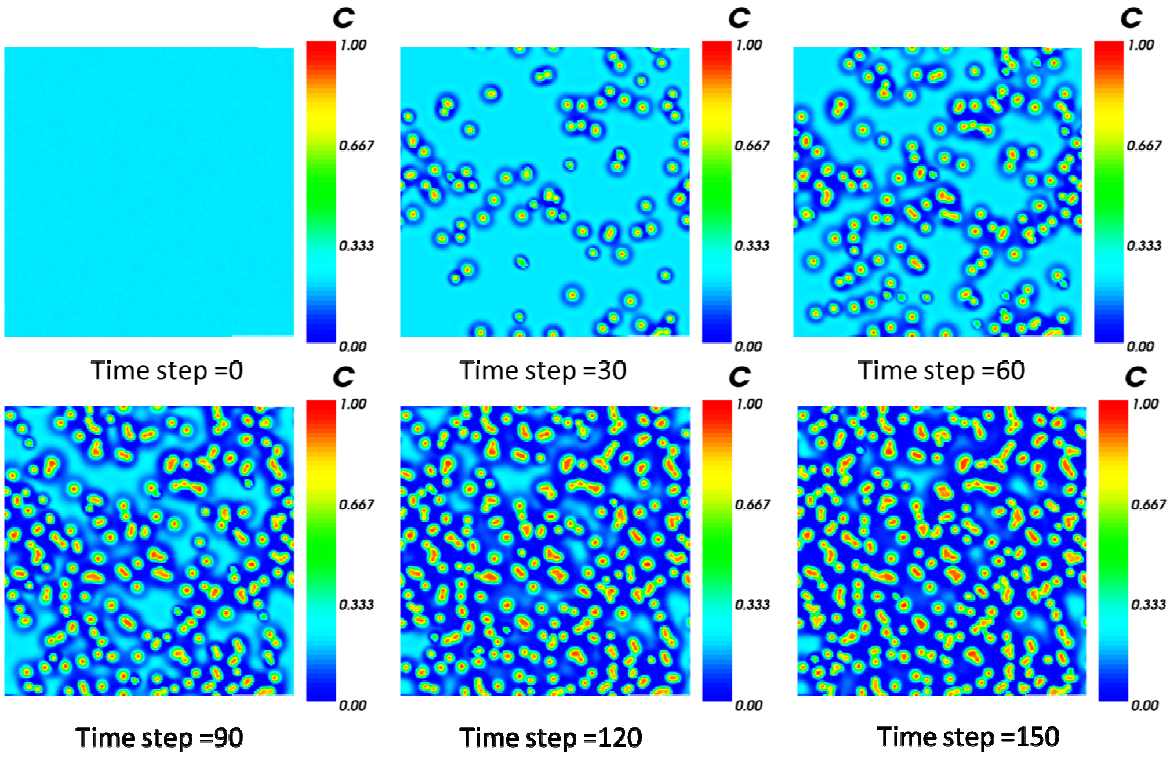

Fig. S3.47 voids nucleation in uranium dioxide

As more and more voids in the matrix material, the effective thermal conductivity of the domain will decrease. In this simulation, we use solid uranium dioxide thermal conductivity for the bulk, which is 2.75 (W/mK) at around 1273K [7]. we use 0.42 (W/mK) for the thermal conductivity of Helium in 1273 K. Using equation $k = (1 - c_v^2)k_{bulk} + c_v^2 k_{void}$ for the thermal conductivity for the interface. When $c_v < 0.1$we consider it as matrix, $c_v > 0.9$ as void, between 0.1 and 0.9 all considered as interface region.

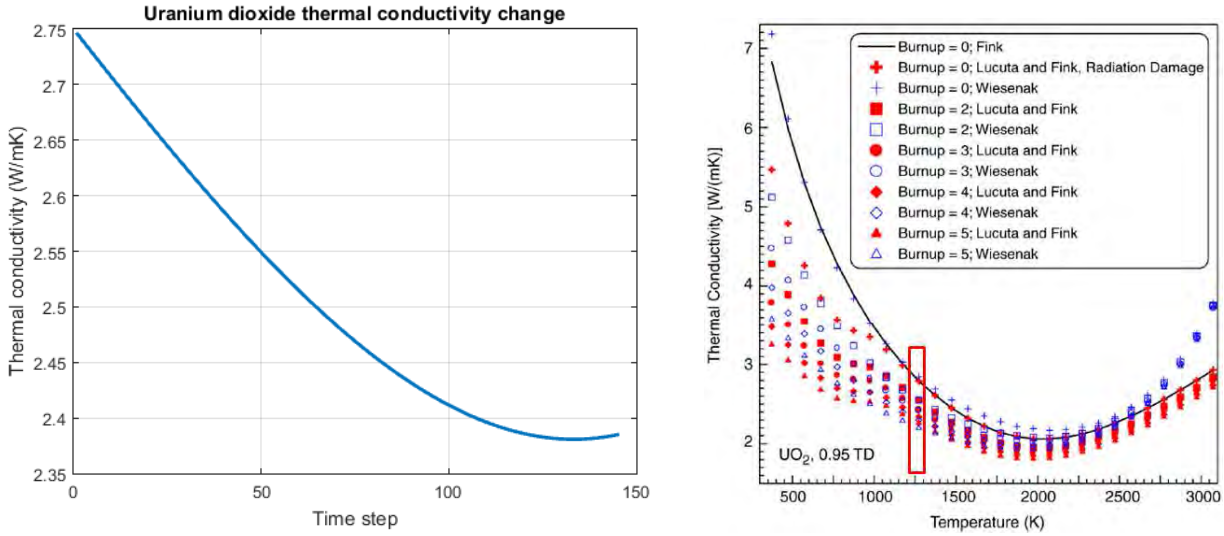

Fig. S3.48 (right) effective thermal conductivity change of uranium dioxide; (left) thermal

conductivity for uranium dioxide with different burnups

The thermal conductivity decrease as more and more voids appears in the matrix. After voids saturation, the effective thermal conductivity is around 2.62 W/mK according to our simulation. This value is close to the reported data for irradiated uranium dioxide at 1250K [7].

III.3 Pellet Cladding Mechanical Interactions

Pellet-cladding interaction (PCI) is one of the most important phenomena leading to fuel rod failure, which has been studied worldwide for many years [1]. But it still remains a great concern, since that mechanical interaction is not well understood and further work is useful in this area. A typical rupture of the cladding due to PCI during a power ramp test could lead to invoke several factors. Among these factors, three most important ones are:

- Stress corrosion cracking acceleration due to iodine produced in the pellet under irradiation.
- Stress concentration in the cladding due to a pinch effect associated to pellet hourglass shape.
- Strain localization in the cladding due to crack opening between two pellet fragments.

A nuclear fuel element typically consists of a tube containing cylindrical uranium dioxide fuel pellets. Typical radial clearance between the oxide pellet and the cladding inner radius at this initial cold state is 200 to 400 microns. In the reactor, heat is generated throughout the pellets and is conducted through the cladding tube to the surrounding coolant. After insertion in the core and startup, a parabolic temperature gradient is generated in the fuel pellets (~100 ˚C/mm), and the central axis becomes the position of the maximum temperature due to the low thermal conductivity of uranium dioxide. This temperature gradient has significant influence for both the cladding and the pellet.

For the pellet, the initial heat up causes both thermal expansions leading to cracking as well as densification due to additional sintering of the pellet. The cracking is a consequence of the stresses induced in the pellet due to differential thermal expansion. Moreover, at high power, gaseous fission products are created and stored in the fuel, causing an additional pellet diameter increase. For a Zircaloy cladding with a typical service temperature of 600 K, creep becomes an important consideration. The external coolant pressure is about 15 MPa, therefore there is a significant stress driving cladding creep-down onto the pellet. Consequently, the gap size decreases to gap closure.

After contact of fuel pellets and cladding, the presence of cracks in the pellets, which open to accommodate the excess central thermal expansion, intensifies the stresses locally and leads to strain–stress concentrations in the cladding. In the 70s and 80s, this mechanism has been studied in detail through the development of elastic two-dimensional analytical or numerical models [2,

3, 4]. From these studies, people notice that friction at the pellet-cladding interface is the dominant parameter with respect to stress concentration in the cladding (it maximizes interfacial shear stresses). The pellet hourglass shape, which results from a power increase, will also cause an increase in the clad hoop stress at the pellet end relative to that at the mid-pellet (MP) plane, leading to the so called bamboo like shape of the cladding with regularly spaced ridges. Recent non-linear analyses also shows the similar conclusions.

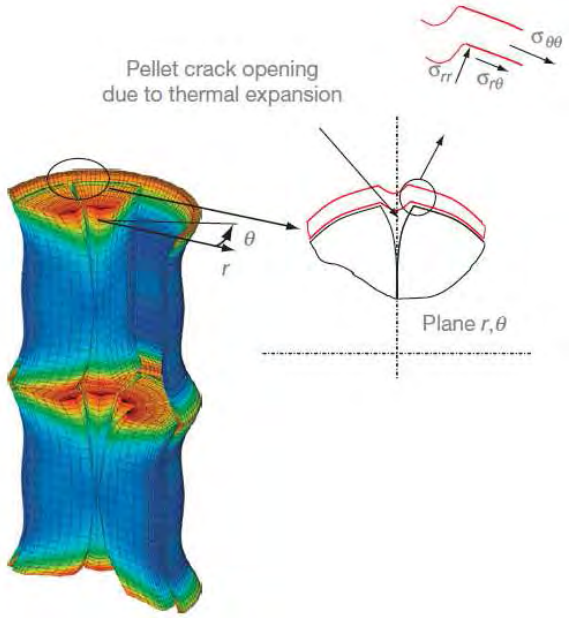

Figure S3.49 Stress and strain concentration [Comprehensive nuclear materials].

Literature review indicates that friction at pellet-clad interface is a crucial parameter with respect to PCI-driven rod failures. It also shows that it evolves with irradiation (burnup). An experimental characterization of friction evolution during irradiation is very difficult to achieve and requires very sophisticated equipment. Therefore, numerical simulations of the irradiation behaviors in nuclear fuel rods are playing a more and more important role to interpret the damage mechanism and carry out parametric studies.

The first attempts to model PCI have focused on catching the stress–strain concentration in the cladding over an opening fuel crack. Approximate solutions have been derived from 2D elastic cladding models assuming a symmetric distribution of fuel pellet cracks with symmetric interfacial slippage [5, 6, 7]. More recently, 2D finite element analyses modeling of a fuel pellet fragment and the overlying piece of cladding have been performed to study in more detail the impact of friction bonding on stress–strain concentrations in the cladding [8 , 9]. Nowadays, progress in computational performance and finite element codes has made the simulation of the thermo mechanical behavior of a fragmented pellet enclosed in a viscoplastic cladding [10, 11, 12]. By providing sufficient mesh refinement, the stress and strain concentration in the cladding in front of the pellet crack can be described, particularly in 2D calculations. The complexity of

the problem is due to the high level of interaction between adjacent pellet fragments and at the pellet cladding interface. In practice, it's important to assess the validity of the stress and strain states in the cladding resulting from PCI as estimated by the finite element method.
The challenge for the simulation is developing 3D simulation to have a local stress concentration assessment at a scale of the micrometer. Because 3D local stress computation in the cladding is not consistent with experimental results because the mesh size of the finite element is not small enough to catch the stress concentration. This can be done by micro scale FEM simulation, combining with microstructure characteristics. The simulation result can be verified by using our nano-indentation Raman spectroscopy experiment, measuring the stress and strain distribution. The result can be used in the PCI simulation in engineering scale.

Typically, during a PCI ramp test, the power during the preconditioning period is about 20 kW/M, and the power during the holding period after transient could be up to 50 kW/M. The power rate during the transient is about 10 (kW/M min).
The temperature distribution through the pellet during preconditioning is about $840\ °C$ at the center and $470\ °C$ at the periphery. The temperature distribution through the cladding thickness is about $320\ °C$ at the internal surface and $290\ °C$ at the external surface. After transient, the temperature distribution through the pellet becomes about $1680\ °C$ at the center and $470\ °C$ at the periphery. The temperature distribution through the cladding thickness is about $360\ °C$ at the internal surface and $320\ °C$ at the external surface.
B. Michel (2008) [15] performed a detailed study of PCMI during the ramp test. Only one fourth of a single pellet fragment and the overlying piece of cladding is meshed. The size of the pellet fragment is consistent with post-irradiation pellet structure with has four to eight pellet fragments in the circumferential direction.

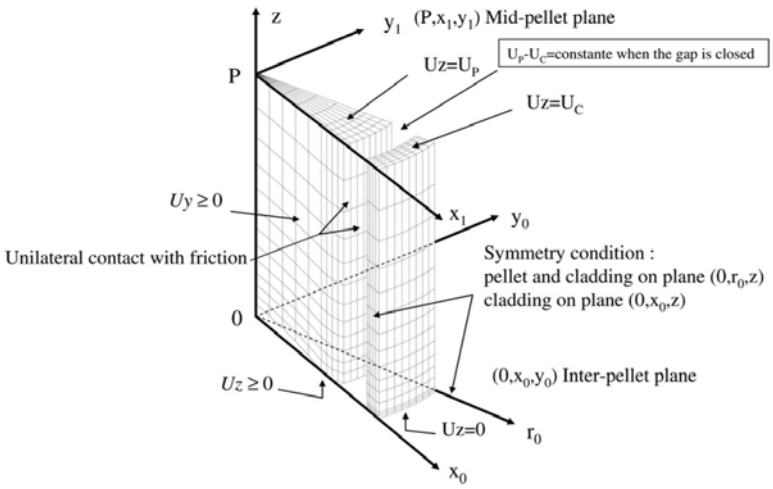

Fig. S3.50 3D PCI simulation symmetry and boundary conditions

The 3D simulation results shows, after the preconditioning period of the ramp test, the pellet cladding gap is closed for an important proportion of the interface. The contact pressure ($-\sigma_{rr}$) is about 40 MPa, it's higher than the internal pressure from fission gas which is about 8 MPa. Due to the contact pressure, the mean circumferential stress level is at a value of 10 MPa. Typically, the outer pressure due to the coolant fluid is about 13.5 Mpa, which gives an internal and external pressure difference of 5.5 MPa.

After the transient stage, the large temperature gradient in pellet lead to a volumn expansion with a hourglassing shape of the pellet fragment. These geometrical changes induce an enhancement of the pressure contact and then a tensile circumferential stress in cladding (mean value of $\sigma_{\theta\theta} = 465\ MPa$) and a pressure contact concentration at the inter pellet plane ($-\sigma_{rr} = 160\ MPa$). These values could be used in the simplified 2D model during the simulation of the transient stage of the power ramp test.

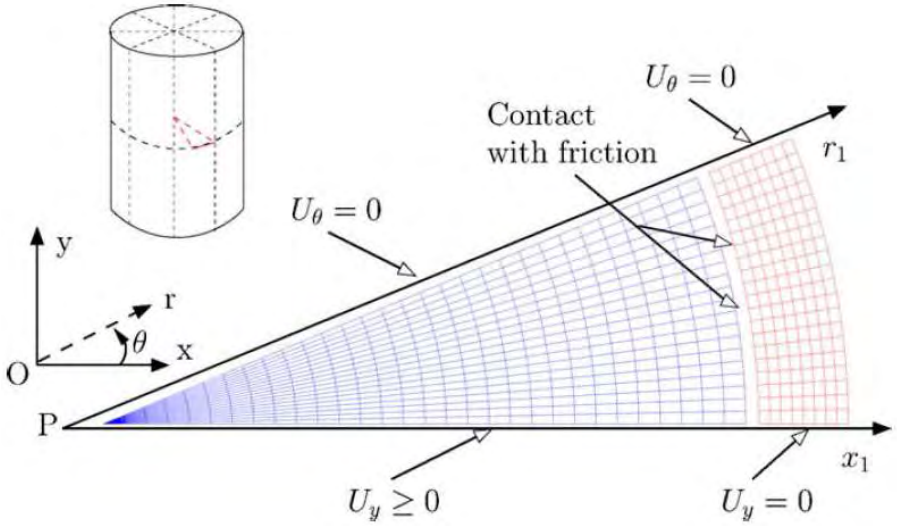

Fig. S3.51 2D PCI simulation symmetry and boundary conditions

The internal contact pressure equal to the mean value computed in the 3D model, which is about 70 MPa. An external pressure of the coolant fluid is 13.5 MPa. A shear stress $\sigma_{r\theta}$ at pellet cladding interface plays a very important rule in stress concentration in cladding. It's caused by friction, distributes as a decreasing function of the distance from the pellet edge through cladding thickness,

$$\sigma_{r\theta}(x) = \sigma_{r\theta}^{max}(1-x)^{15}$$

The maximal value is 100 MPa according to 3D simulation. X is the curvilinear distance from the pellet edge normalized to unity for an angular portion of 22.5°.

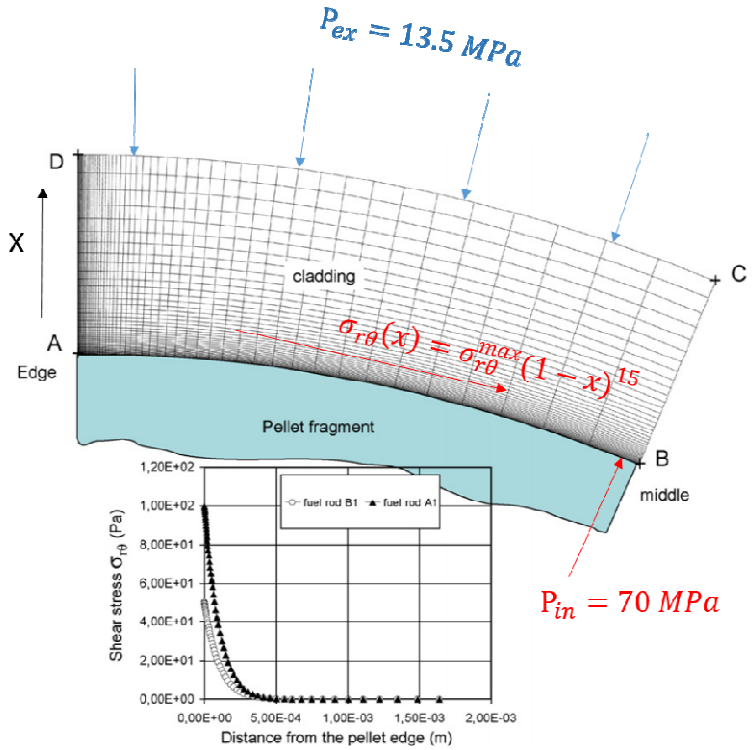

Figure S3.52 2D PCI simulation cladding boundary conditions

We also created a preliminary model for pellet cladding combination, shown in Fig. S3.53.

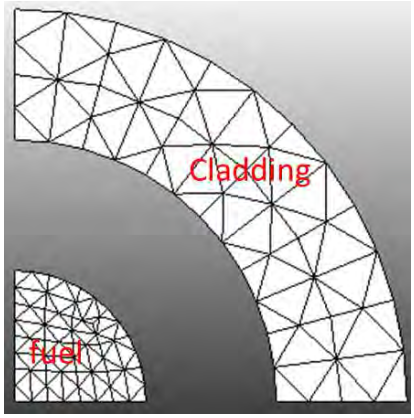

Fig. S3.53 Pellet cladding cross section model in 2D

For heat transfer test, we use constant thermal conductivity value for each part at this point. The values we use are 2.75 (W/mK) for fuel rod, 15.75 (W/mK) for cladding, and 0.42 (W/mK) for the gap between them. During the simulation, temperature at the center point of fuel rod increase linearly from 300 °C to 1000°C. Temperature at the outer surface of cladding is fixed to 300°C. Simulation results are shown below.

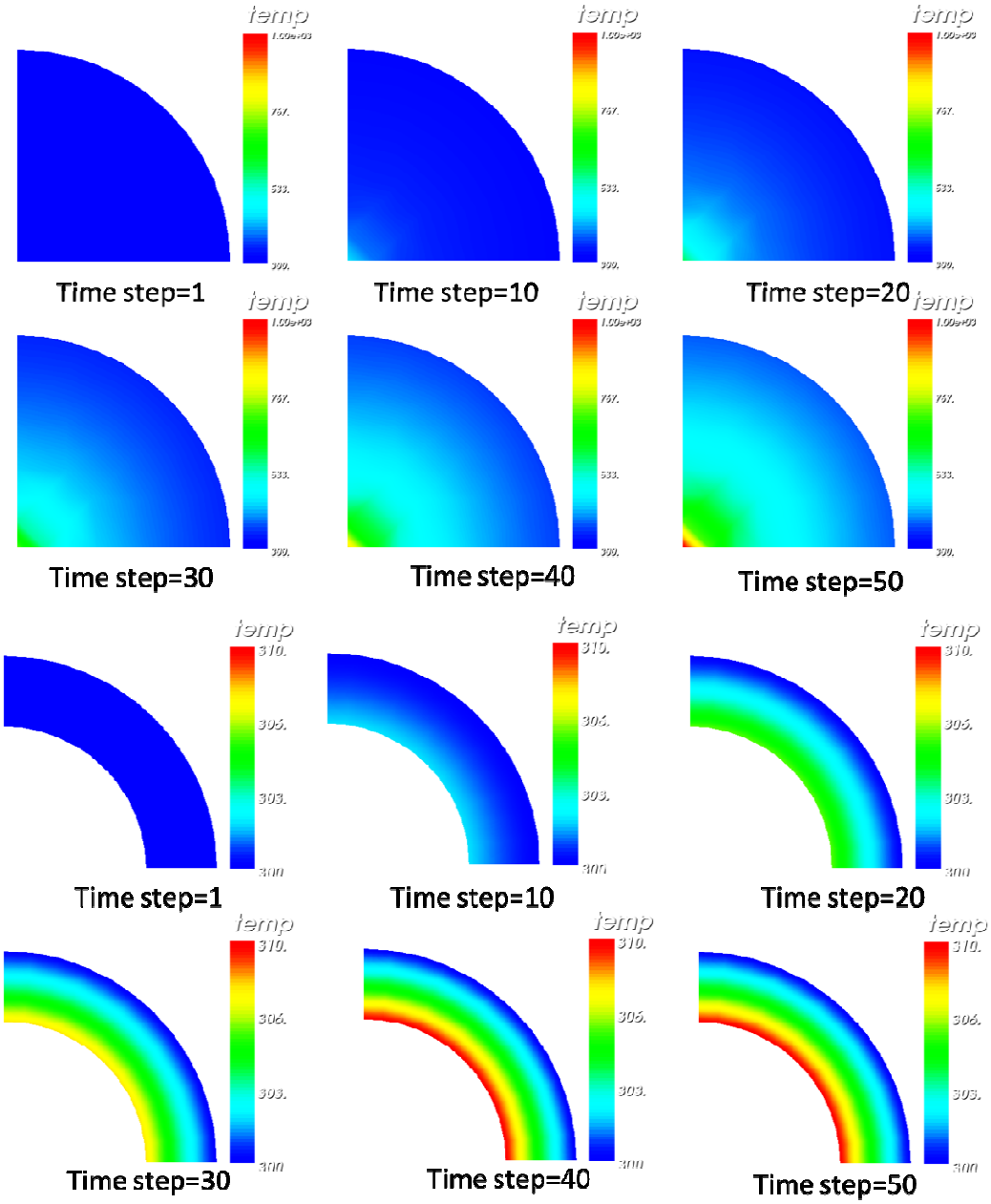

Fig. S3.54 (top) fuel rod temperature distribution; (bottom) cladding temperature distribution

As the simulation runs, temperature rises from the center point of fuel rod. There's temperature jump between the outer surface of fuel rod and inner surface of cladding. This's due to the physical gap between them. Figure S3.55 shows how temperature changes on these two surface according to the temperature at fuel rod center.

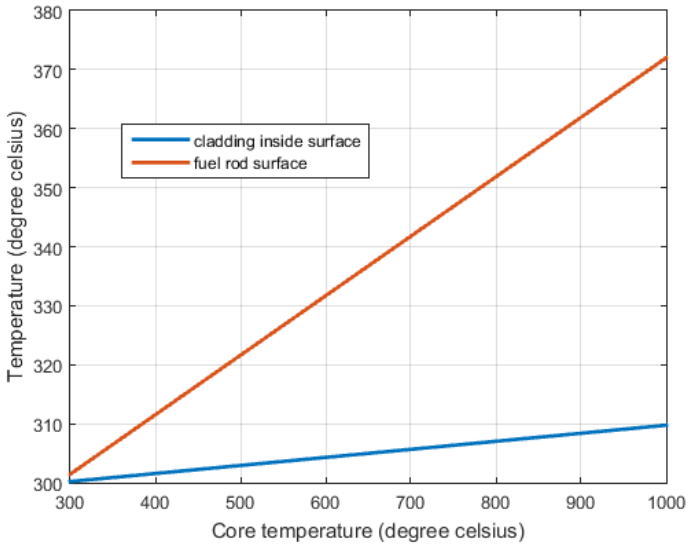

Fig. S3.55 temperature change on the outer surface of fuel rod and inner surface of cladding

The temperature on these two surfaces is changing linearly. However, the difference between them is getting larger and larger. This result is consistent with our expectation.

III.4 Pellet Cladding Interactions and Its Relation with Thermal Properties

Non-irradiated & Non-corroded sample

Gathering all above information, a contour plot of thermal conductivity distribution and stress distribution is shown in Fig. S3.57. Fig. S3.57 (a) shows the thermal conductivity distribution without any loading. The local thermal conductivity varies from points to points; this is mainly caused by the difference of microstructure, precipitates and silicon layer coating condition at each point. The effective thermal conductivity value over the whole domain is measured as 12.916 W/(m*K), which is very close to the value reported as 12.7 W/(m*K) at room temperature in literature [19].

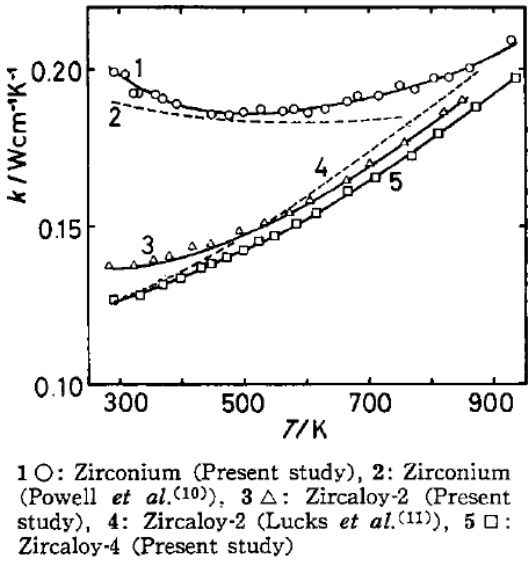

1 ○: Zirconium (Present study), 2: Zirconium (Powell *et al.*[10]), 3 △: Zircaloy-2 (Present study), 4: Zircaloy-2 (Lucks *et al.*[11]), 5 □: Zircaloy-4 (Present study)

Figure S3.56. Thermal conductivity of zircaloy-2,-4, and zirconium[19]

Fig. S3.57 (b) shows the thermal conductivity distribution with a loading of 2N. The distribution map agrees with the loading free case. However, value of each point decreases due to the influence of local stress state. The effective thermal conductivity decrease to 12.3 W/(m*K). After subtracting the temperature-induced Raman shift contribution, the remaining Raman shift was used to calculate stress. Fig. S3.57 (c) shows the stress conductivity distribution with a loading of 2N. The stress distribution is also affected by the microstructure and the precipitates. Comparing the stress distribution with the thermal conductivity change, it could be noticed that high stress state area induces larger thermal conductivity degradation. It clearly shows the stress effect on thermal conductivity change.

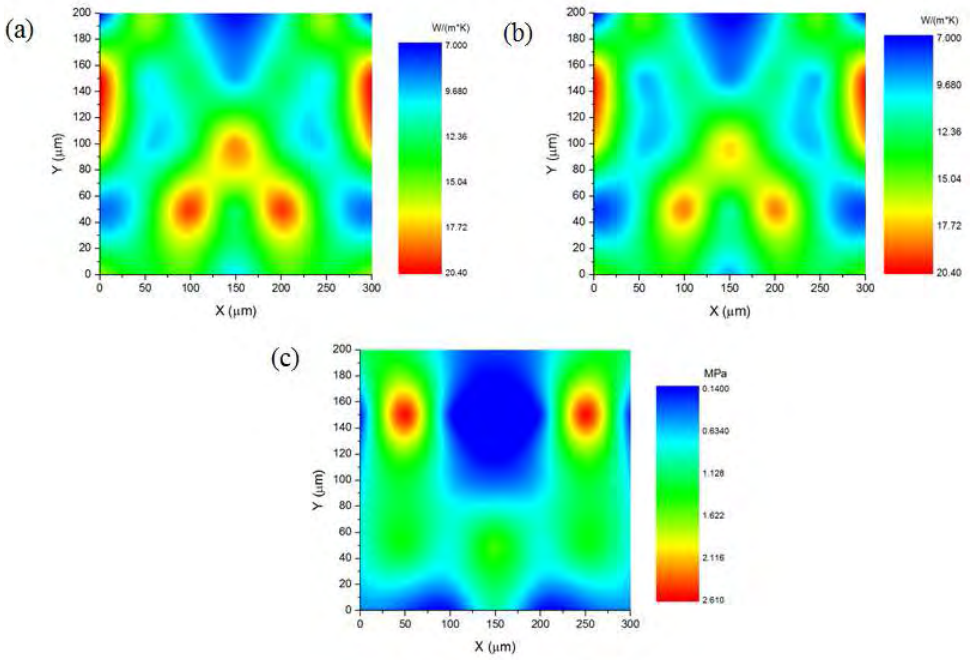

Figure S3.57. (a) Thermal conductivity distribution using Raman mapping at room without any loading, (b) Thermal conductivity distribution using Raman mapping at room during a loading of 2N, (c) Stress distribution using Raman mapping at room during a loading of 2N

Non-irradiated & 60 Days corroded sample

Similar method is used for the measurement on non-irradiated & 60 days corroded sample. Fig. S3.58 (a) shows the thermal conductivity distribution without any loading. The effective thermal conductivity value over the whole domain is measured as 12.83 W/(m*K). Comparing to thermal conductivity of non-irradiated & non-corroded sample, corrosion induces a slight decreasing on the average thermal conductivity value. Fig. S3.58 (b) shows the thermal conductivity distribution without a loading of 2N. After applying compressive load, the effective thermal conductivity decrease to 11.916 W/(m*K). Thermal conductivity degradation is also observed in this case. Fig. S3.58 (c) shows the stress conductivity distribution with a loading of 2N.

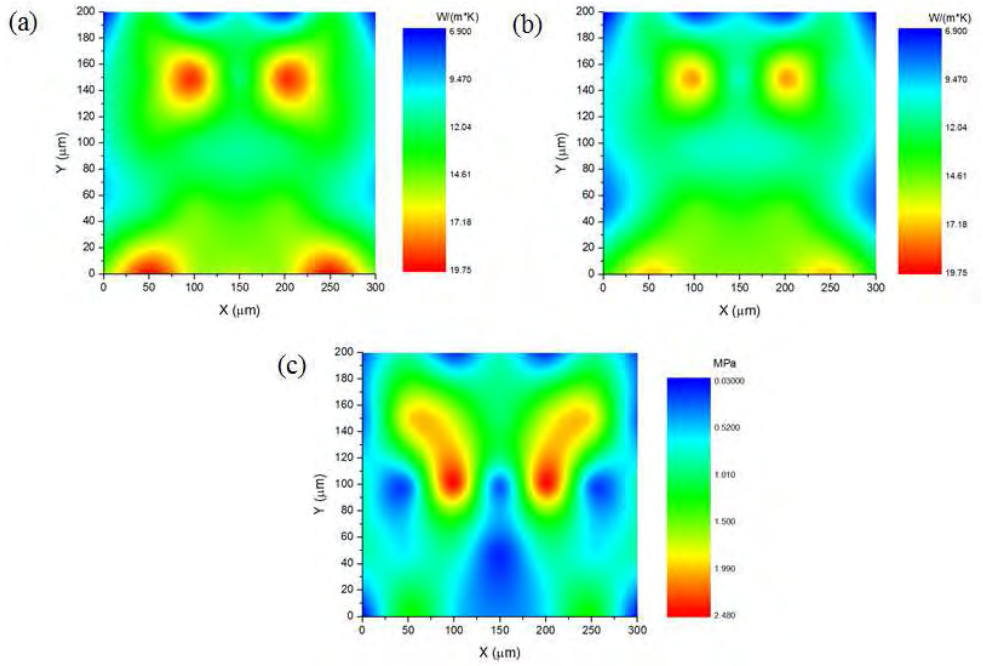

Figure S3.58. (a) Thermal conductivity distribution using Raman mapping at room without any loading, (b) Thermal conductivity distribution using Raman mapping at room during a loading of 2N, (c) Stress distribution using Raman mapping at room during a loading of 2N

Irradiated & 60 Days corroded sample

Fig. S3.59 (a) shows the thermal conductivity distribution without any loading. The effective thermal conductivity value over the whole domain is measured as 13.03 W/(m*K). Comparing to previous samples, irradiation doesn't induces a more obvious degradation on the effective thermal conductivity value. On the contrary, the thermal conductivity even rises slightly. Fig. S3.59 (b) shows the thermal conductivity distribution without a loading of 2N. Thermal conductivity degradation is also observed in this case. The effective thermal conductivity decrease to 11.943 W/(m*K). Fig. S3.59 (c) shows the stress conductivity distribution with a loading of 2N.

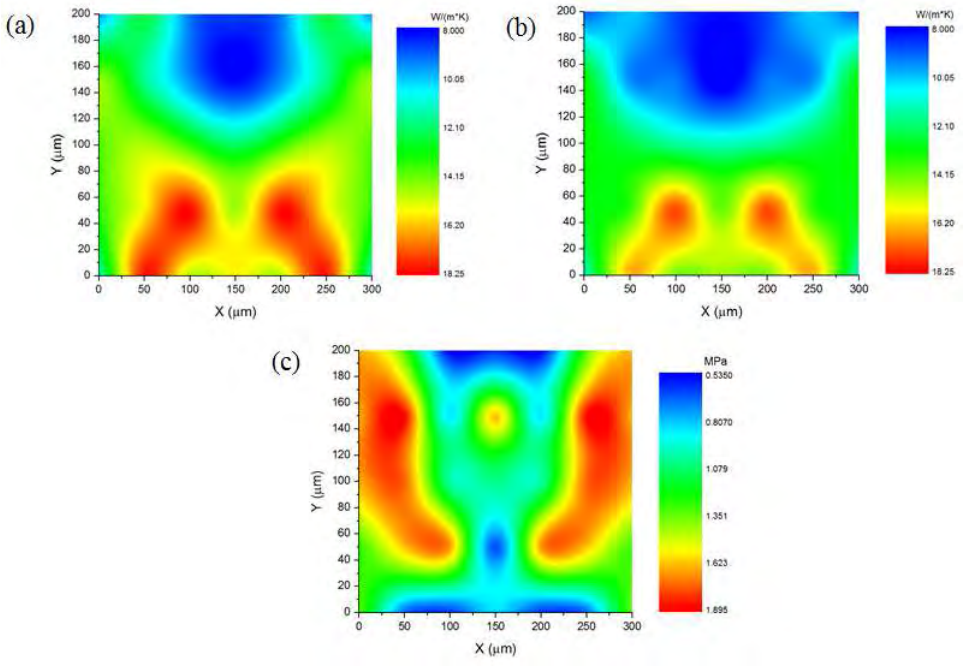

Figure S3.59. (a) Thermal conductivity distribution using Raman mapping at room without any loading, (b) Thermal conductivity distribution using Raman mapping at room during a loading of 2N, (c) Stress distribution using Raman mapping at room during a loading of 2N

Comparison

In order to get a better understanding of stress state influence on thermal conductivity change, a comparison summary is shown in following figure. Fig. S3.60 (a) shows the effective thermal conductivity value for each sample under different loading cases. Several important points can be noticed in this figure. Firstly, comparing with normal sample, both corrosion and irradiation doesn't cause an obvious degradation on thermal conductivity of zircaloy samples, this agrees with literature results on ASTM A533[20] and alloy 690[21]. However, when compressive loading is applied, thermal conductivity decreases in all three samples. Fig. S3.60 (b) shows thermal conductivity degradation at different stress states on each sample. The thermal conductivity degradation proportion shows a linear correlation with the stress state. Comparing the linear fitting results of different samples, the normal sample has a good resistance on stress induced thermal conductivity decrease. For the sample with only corrosion, stress induced thermal conductivity change begins to become apparent. When irradiation also comes into the case, the thermal conductivity gets very sensitive to the local stress state. The comparison clearly shows the stress induced thermal conductivity degradation in zircaloy samples. Although corrosion and irradiation don't change the effective thermal conductivity at loading free case, they obviously enhanced the stress state effects on thermal conductivity degradation under compressive loadings.

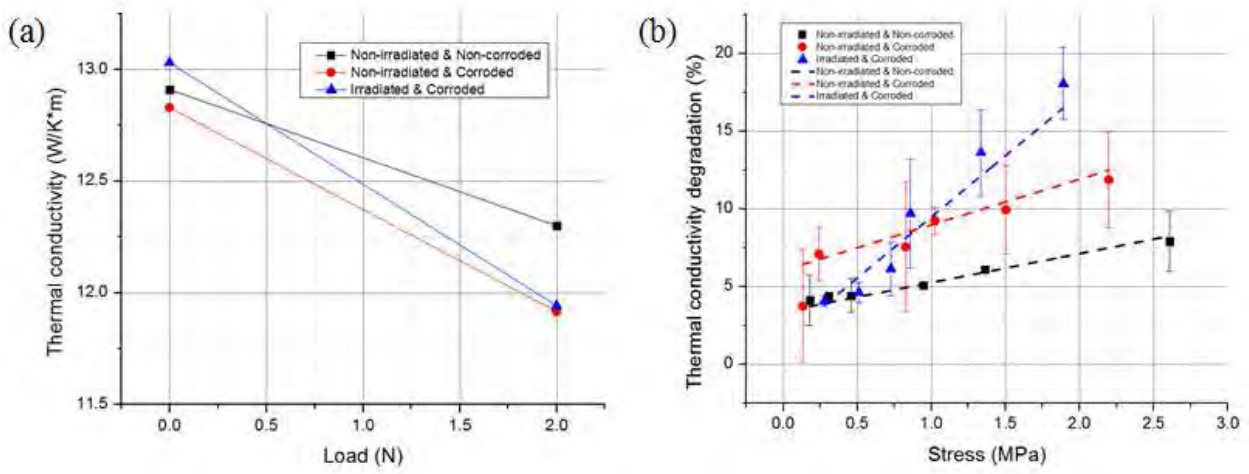

Figure S3.60. (a) effective thermal conductivity values for different samples, (b) Thermal conductivity degradation at different stress state.

THERMO-MECHANICAL CONSTITUTIVE LAW

The Johnson-Cook (JC) constitutive model is a most widely known temperature, strain and strain-rate-dependent phenomenological flow stress model, and is successfully used for a variety of materials with different ranges of deformation temperature and strain-rate. It assumed material is isotropic, avoiding the traditional concept of yield surface in constitutive equations. Therefore, JC model enjoyed much success because of its simplicity and the availability of parameters for carious materials. The original Johnson-Cook model can be expressed as:

$$\sigma = (A + B\varepsilon^{n})(1 + C ln\dot{\varepsilon}^{*})(1 - T^{*m})$$

Where σ is equivalent flow stress, ε is the equivalent plastic strain, A is the yield stress at reference temperature and reference strain-rate, B is the coefficient of strain-hardening, n is the strain-hardening exponent, C and m are the material constant which represent the coefficient of strain-rate hardening and thermal softening exponent, respectively. The expression in the first brackets gives the effects of strain on the flow stress, and the second represents instantaneous strain-rate sensitivity, while the third term represents the temperature dependence of flow stress. Obviously, the original JC model requires fewer material constants and few experiments to evaluate these constants. JC model assumes that thermal softening, strain-rate hardening and strain-hardening are three independent phenomena and can be isolated from each other, i.e., the original Johnson–Cook model does not represent any thermal or strain-rate history effects, but is simple to implement and the parameters are readily obtained from a limited number of experiments. In general, the JC model represents a set of models that consider that the mechanical behaviors of material are the multiplication effects of strain, strain-rate, and temperature. This form is simple and has a clear physical interpretation. However, the coupling effects of strain, temperature and strain-rate are omitted in the original JC model. The original JC model remains a good start point for our case. We can use our experiment results from nano-

indentation and nano-mechanical Raman to determine these parameters for zircaloy, stress-thermal conductivity relation will strongly affect the temperature distribution in the pellet and cladding system. And this influence will affect the constitutive relation through the last term of the JC model.

B. Michel[22] also introduced a nonlinear behavior of the cladding under irradiation is taken into account by a nonunified formulation coupling a creep law,

$$\frac{d\varepsilon_v}{dt} = A \cdot (J_2(\bar{\sigma}))^{n_p} \cdot e^{-\frac{Q_p}{RT}} \cdot e^{-Bt} + C \cdot (J_2(\bar{\sigma}))^{n_s} \cdot e^{-\frac{Q_s}{RT}} \cdot \Phi^p$$

Where $d\varepsilon_v/dt$ is the creep strain rate, Φ is the fast neutron flux, R is universal gas constant, A, n_p, Q_p, B, C, n_s, p are material parameters. The creep rate enhancement due to the effect of the fast neutron flux on the material is taken into account in the second term of above equation, which models stationary creep. The irradiation-induced hardening of the material is introduced in the first term above equation, which models the primary creep, and by the dependency of the material parameters on neutron fluence. The anisotropic behavior of the cladding, which is particularly important for some alloys, can also be taken into account by using Hill's equivalent stress instead of the Von Mises equivalent stress J2.

Measured thermal conductivity value under different loading cases are plotted for all samples. Figs. S3.61 (a)-(d) are plots for samples 1-4 respectively. Linear fitting process is used for all samples, and the fit relation can be expressed as

$$\kappa = 13.631 - 1.009\times10^{-7}\,|\sigma|$$

$$\kappa = 12.074 + 4.143\times10^{-7}\,|\sigma|$$

$$\kappa = 6.540 + 3.853\times10^{-7}\,|\sigma|$$

$$\kappa = 7.176 + 4.588\times10^{-7}\,|\sigma|$$

Same procedures with the stress-Raman relation measurement; the stress range during experiments are from 0N to 20N with an interval of 2N. Since the thickness of each sample is not exactly 1mm due to polishing process. Therefore, the stress state in each sample under same compressive loading is not exactly same as well; the stress range is from 0MPa to 10MPa. Based on above relations, a clear stress dependence of thermal conductivity in different samples can be established. Fig. S3.62 shows a direct comparison among different samples. Several interesting points could be found. Firstly, without any loading applied, thermal conductivity value of normal zircaloy sample is measured as $13.22\,Wm^{-1}K^{-1}$, which is close to literature reported values[21, 22]. Samples after either irradiation or corrosion, has a lower thermal conductivity value than the normal one, recorded as 11.92 and $7.40\,Wm^{-1}K^{-1}$. The thermal conductivity of sample after both irradiation and corrosion is recorded as $7.58\,Wm^{-1}K^{-1}$, which is close to the only irradiation case. From this comparison, it's clear that both corrosion and irradiation could reduce the thermal conductivity of zircaloy samples. However, irradiation is dominant in the thermal conductivity degradation. Secondly, more differences can be observed after the compressive loading is applied. For normal zircaloy sample, the thermal conductivity

decreases slightly with the increasing of compressive stress. However, after irradiation and corrosion, the trend has changed. The thermal conductivity increases as a function of the compressive stress in all other samples. These differences are clearly induced by irradiation and corrosion. The reasons for these changes are discussed in next part.

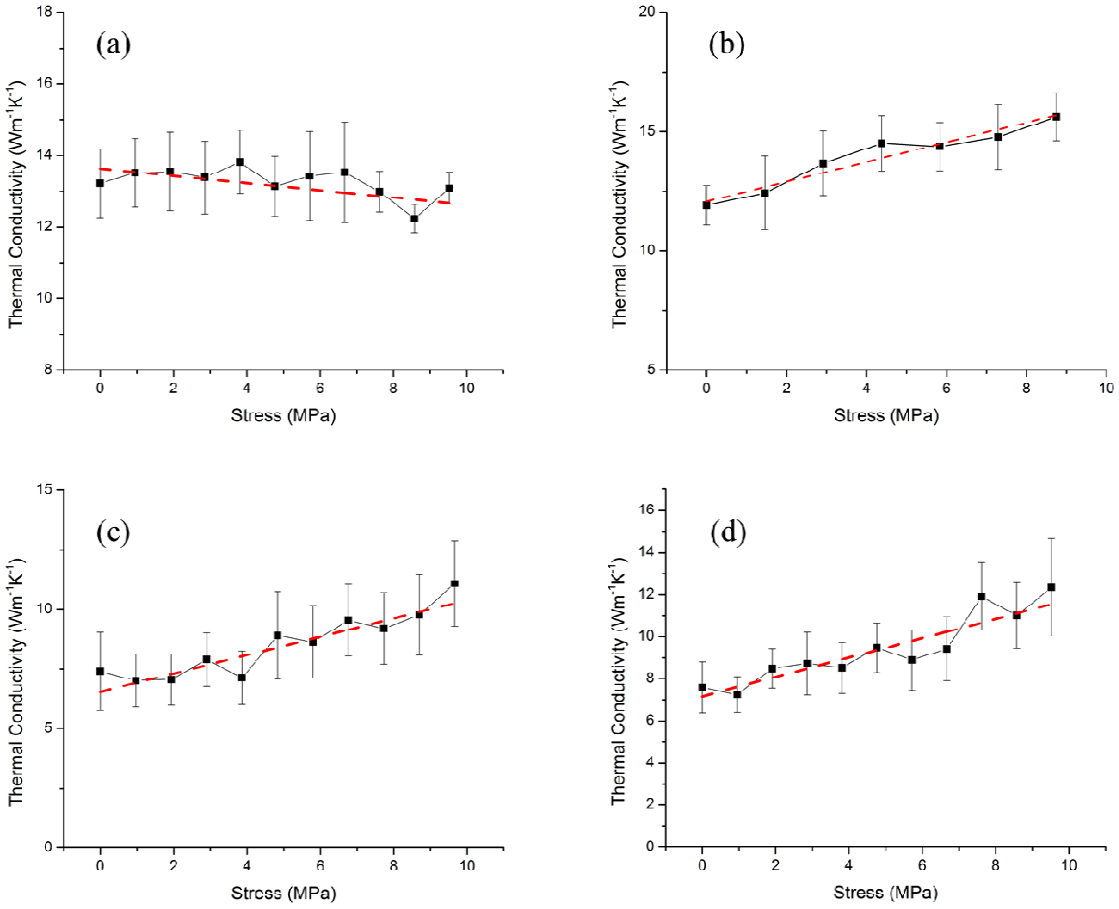

Figure S3.61. Thermal conductivity of zircaloy samples as a function of stress; (a) sample 1, (b) sample 2, (c) sample 3, (d) sample 4

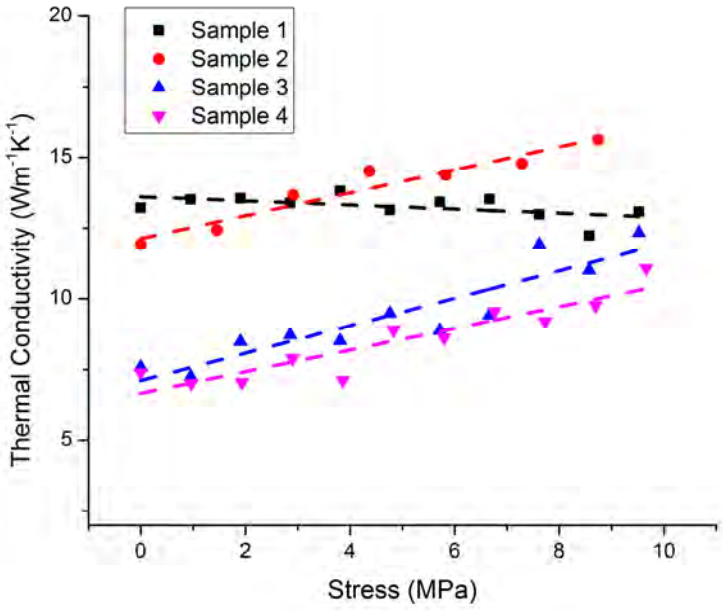

Figure S3.62. Comparison among different samples

3. PROJECT APPROACH UPDATES

3.1 ISSUES FACED IN TASK 3

The proposed m TEM methodology worked excellent with sputter deposited Zr thin films. However, the proposed material was Zircaloy. In the last quarter of first year, we started preparing FIB based preparation of TEM specimens. Our experience with that process raises two concerns,

Cost: the cost of FIB based specimen preparation is prohibitive for the budget ($6000 and $4000 only in the years 2 and 3 for the specimen preparation and in-situ TEM). Each specimen takes about 2 hours for preparation and about 5 hours for integration with the MEMS chip (total about $500, for preparation only. Another $500 for the experiment suggests only 4 to 5 experiments each year.

Quality: The Zircaloy material has significant residual stress which curls the specimen. Such curling is acceptable for conventional TEM characterization (i.e. imaging). But it is un-acceptable for integration with a MEMS device, which as essentially planar devices.

Proposed Alternatives: The PI will attempt to sputter deposit the Zircaloy specimen as an alternative. If this not possible, continuing with pure Zr could be a solution for the budget. We will also work on APMT steel and HT-9 steels as advised by TPOC.

3.2 ISSUES FACED IN TASK 4

The mechanical property-microstructure-temperature dependence data for polycrystalline Zr has now been established. The students are now trained on project methods. The next phase focuses on measuring environment dependent thermo-mechanical coupling in Zircaloy-4 samples as a function of Zircaloy microstructure. These targets are according to the schedule. The measurements will also be performed on HT-9/APMT steels and the models will be modified to include experimental

measurements, both in Tasks 3 and 4 for ultimate incorporation in MOOSE™ framework.

3.3 Issues Faced in Task 5

Zircaloy TEM specimen preparation was accomplished with FIB milling. However, their residual stress made the specimens curl up and the integration with MEMS test chips were not reliable. Therefore, we worked with zirconium thin film that was evaporated on the silicon wafer. We will address this issue by (a) developing a zircaloy sputtering scheme to achieve thin films for electron transparency and (b) continue the FIB milling scheme.

In the Oct 2015-Jan 2016 quarter, the TEM was unavailable at Penn State. Also neutron irradiated specimens were hot enough not to be released by the Isotope Committee. To complete this task, we performed ex-situ experiments on gamma irradiated specimens.

3.4 Issues Faced in Task 6

Original plan was for neutron irradiation. However, due to issues surrounding the time required for radioactivity to die for testing to be done in lab, ion-irradiation was finally chosen. A request was made for equipment upgrade from fund without additional expenditure. Request was approved. Neutron irradiation of equipment is also ongoing.

3.5 Issues Faced in Task 7

Phase field models to incorporate experimental results have been started. PI is working with INL on implementing these models in MOOSE. A significant part of project time is being spent on student training.

4. Key Personnel Updates

There has not been any change.

PI, Dr. Tomar, and co-PI, Dr. Aman Haque are US Citizens. The following personnel are working.

Personnel At Purdue University

Last Name: Wang First Name: Hao
Country of Citizenship: China
Major: Aeronautics and Astronautics
Expected Graduation Year: 2019
Level of Education Pursued: PhD

Last Name: Biswas First Name: Sudipta
Country of Citizenship: India
Major: Aeronautics and Astronautics
Expected Graduation Year: 2016
Level of Education Pursued: PhD

Last Name: Zhang First Name: Yang
Country of Citizenship: China
Major: Aeronautics and Astronautics

Expected Graduation Year: 2016
Level of Education Pursued: PhD

Last Name: Marsh First Name: Jonathan
Country of Citizenship: USA
Major: Aeronautics and Astronautics
Expected Graduation Year: 2017
Level of Education Pursued: PhD

Last Name: Acosta First Name: Eric
Country of Citizenship: USA
Major: Nuclear Engineering
Expected Graduation Year: 2015
Level of Education Pursued: BS

Last Name: El Atwani First Name: Osman
Country of Citizenship: Palestine/Turkey
Major: Nuclear Engineering
Level of Education Pursued: PhD
Role: Visiting Assistant Professor

Personnel At Penn State University

Last Name: Wang First Name: Baoming
Country of Citizenship: China
Major: Mechanical Engineering
Expected Graduation Year: 2017
Level of Education Pursued: PhD

Last Name: Crawmer First Name: Joel
Country of Citizenship: USA
Major: Mechanical Engineering
Expected Graduation Year: 2017
Level of Education Pursued: BS

Last Name: Zhang First Name: Qian
Country of Citizenship: China
Major: Materials Science & Engineering
Expected Graduation Year: 2016
Level of Education Pursued: PhD

Last Name: Pulavarthy First Name:Raghu
Country of Citizenship: India
Major: Mechanical Engineering

Expected Graduation Year: 2016
Level of Education Pursued: PhD

5. ISSUES OR CONCERNS

PIs wanted to update the equipment. The request is approved by DoE.

In the Jan-April 2016 quarter, the co-PI Haque faced equipment problems. Penn State University acquired to new TEMs and he had to change the specimen holder. This caused some compatibility issues which is currently being fixed. Another concern was the significant amorphity in the TEM specimens prepared from the bulk materials. Even though Xray diffractions supports the co-PI's findings, he is still investigating whether the specimen preparation itself damaging the crystallinity.

6. PRODUCTS PRODUCED AND TECHNOLOGY TRANSFER

LIST OF INTERNATIONAL JOURNAL PUBLICATIONS

1. Wang, B., Tomar, V., and Haque, A., 2015, *In-situ* TEM mechanical testing of nanocrystalline zirconium thin films, Materials Letters, Vol. 152, 1 pp. 105–108, 2015.
2. Marsh, M., Han, Y., Verma, D., and Tomar, V., 2015, An investigation into plastic deformation of irradiated tungsten microstructure at elevated temperatures using the Anand's viscoplastic model, International Journal of Plasticity, Volume 74, pages 127-140.
3. Marsh, J., Verma, D., Zhang, Y., Biswas, S., Haque, A., El-Atwani, O., and Tomar, V., 2015, Nanomechanical Characterization of Temperature Dependent Mechanical Properties of Ion Irradiated Zirconium with Consideration of Microstructure and Surface Damage, JoM-The Journal of the Metals, Minerals, and Materials Society, Volume 67, Issue 12, pp 2945–2958.
4. B. Wang and M. A. Haque "In-situ Microstructural Control and Mechanical Testing inside the Transmission Electron Microscope at Elevated Temperatures", JoM-The Journal of the Metals, Minerals, and Materials Society, Volume 67, Issue 8, pp 1713-1720, 2015.
5. B. Wang, R. A. Pulavarthy and M. A. Haque, Grain Size Induced Thermo-Mechanical Coupling in Zirconium Thin Films Journal of Thermal Analysis and Calorimetry, Vol 123, pp 1197, 2016.
6. Biswas, S., Schwen, D., Singh, J., and Tomar, V., 2016, A Study of the Evolution Of Microstructure And Consolidation Kinetics During Field Assisted Sintering Using A Phase Field Modeling Based Approach, Extreme Mechanics Letters, Volume 7, pp 78-89.
7. Verma, D., Biswas, S., Prakash, C., and Tomar, V., 2017, Relating Interface Evolution with Interface Mechanics based on Interface Properties, Journal of Materials (TMS), Volume 69, Issue 1, pp 30–38.
8. Biswas, S., Schwen, D., Wang, H., and Tomar, V., 2016, Role of irradiation fluence in microstructure dependent thermal conductivity, submitted.

Conference Papers

None

Presentations

1. In-Situ Multi-domain Characterization of Nanoscale Materials, Baoming Wang and Aman Haque, Society of Engineering Sciences, Oct. 2-5, 2016 at the University of

Maryland, College Park.

2. Mechanical & Thermal Properties of Gamma Irradiated Materials, Baoming Wang Raghu Pulavarthy & Aman Haque, Materials Research Society Spring 2016 Meeting, Control ID Number: ((2406618),
3. Biswas, S., Marsh, Y., and Tomar, V., 2014, "Role of length scale and temperature in indentation induced creep behavior of polycrystalline Al", 2014 Society of Engineering Science Meeting, October 1-3, 2014, Purdue University, West Lafayette-IN.

Workshops Attended

1. 2nd Int. Workshop Irradiation of Nuclear Materials: Flux and Dose Effects, November 4-6, 2015, CEA – INSTN Cadarache, France
2. Nuclear Energy Agency International Workshop on Structural Materials for Innovative Nuclear Systems, 11-14 July 2016, Manchester, UK, Hosted by University of Manchester
3. In-situ TEM Testing of Thermo-physical Properties, Idaho National Lab, NSUF meeting, June 2015.
4. Controlling Microstructure and Measuring Thermo-Electro-Mechanical Properties of Nanoscale Materials, Baoming Wang and Aman Haque, Penn State Research Day, October 5-6, University Park, PA 16802.

7. REFERENCES:

Ahmad, S., Bashir, S., Ali, N., Yousaf, D., Naeem, A., Ahmad, R. and Khlaeeq-ur-Rahman, M. (2014). "Effect of ion irradiation on the surface, structural and mechanical properties of brass." Nuclear Instruments and Methods in Physics Research Section B: Beam Interactions with Materials and Atoms **325**.

Ahmed, K., Pakarinen, J., Allen, T. and El-Azab, A. (2014). "Phase field simulation of grain growth in porous uranium dioxide." Journal of Nuclear Materials **446**(1-3): 90-99.

Alam, T., Wang, B., Pulavarthy, R., Haque, M. A., Muratore, C., Glavin, N., Roy, A. K. and Voevodin, A. A. (2014). "Domain engineering of physical vapor deposited two-dimensional materials." Applied Physics Letters **105**(21): 213110 (213111-213115).

Anand, L. (1982). "Constitutive equations for the rate-dependent deformation of metals at elevated temperatures." Journal of engineering materials and … **104**: 12-17.

Aranson, I. S., Kalatsky, V. A. and Vinokur, V. M. (2000). "Continuum field description of crack propagation." Physical Review Letters **85**(1): 118-121.

Asoka-Kumar, P., O'Brien, K., Lynn, K. G., Simpson, P. J. and Rodbell, K. P. (1996). "Detection of current-induced vacancies in thin aluminum–copper lines using positrons." Applied Physics Letters **68**(3): 406-408.

Behrisch, R., Bo, J., Eckstein, W., Littmark, U., Roth, J. and Scherzer, B. (1975). "Implantation profiles of low-energy helium in niobium and the blistering mechanism." Applied Physics Letters **27**(4): 199-201.

Brown, S., Kim, K. and Anand, L. (1989). "An internal variable constitutive model for hot working of metals." International Journal of Plasticity **5**: 95-130.

Cahn, J. W. and Hilliard, J. E. (1958). "Free Energy of a Nonuniform System. I. Interfacial Free Energy." The Journal of Chemical Physics **28**(2): 258-267.

Caspers, L., Fastenau, R., Van Veen, A. and Van Heugten, W. (1978). "Mutation of vacancies to divacancies by helium trapping in molybdenum effect on the onset of percolation." physica status solidi (a) **46**(2): 541-546.

Chen, X., Chen, G. and Sakane, M. (2005). "Prediction of stress-strain relationship with an improved Anand constitutive model for lead-free solder Sn-3." Components and Packaging ….

Crosby, T. and Ghoniem, N. (2012). "Phase-field modeling of thermomechanical damage in tungsten under severe plasma transients." Computational Mechanics **50**(2): 159-168.

Crosby, T. and Ghoniem, N. M. (2013). "Multiphysics model of thermomechanical and helium-induced damage of tungsten during plasma heat transients." Journal of Nuclear Materials **442**(1–3, Supplement 1): S261-S266.

De Orio, R., Ceric, H. and Selberherr, S. (2010). "Physically based models of electromigration: From Black's equation to modern TCAD models." Microelectronics Reliability **50**(6): 775-789.

Dean, J., Bradbury, A., Aldrich-Smith, G. and Clyne, T. W. (2013). "A procedure for extracting primary and secondary creep parameters from nanoindentation data." Mechanics of Materials **65**: 124-134.

El-Atwani, O., Efe, M., Heim, B. and Allain, J. P. (2013). "Surface damage in ultrafine and multimodal grained tungsten materials induced by low energy helium irradiation." Journal of Nuclear Materials **434**(1-3): 170-177.

El-Azab, A. and Liang‡, Y. (2003). "Nanoscale copper oxide ring structure on an SrTiO3 substrate." Philosophical Magazine **83**(31-34): 3847-3869.

Faulkner, D. and Woo, C. (1980). "Void swelling in zirconium." Journal of Nuclear Materials **90**(1): 307-316.

Gan, M. and Tomar, V. (2010). "Role of length scale and temperature in indentation induced creep behavior of polymer derived Si–C–O ceramics." Materials Science and Engineering: A **527**(29-30): 7615-7623.

Grafe, U., Bottger, B., Tiaden, J. and Fries, S. G. (2000). "Simulations of the initial transient during directional solidification of multicomponent alloys using the phase field method." Modelling and Simulation in Materials Science and Engineering **8**(6): 871-879.

Hoffman, R. and Turnbull, D. (1951). "Lattice and Grain Boundary Self-Diffusion in Silver." Journal of Applied Physics **22**(5): 634-639.

Hu, S. and Henager Jr, C. H. (2009a). "Phase-field modeling of void lattice formation under irradiation." Journal of Nuclear Materials **394**(2–3): 155-159.

Hu, S. and Henager Jr, C. H. (2009b). "Phase-field simulations of Te-precipitate morphology and evolution kinetics in Te-rich CdTe crystals." Journal of Crystal Growth **311**(11): 3184-3194.

Hu, S. Y. and Chen, L. Q. (2001). "Solute segregation and coherent nucleation and growth near a dislocation - A phase-field model integrating defect and phase microstructures." Acta Materialia **49**(3): 463-472.

Hunter, A., Saied, F., Le, C. and Koslowski, M. (2010). "Large-Scale 3D Phase Field Dislocation Dynamics Simulations On High-Performance Architectures." International Journal of High Performance Computing Applications **25**(2): 223-235.

JF Ziegler, M. D. Z., J.P. Biersack (2010). "SRIM – The stopping and range of ions in matter (2010)." Nuclear Instruments and Methods in Physics Research B **268**: 1818-1823.
Jin, Y. M., Artemev, A. and Khachaturyan, A. G. (2001). "Three-dimensional phase field model of low-symmetry martensitic transformation in polycrystal: Simulation of zeta '(2) martensite in AuCd alloys." Acta Materialia **49**(12): 2309-2320.
Karma, A., Kessler, D. A. and Levine, H. (2001). "Phase-field model of mode III dynamic fracture." Physical Review Letters **87**(4).
Kazaryan, A., Wang, Y., Dregia, S. A. and Patton, B. R. (2000). "Generalized phase-field model for computer simulation of grain growth in anisotropic systems." Physical Review B **61**(21): 14275-14278.
Kirchheim, R. (1992). "Stress and electromigration in Al-lines of integrated circuits." Acta Metallurgica et Materialia **40**(2): 309-323.
Kumar, S., Alam, M. T., Connell, Z. and Haque, M. A. (2011). "Electromigration stress induced deformation mechanisms in free-standing platinum thin films." Scripta Materialia **65**(4): 277-280.
Lin, M. and Basaran, C. (2005). "Electromigration induced stress analysis using fully coupled mechanical–diffusion equations with nonlinear material properties." Computational Materials Science **34**(1): 82-98.
Loginova, I., Amberg, G. and Agren, J. (2001). "Phase-field simulations of non-isothermal binary alloy solidification." Acta Materialia **49**(4): 573-581.
M. Kothari and Anand, L. (1998). "Elasto-viscoplastic constitutive equations for polycrystalline metals: Application to tantalum." Journal of Mechanics and Physics of Solids **46**(1).
Millett, P. C., El-Azab, A., Rokkam, S., Tonks, M. and Wolf, D. (2011a). "Phase-field simulation of irradiated metals: Part I: Void kinetics." Computational Materials Science **50**(3): 949-959.
Millett, P. C., El-Azab, A. and Wolf, D. (2011b). "Phase-field simulation of irradiated metals: Part II: Gas bubble kinetics." Computational Materials Science **50**(3): 960-970.
Minyou, Y. (2005). " Effects of low energy and high flux helium/hydrogen plasma irradiation on tungsten as plasma facing material." Plasma Sci. Technol **7**: 2828-2834.
Oliver, W. and Pharr, G. (1992). "An improved technique for determining hardness and elastic modulus using load and displacement sensing indentation experiments." Journal of materials research.
Pawel, R., Cathcart, J. and McKee, R. (1979). "The Kinetics of Oxidation of Zircaloy-4 in Steam at High Temperatures." Journal of the Electrochemical Society **126**(7): 1105-1111.
S. D. Harkness and Li, C.-Y. (1971). "A study of void formation in fast neutron-irradiated metals." Metallurgical Transactions **2**(5).
Singh, B. N. and Foreman, A. (1974). "Calculated grain size-dependent vacancy supersaturation and its effect on void formation." Philosophical Magazine **29**(4): 847-858.
Som, T., Bhargava, S., Malhotra, M., Bist, H., Kulkarni, V. and Kumar, S. (1998). "MeV He+ ion induced delamination of diamond films." Applied physics letters **72**(23): 3014-3016.
Tabachnikova, E. D., Podolskiy, A. V., Bengus, V. Z., Smirnov, S., Natsik, V., Azhazha, V., Tikhonovsky, M., Velikodny, A., Andrievskaya, N. and Storozhilov, G. (2008). Strength and Plasticity of Ultra-Fine Grained Zirconium at Low Temperatures. Materials Science

Forum, Trans Tech Publ.
Tan, C., Gan, Z., Li, W. and Hou, Y. (2011). Development of Physics-Based Modeling for ULSI Interconnections Failure Mechanisms: Electromigration and Stress-Induced Voiding. Applications of Finite Element Methods for Reliability Studies on ULSI Interconnections, Springer London**:** 5-38.
Wang, B., Alam, M. T. and Haque, M. A. (2014). "Grain growth in nanocrystalline nickel films at low temperature and stress." Scripta Materialia **71**(0): 1-4.
Wang, Y. and Khachaturyan, A. G. (1997). "Three-dimensional field model and computer modeling of martensitic transformations." Acta Materialia **45**(2): 759-773.
Wu, Z.-J. and Ho, P. S. (2012). "Size effect on the electron wind force for electromigration at the top metal-dielectric interface in nanoscale interconnects." Applied Physics Letters **101**(10): 101601.
Yulan Li, S. H., Robert Montgomery, Fei Gao, Xin Sun (2012). "Problem 1: Mesoscale Simulations of Intra-granular Fission Gas Bubbles in UO2 under Postirradiation Thermal Annealing ".
Zhang, L., Xue, S., Gao, L., Zeng, G., Sheng, Z., Chen, Y. and Yu, S. (2009). "Determination of Anand parameters for SnAgCuCe solder." Modelling and Simulation in Materials Science and Engineering **17**(7): 075014.